SUBTERRANEAN BATTERY ENERGY STORAGE SYSTEMS FOR GRID STORAGE: THERMAL MODELING AND EXPERIMENTAL VALIDATION

by

Elizabeth Oyekola

Submitted in partial fulfilment of the requirements

for the degree of Master of Applied Science

at

Dalhousie University

Halifax, Nova Scotia

January 2024

© Copyright by Elizabeth Oyekola, 2024

Table of Contents

List of Tables

List of Figures

Abstract

The deployment of stationary battery energy storage system continues to grow as renewable energy systems are integrated into the electricity grid. Research on battery systems covering areas of system optimization, battery management system, grid integration of BESS, etc., have transformed the pattern of energy use and storage resulting in more energy efficient and sustainable energy systems.

This thesis explores the thermal dynamics of subterranean battery energy storage systems for residential applications. Residential battery installations have brought up concerns surrounding safety, pollution, and structural footprint, which could hinder a widespread adoption of stationary battery storage systems for increased electrification. Burying batteries underground addresses these concerns. While previous research has focused above-ground battery installations, this study explores the potential of utilizing the ground as an infinite heat sink or storage for thermal management. The impact of soil temperatures, battery geometry and soil thermal properties on battery performance are analyzed through thermal modelling and laboratory experiments.

The result indicates that the thermal response of the battery and its surrounding soil is significantly influenced by the battery operation signal and the thermal properties. This is reflected in the variation peak battery temperature and the heating or cooling rate of the battery. The ground temperature has a linear influence on the peak battery temperatures but has no impact on the rate of heat dissipation. Variation of the geometry may create or reduce the heat pathways, which influences the temperature of the system minimally. For example, a four-sided battery pack creates a wider area for heat diffusion, and the predicted battery temperature peaks at 67 ^{o}C for an aggressive signal, which is a 5 ^{o}C less than the result of a six-sided battery pack.

List of Abbreviations and Symbols Used

Abbreviations

BESS	Battery Energy Storage Systems
BMS	Battery Management Systems
BTM	Battery Thermal Management
CC	Constant Current
CCCV	Constant Current Constant Voltage
CV	Constant Voltage
CSF	Conduction Shape Factor
IR	Internal Resistance
MV	Model Value
MWC	Mass Water Content
OCV	Open Circuit Voltage
PCM	Phase Change Material
RMSE	Root Mean Square Error
RPT	Reference Performance Test
SEI	Solid Electrolyte Interface
TEM	Thermistor Expansion Module
TV	Test Value
VPC	Voltage Per Cell
VWC	Volumetric Water Content

Symbols

		Unit
A	Area	m^2
C_p	Specific Heat Capacity	$Jg^{-1}K^{-1}$
C_v	Volumetric Heat Capacity	$Jg^{-1}K^{-1}$
I	Current	A
i	Individual components	-
L	Length	m

M	Mass	kg
M_c	Mass of Container	kg
M_s	Mass of Soil	kg
$M_{s,dry}$	Mass of Dry Soil	kg
$M_{s,wet}$	Mass of Wet Soil	kg
M_w	Mass of Water	kg
Q	Heat Rate	W
$\dot{Q}$	Heat Transfer per Unit Length	Wm^{-1}
$\ddot{Q}$	Heat flux (i.e., heat transfer per unit area)	Wm^{-2}
$\dddot{Q}$	Volumetric or Internal Heat Generation	Wm^{-3}
R	Resistance	Ω
r	Radius	m
S	Shape Factor	-
T	Temperature	^oC
t	Time	s
U	Heat transfer coefficient	$WK^{-1}m^{-2}$
V_{ocv}	Open-Circuit Voltage	V
V	Terminal Voltage	V
V_b	Volume of Battery Module	m^3
V_c	Volume of Container	m^3
Vs	Volume of Solid	m^3
V_w	Volume of Water	m^3
ρ	Density	gcm^{-3} or kgm^{-3}
$\boldsymbol{\rho_b}$	Bulk Soil Density	kgm^{-3}
$\boldsymbol{\rho_w}$	Density of Water	kgm^{-3}

Greek Letters

		Unit
λ	Thermal Conductivity	$Wm^{-1}K^{-1}$
ϕ	Volume fraction	

Acknowledgements

My profound gratitude and appreciation go to all who were instrumental in the completion of this thesis. The conclusion of this work would not be possible without the contributions of some incredible people who must be acknowledged.

Dr. Lukas Swan – your mentorship and guidance is one that I would not forget ever. You held no opportunity back from me (learning, funding, and others) and because of that, I had a splendid time learning and doing research under your supervision. You really are an incredible teacher, and human being. I hope I am able to make you proud, carrying all that I have learnt from you in my journey going forward. Thank you!

RESL group members – the most brilliant researchers, amazing personalities, and never boring team members one could ask to work with. Thank you for answering my ton of questions and helping my research. Thank you also for creating the wonderful space to be inquisitive, to learn, to explore, and to laugh. Thank you, Hayley, Bryan, Ryan, Mitch, Chris, Nat, and David. Every one of you is amazing.

The Novonix Group and Emera – this project could not be completed without the contributions of the members engineering team at Novonix and Emera. The resources for this project including the battery, soil, test unit materials and data, were provided by the people here. My gratitude extends to all involved

I would like to especially thank Avery Opalka for the software design and assistance building the test unit. Also, to Jason Zrum and Bryan Ellis, who assisted in the preliminary soil testing and test unit build for laboratory battery testing – Thank You.

I would like to acknowledge my supervisory committee, Prof. Jeff Dahn and Dr. Barret Kurylyk, for their assistance and guidance, which has been valuable to the conclusion of this work. Thank you.

I would like to acknowledge the financial support provided by Dr. Lukas Swan, NSGS-M, the Department of Mechanical Engineering and Dalhousie University, which contributed to my studies.

And to my family and friends, your support has kept me going. Thank you all

Chapter 1: Introduction

This thesis investigates subterranean battery installations and the thermal response to the battery operations, which influences the performance. This research includes thermal modeling and laboratory experimentation, from which results are analyzed and conclusions are drawn for comprehension of subterranean battery operations.

1.1 Background

The demand for electricity coupled with environmental concerns has propelled the growth of renewable energy generation. The integration of renewable energy resources (such as solar, wind, tidal, and geothermal energy, etc.) into electricity systems provides many benefits aimed to increased energy independence and security. However, the deployment of renewable energy systems in large scales into the electrical grid also introduces a myriad of problems due to the inconsistent nature of renewable energy sources. Energy storage provides solutions to these problems, due to its unique ability to act as a load (storing energy) and a generator (dispensing energy) [1].

Battery energy storage systems (BESS) are a widely used and cost-competitive energy storage technology. They possess a wide range of power and energy storage capabilities, are efficient, and are not subject to geographical constraints, which means they can be integrated at any point from energy production to end-use consumption [2]. Lithium-ion is the foremost battery technology in the market due to its unique characteristics including comparatively high energy and power density, improved cycling stability (i.e., reversible intercalation and deintercalation of lithium ions in the electrode materials), and high cycle life. Thus, increased efforts at electrification through battery energy storage employ lithium-ion battery technology and have given rise to a wide range of these units on the market for diverse applications including stationary applications. This presents the question of the physical placement of BESS in the energy system. BESS placement involves the process of BESS sizing and choosing an installation location in the energy system [3], [4]. BESS placement discussed in existing literature is targeted at minimizing cost and energy or power losses showing a major consideration towards technical operation and maintenance [3], [5], [6], [7]. BESS placement models and algorithms developed in literature place minimal focus on the installation process, and often do not consider the state of the physical location (building or

space) in determining an optimal location for BESS placement. The physical footprint of BESS varies depending on the technology employed and the energy capacity required. Increased energy capacity necessitates additional space. It is not unusual for owners of distributed BESS to utilize indoor spaces such as the garage or basement approved by [8], which typically have poor air circulation for maintaining the ambient temperatures within a range that is favorable BESS operations. In some cases, an external structure may need to be built to house BESS units. However, there are concerns from BESS owners regarding safety, the inconvenience of additional cost, thermal management, strict adherence to stringent codes and standards like the standard for the installation of stationary energy storage systems, NFPA 855, Canadian electrical code, CSA C22.1:21 [9], etc. As an innovative alternative, installation of batteries underground could potentially address these concerns. Such subterranean BESS installations leave no apparent footprint as they require no external structure to be constructed. They are not noticeable, hence concerns from the BESS owner regarding safety, thermal management, codes and standards, etc., are alleviated. BESS adoption for residential applications is likely to increase when there are less worries about indoor installations.

1.2 Research Objectives

The primary challenge with subterranean BESS operation is thermal management due to difficulty accessing the system underground. BESS require thermal management to keep battery temperatures uniform and within a desired temperature range. Extensive research had been done on battery thermal management, often involving large convective surfaces or active air or liquid thermal control systems, which is easily implemented for above-ground BESS installations. Subterranean environments experience limited temperature fluctuation further away from surface levels, which eliminates the undesirable effects of ambient temperature fluctuations. However, accessibility to the battery is limited underground, hence active thermal management utilizing active control mechanism for thermal management, is difficult to achieve. Consequently, passive thermal management which requires only the ambient environment, and no active thermal control mechanism is more plausible. Thermal management of the battery below ground surface is complicated by varying properties in the ground e.g. thermal conductivity, moisture content in the soil, thermal mass. The objective of this research is to model the thermal dynamics of subterranean battery operation and perform practical lab tests to evaluate the cycling and power capabilities as

a function of the maximum temperatures, as well as other limitations under continuous operations. This research provides a framework for modeling and evaluating subterranean battery operation in different scenarios and for various power outputs. Thus, the research questions for this project are,

- What is the temperature response of the battery and the surrounding soil during operation, and how does this vary for different soil?
- What is the heat dissipation rate, and how does that decide the duration of maximum power output and maximum average power from the battery during continuous operations?
- What is the average steady state temperature and the impact on the degradation of lithium-ion battery?
- What are the cycling and power limitations as a function of temperature?
- How do the limitations affect battery operations and residential battery applications?

1.3 Scope of the Research

The model developed in this work is a thermal model for a module or pack-level battery operation. The modeling technique is analytical with the use of ANSYS and Solidworks software packages. ANSYS is an analytical modeling and simulation tool, which uses finite element analysis for comprehensive engineering simulation and provides detailed and accurate analysis results. Solidworks is a design software used for computer-aided design, and simple engineering model simulations and analysis. For this work, the geometry parts are designed using Solidworks and imported into ANSYS for thermal simulation and analysis. The soil thermal properties are assumed to be homogenous. Emphasis is placed on the heat dissipation in the soil, and the thermal recovery of the battery. A comprehensive study of the battery module itself (at the cell level interfaces) in operation underground is a different scope outside of this study. Therefore, for an integrated battery module with a cooling plate, it is tenable that the battery is modeled as a single lumped element with uniform heat generation. A test unit was built for experimental validation of the model.

This research is targeted towards residential applications given the growth of distributed renewable energy generation and BESS installations.

Chapter 2: Literature Review

This chapter provides a review of academic literature relevant to this research. The selected literature focus on battery thermal behaviours, management and control, and the thermal dynamics of subterranean environments. The findings drawn from the reviewed literature provide critical information to the basis of this project, and present benchmarks for comparison of the model.

2.1 Thermal Behaviour of Lithium-ion Battery

The thermal dynamics in a battery is a complex process that involves several events in the battery such as entropy change, mass transport, charge transport, etc. Many researchers have studied this process for understanding and designing thermal management strategies for battery operations (involving small cells or modules and large battery stacks).

2.1.1 Heat Generation in Lithium-ion Batteries

The heat generated in lithium-ion batteries can be attributed to various phenomena occurring within the battery, which can be categorized into reversible and irreversible heat. These includes joule or ohmic heating, heating due to charge transfer between the electrodes and the electrolyte, heating due to mass transport resistance between the electrodes, through the electrolyte, heat of mixing, phase change heat, side reactions heat and entropic heating caused by the insertion and removal of lithium ions from the electrode materials [10], [11], [12], [13], [14].

Irreversible heat generation

The irreversible heat generation arise due to transport resistances and overpotentials related to charge transfer reactions in the battery. Transport resistances includes electron transport resistance in the electrode materials and the current collectors, contact resistance between material components, charge transport resistance between the electrode and electrolyte interfaces, and mass transport resistance in the electrolyte. These resistances contribute to power lost as heat into the battery module and its external environment. Other contributions to irreversible heat generation includes heat occurring as a result of undesired electrolyte-electrode reactions, solid electrolyte interface (SEI) reactions with the electrolyte, and heat of mixing during battery voltage relaxation [14], [15].

Reversible heat generation

The reversible heat generation is attributed to entropic heating due to the electrochemical processes that occur within the battery. The intercalation and deintercalation of lithium ions in the electrode materials leads to changes in the atomic arrangement in the crystal lattices in the electrodes causing a change in entropy. An increase in the entropy absorbs heat and a decrease in entropy releases heat. Ideally, the same amount of heat is absorbed as is released during battery operation, making entropic heating reversible [12], [14], [16]

For most battery thermal models, the heat generated due to side reactions, mixing and phase changes are neglected because they are often considered small compared to heat generated due to resistance in the battery.

Several factors affect reversible and irreversible heating which includes; ambient temperatures, state of charge or depth of discharge, charge and discharge rates and electrode material structure [11]. Chen et al. in [17] summarizes that a battery's thermal behaviour and its electrochemical performance are dependent on each other. During a discharge, a battery generates more heat with increasing rate of discharge and depth of discharge. Consequently, increasing temperatures enhances a battery's performance due to increased conductivity of ions in the electrolyte and other factors.

During battery operations, the irreversible heat (joule heating) is the predominant source of heat as a function of the state of charge and current rate [16]. The heat which cannot be converted back to electrical energy causes an initial localized increase in battery temperature, which is dependent on the battery thermal mass, and is then dissipated to the external environment of the battery. The heat generated may be dissipated more easily for smaller batteries than larger battery stacks due to shorter path lengths. For battery modules or packs, the heat generated is higher than that of a single cell, from a scaling perspective, and elevated battery temperatures are more likely due to a lower surface area to volume ratio for heat dissipation, than that of a single cell.

2.2 Temperature Effect on Batteries

The performance and degradation of batteries are strongly influenced by temperatures, which comprises of both operational and ambient temperatures. The operational temperature is defined as the temperature of a battery, usually measured at the battery cell surface, during battery

operation. The ambient temperature is defined as the temperature of the battery's external environment, which includes the storage temperature. The effect of temperature presents itself in the battery electrochemical performance and its aging [18]. The temperature effects on lithium-ion batteries can be discussed in three groups: low temperature influence, high temperature influence and the influence of non-uniform temperature distribution.

2.2.1 Low Temperature Influence

A sundry of studies has been done on the effects of low temperatures, typically below -20 ºC, on lithium-ion batteries, which has established that lithium-ion batteries perform inadequately in low temperatures [19]. The poor performance can be primarily attributed to the transport properties of the electrolyte, which is the medium for ion transport between the battery electrodes. At low temperatures, the deliverable energy and power from lithium-ion batteries decrease [12], which is due to poor electrolyte conductivity, low charge transfer capabilities, increased resistance due to SEI formation, and reduced ion diffusivity through the active materials on the electrodes [20], [21]. The viscosity of the electrolyte increases with reduced temperatures, which in turn increases the resistance of ion movement, limiting the ion conductivity [22]. To remedy this, various research has been done on electrolyte performance in cold temperatures. Similarly, experimental research has also shown that the charge transfer resistance and SEI resistance increases in lower temperatures, which reduces ion diffusivity into the active materials and limits the cycling performance of the battery [19], [21], [23].

The increase of the battery internal resistance limits the power capability of the cell, and the transport limitations of the electrolyte, in conjunction with SEI thickening at the electrodes limits the energy capacity. Loss of active material and lithium ions from lithium plating occurs as a function of low ion diffusivity in the active material, which is a major aging mechanism for lithium-ion batteries [24], [25]. High current rate charge operations under low temperature conditions may lead to cracks in the negative active material due to mechanical stress, which contributes to battery degradation, and may lead to battery failure [26].

In summary, low temperatures not only limit battery performance but can also play a significant role in causing battery failure and degradation.

2.2.2 High Temperature Influence

In contrast to low temperature effects, higher temperatures reduce the electrolyte viscosity thus increasing the ionic conductivity. Ion diffusivity is also improved, which aids the movement of ions from one electrode to another and improves the electrochemical performance of the battery [11], [22]. This is beneficial for the overall energy efficiency, and power performance.

However, increased temperatures, typically above 60 ^{o}C triggers detrimental effects within the battery leading to undesired outcomes. High temperatures increase the rate of electrochemical reactions, which may lead to undesired side reactions. Ramadass et al. in [27] reported that accelerated chemical reactions due to high temperatures leading to thickening of SEI film on the electrode materials lead to more consumption of lithium ions, and increased resistance on the negative electrode resulting in capacity degradation with continuous cycling. Capacity degradation may also be attributed to electrolyte decomposition and degradation of active material, which is expedited at higher temperatures [28]. Increased resistance is a byproduct of SEI formation and thickening, electrolyte decomposition as well as active material degradation, all contributing to reduced power capabilities of the battery [29].

During battery operation, the temperature of a battery increases due to joule heating and the electrochemical reactions generating heat. However, as the battery degrades, the temperature rise during operations become more inflated, and depending on the application rate, this could lead to thermal runaway and cause battery failure. Thermal runaway occurs when the exothermic reaction between the electrolyte and the electrodes is expedited by higher temperatures, increasing the heat generation rate, and leading to gas production. If the heat generated is not dissipated fast enough, the battery temperature surges further which leads to an exacerbation of the exothermic reactions, developing into a self-sustaining loop. The outcome of this snow-ball effect is a thermal runaway occurrence. The accumulation of gas within the battery, heightens the risk of rupture and an explosion evolving into a safety incident [30].

Although higher temperatures improve the battery's electrochemical performance, they have undesirable consequence that expedite battery degradation and reduce battery life.

2.2.3 Non-uniform Temperature Distribution

As mentioned earlier, temperature directly influences the reaction rate within a battery. Therefore, the temperature distribution of a battery is crucial for uniform battery performance. Non-uniform temperatures lead to uneven reaction rates within the battery resulting in non-uniformity of other parameters such as resistance, capacity, etc., and different degradation rates [31], [32]. Experimental results from the study done by Feng et al. [33] proved a temperature difference of 5 ^{o}C within a battery module or pack, resulting in a 1.5% to 2% loss of the battery's useful capacity. Similarly, Kuper et al. [34] reported that a temperature difference of 5 ^{o}C within a battery module or pack, reduces the useful power capability of the battery by 10%. Thus, it is recommended to keep battery temperatures as uniform as possible, and not exceed a temperature difference of 5 ^{o}C.

The typical recommended temperature range provided by battery manufacturers in technical data sheets for long lasting lithium-ion batteries are 0 – 45 ^{o}C for charging and -20 – 60 ^{o}C for discharge operations.

2.3 Battery Thermal Management

It has been established that lithium-ion batteries have an optimal temperature range of operations, outside of which, the battery performance and life is adversely affected. To predict the battery's thermal behaviour, diverse thermal models have been developed and validated by experiments to the end of optimizing battery design and operation performance. Accordingly, battery thermal management has become a topic of investigation adopting the thermal model results and developing techniques for thermal control. The primary purpose of battery thermal management is to keep the battery temperatures within an acceptable range and maintain uniform temperatures within the battery. This may involve cooling or heating depending on the environment of BESS integration. Additional purposes for battery thermal management, highlighted in [35] are insulation and thermal storage. Battery thermal management may be categorized in diverse ways based on the material used (i.e., liquid, air, phase change materials), heating or cooling, internal or external, active, or passive etc., with each having distinct advantages and disadvantages [36]. For simplicity, they will be classified into active or passive thermal management as defined below in this review.

2.3.1 Active Battery Thermal Management

Active thermal management, in existing literature have been defined as requiring the use of external device that consume energy for thermal control [37]. However, for this study, this definition is broadened to include the involvement of active control mechanisms to determine thermal behaviour. Active thermal management systems may employ the use of liquid, or air.

Air-based active BTM

Battery heating or cooling can be done through forced convection by directing the air using a fan or pump. This strategy may be adopted for small battery modules due to its simplicity, and low cost. Typical values for the convective heat transfer of air under free or forced convection, ranges from 2.5 to 500 $Wm^{-2}k^{-1}$, and that of liquids ranges from 100 to 100,000 $Wm^{-2}k^{-1}$ [38]. The heat transfer coefficient of air is low compared to liquids, hence air-based systems may be limited in controlling battery temperatures [35], [37]. Many studies have been done on air-based thermal management for batteries, with existing literature focusing on the design aspect and cell arrangement, efficiency of thermal management, and control mechanisms.

Yu et al. in their investigation of air based battery thermal management systems [39], report that thermal management is enhanced if the flow of air in the battery is in two dimensions (through the sides as well as the height of the battery). This helps to distribute the air more efficiently and maintain a more uniform temperature within the battery. They also note that thermal control is enhanced with a higher air flow rate resulting in more effective cooling and keeping the maximum battery temperature at 36 ^{o}C, as opposed to 42 ^{o}C, where there is no thermal management. A multiple factor analysis of angle of air inlet and outlet, and the air channel layout in the battery was studied by Xie et al. [40]. The study was done on a module containing ten prismatic lithium-ion cells and having eleven coolant passage within. The numerical study evaluated the variation of individual parameters of the air inlet and outlet angle, and the width of the coolant passage for battery design optimization. The result showed optimal thermal performance for cell arranged with uniform air channel widths between the cells and a 2.5^{o} angle of air injection and rejection in the battery pack resulting in a 28% drop in the temperature difference within the battery pack, and the peak temperature reduced by 12.8% from a maximum temperature of 44 ^{o}C observed for a range of different channel widths and angle of air injection and rejection. Their work highlighted the influence of battery design on thermal management.

Existing literature on BTM prioritize battery cooling rather than heating which is important for BESS operation in very cold climates. The air flow channel design is the most common aspect of optimization for air-based systems. The different channel designs are summarized and illustrated in Figure 1. However, this mode of BTM could be used in conjunction with substructures like fins, heat pipes or other thermally conductive materials for a more efficient thermal control [41]. For the many studies and models developed for optimizing air-BTM systems, they are often insufficient for large BESS operations involving high power-rate and high ambient temperature conditions, thus, liquid-based BTM is explored in research [37].

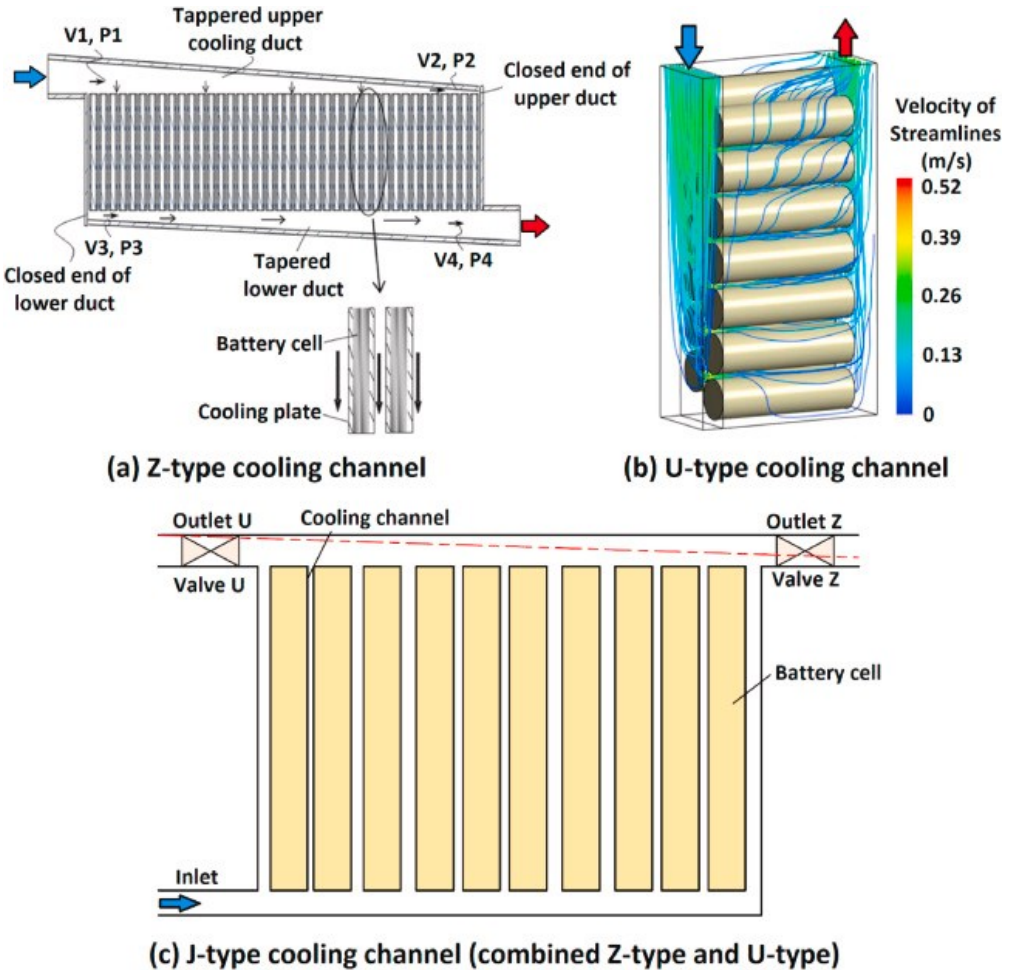

Figure 1: Different air-cooling channel designs [41]

Liquid-based active BTM

The use of liquids for BTM is adopted for better battery thermal management in comparison with air based BTM systems. Liquids possess better thermal qualities in terms of thermal conductivity and heat capacity, than air. However, the use of liquids makes the system susceptible to faults due to leakages, consequently making the system more complex. This means higher cost of the system, and increased maintenance. There are a range of thermal fluids (liquids) that can be used for thermal management including water, oil, acetone, glycol, etc., the choice of which is dependent on factors including thermal performance, safety, and cost [37]. Liquid BTM may be designed using direct or indirect contact with the battery [32].

Several studies have been done on this method of BTM, which includes one that was done by Karimi et al. [42] using a lumped capacitance thermal model and a flow network approach to analyze the thermal performance of water and silicone oil and compare the performance with air. In this study, the flow configurations are investigated and the effects on temperature distribution for pouch cells. The flow channels are looped around each battery cell, and the inlet and outlet locations are varied for comparison. The findings in this paper show that although, the U-configuration (i.e., inlet and outlet locations on one side of the battery) and Z-configuration (i.e., inlet and outlet locations on opposing sides and heights of the battery) are more common designs for liquid BTM, a three-point inlet, and single outlet position provides the best thermal results ensuring more even temperature distribution within the pack and maintain the battery temperatures below 40 ºC. The results also showed that for higher discharge-rates (12 minutes discharge or less), air cooling was insufficient to keep battery temperatures below 40 ºC, unlike the silicone oil and water. The use of silicone oil consumed higher parasitic power, compared to water, making water the best fluid for thermal management in this study.

Another numerical study validated by experiments compares the thermal performance of liquid metal (gallium and its alloys) to water for liquid based BTM with prismatic cells was done in [43]. The battery was discharged at a twenty-minute rate, and under ambient temperatures of 25 ºC. The use of this material was sufficient to keep the peak temperature at 40 ºC, and the temperature difference within the battery to 2.3 ºC as opposed to a temperature difference of 3.1 ºC with water as the thermal fluid. The findings from this study show that under the same flow conditions (i.e., configuration and flow rate), liquid metal provides superior thermal management than water,

keeping battery temperatures 2.3 ^{o}C cooler, and consumes less parasitic power, making them suitable for aggressive conditions (i.e., high ambient conditions, and high discharge rates). The demerit of liquid metal as a thermal fluid is the weight, which makes the system heavier and may not be preferred for applications where mass is a concern. In addition, aluminum jackets are often used for conventional liquid BTM systems, however, liquid metal reacts with aluminum hence nickel-plated copper is adopted for the jackets.

Liquid-based BTM may be direct or indirect. For direct cooling for BTM, the coolant flows through the battery module or pack and is in direct contact with individual cells surfaces. This mode of liquid cooling is rather complex, considering flow distribution and potential for leakage. Dielectric fluid is often utilized for direct cooling. For indirect liquid based BTM, heat plates or tubes are placed between the cells and at the surface areas of the cells in the battery module or pack, which passes liquid through to optimize the area for heat transfer and improve thermal performance [44], [45], [46].

The existing literature on liquid BTM systems focus on channel design and arrangement, coolant types and thermal properties, performance evaluation, and flow properties.

2.3.2 Passive Battery Thermal Management

Passive thermal management involves only the ambient environment and requires no external power consumption for thermal management [37]. Passive thermal management is a rather simple approach to BTM in that the complexities of active BTM are excluded, mostly depending on heat transfer through natural convection, conduction, or radiation. Passive thermal management involves no active control of the thermal behaviour of the battery. The thermal performance is determined by the natural flow of air, fins, heat plates or pipes or phase change materials (PCM), and the thermal properties of the components within the battery.

Wu et al. [47], studied the use of hydrogel for large-format lithium-ion pouch cells. Here hydrogel is used as a heat sink material, due to its ability to hold substantial amounts of water. The emphasis of this study is cooling and temperature uniformity. Different configurations were adopted for applying the hydrogel exploring direct contact cooling and indirect contact cooling, the system being integrated with a heat plate, fins, and copper foams. The indirect contact method which utilized hydrogel in conjunction with other thermally conductive material produced better thermal performance, proving to have more efficient thermal management. The most optimal configuration

was determined to be the heat fin-hydrogel method, characterized by the incorporation of heat fins emanating from a heat plate. This produced the most favourable result, with peak temperatures remaining below 33 ºC and a temperature difference of 1.4 ºC at a discharge rate of twenty minutes.

The use of passive thermal management for high-current cycling and high ambient temperatures was explored in [48] using PCM. The PCM used possessed a melting point of 42–45 ºC and exhibited sufficient heat absorption capabilities, keeping the peak battery temperature below 45 ºC and the temperature difference within 4 ºC at a discharge rate of twenty-nine minutes. Whereas in the absence of PCM, a larger temperature difference of approximately 10 ºC within the battery was observed. The long-term effect of PCM-BTM was evaluated for one-hour constant current discharge on the battery. The temperature control by the PCM resulted in lower operating temperatures which slowed the capacity degradation by approximately 50%. Compared to other systems, PCM-BTM provides compactness and reduces the weight of the overall system. However, pure PCM may possess low thermal conductivity and are more expensive than inorganic PCM [49]. Some battery designs may integrate the battery cells directly in contact with PCM, which may lead to displacement in the pack when the PCM melts, resulting in safety issues [50]. Researchers have explored the addition of other materials to PCM for improved battery thermal performance in references [51], [52], [53].

The investigation of heat pipes as a method for thermal management was reported in [54]. The study was done on a module containing sixteen prismatic lithium-ion cells, and heat pipes were arranged to form a mat. The ‘heat mat’ was positioned under the battery module, absorbing the heat from the battery, and transferring it to an external cooling medium (water or refrigerant in this study). This method was able to control the battery temperature difference to within 1 ºC and maintained the battery temperatures below 30 ºC for battery operations under representative duty cycles conditions for electric vehicles. The use of heat pipes or plates alone in literature were found to be insufficient for thermal management and thus are often coupled with air or liquid cooling for improved thermal performance. A summary of literature that investigate the performance of heat pipes in BTM systems can be found in [37].

2.3.3 Hybrid Battery Thermal Management

Active and passive BTM may be considered for BESS applications for reasons including cost, simplicity, thermal performance, etc. However, both categories have limitations alongside the

benefits. Thus, hybrid BTM is common for BESS applications to maximize thermal control. Hybrid BTM systems may be a combination of active and passive BTM systems such as heat pipes with liquid flowing through for better heat exchange, two passive BTM systems such as heat plates and PCM together, two active BTM systems such as liquid cooling within the battery and forced convection in the ambient environment [37].

Zhao et al. in [55] did an experimental study on the coupled effect of PCM and heat pipes on thermal performance for power batteries containing cylindrical cells. The report shows that PCM only BTM systems accomplished a temperature difference reduction of 33.6% compared to air BTM systems, however integrating with the heat plate further reduced the difference by another 28.9% resulting in a temperature difference within the battery of less than 5 ^{o}C. The heat pipe provided support by absorbing heat from the battery and storing it before release to the PCM. This ensures more time for heat absorption and phase transition in the PCM, which has significant effect in cooling the battery and keeping the battery peak temperature below 50 ^{o}C.

A numerical study in [56] combines two active cooling strategy; forced gas and liquid cooling for BESS application in space. The set up is such that a cool plate, which passes liquid coolant through, is placed beneath the battery module, absorbing the heat generated from the battery. The heat is transported from the battery through conduction, radiation and forced air convection using a top fan, in the battery enclosure. Different fan positions and sizes were investigated for thermal performance and compared with the thermal performance of only natural convection. Optimization was achieved when forced convection was introduced at the bottom of the battery. The peak temperature was reduced by 3.45 ^{o}C from 47.8 ^{o}C, where only natural convection is considered and temperature difference within the pack was reduced from 17.3 ^{o}C to 13.6 ^{o}C. The thermal performance of the integrated method showed a significant dependence on the forced convection in the battery enclosure.

2.4 Thermal modeling of Lithium-ion Cells

Thermal modeling of lithium-ion batteries is a way to describe the thermal behaviour of batteries during their operation [15]. This includes the heat generation within the battery and the heat dissipation out of the battery into its external environment. Many studies have been done on battery thermal modeling for both research purposes and battery thermal management. The development

of thermal models in existing literature often takes into consideration the design features, as well as the operation variables and conditions. The thermal behaviour of lithium-ion batteries may be described with simplified spatial and/or temporal one-dimensional models, two-dimensional models, or complex three-dimensional models [15], [57]. They may also be developed as a lumped model. Often times, developed thermal models are coupled with electrochemical models or equivalent circuit models defining the thermal behaviours as a function of the electrochemical processes in the battery or the operational characteristics of an electric circuit [58].

Bernardi et al. in [10] developed a founding but rather complicated model, deriving a general energy balance equation, which describes the heat generation in a battery. The model involves rather complex processes like electrochemical reactions, phase changes in the battery, the electrical work done, the mixing effects, and changes in the heat capacity. This requires considerable parameterization; hence the equation was simplified, ignoring the heat due to mixing effects, phase change, and considering a single-cell reaction [59], [60]. Many researchers and literature have adopted the simplified equation, amongst other equations, in developing new electrochemical thermal models. Bernardi's simplified equation for heat generation in a battery is written in equation 1.

$$Q = I(V_{ocv} - V) - IT\frac{\partial V_{ocv}}{\partial T} \tag{1}$$

The term Q is the heat generation rate. I, V and T are the current, terminal voltage and battery temperature respectively. V_{ocv} is the open-circuit voltage, and $\frac{\partial V_{ocv}}{\partial T}$ is the temperature derivative of the open-circuit voltage. The first term on the right side of the equation describes the irreversible heat generation in the battery and the second term describes the reversible heat in the battery. The irreversible heat generation can be further simplified by defining an overpotential resistance, R as the difference between the open-circuit voltage and terminal voltage, divided by the current, $\frac{V_{ocv}-V}{I}$. Thus, the irreversible heat can be expressed as I^2R. The equation 1 can be then written as

$$Q = I^2R - IT\frac{\partial V_{ocv}}{\partial T} \tag{2}$$

At low C-rates (above 2-hour rate), the reversible heat (entropic heat) contributes makes up a significant proportion of the total heat generation (approximately 60%) and is also dependent on the state of charge of the battery. The entropy coefficient is high at low states of charge (0-20% SOC) and decreases by more than 80% between 20%-100% SOC. At higher C-rates, reversible

heating contributes only about 5% of the total heat generation [16]. Chen et al. in [61] developed a three-dimensional thermal model to investigate the heat generation and dissipation under constant current and dynamic power output conditions. The model was useful for describing the temperature profile and temperature distribution within the battery, providing insight for battery thermal management strategies. This work has been used to evaluate different arrangement of cooling and heating channels, and the choice of heating, cooling or insulation materials used in battery design. The work in [62], develops an electrochemical-thermal model for studying the impact of discharge rate, and the ratio of negative to positive electrode capacity, mainly attributed to the thickness of the electrodes, on the heat generation of a battery. This study is helpful for battery design as well as determining appropriate BESS applications as a function of the heat generation of the battery. A coupled thermal-electrochemical battery model is produced in [63], to describe and predict both the thermal response of a battery and the electrochemical behaviours by combining the thermal energy equation with other electrochemical models based on the temperature dependent properties of the battery. The model provides a tool for predicting the cell electrochemical and thermal behaviours for different charge modes, and to identify mechanisms responsible for thermal runaway.

The common theme with battery thermal modeling is that they focus on the heat generation and transport within the battery and are geared towards improving battery design and BESS thermal management. However, they differ in the mode of heat generation prediction adopting either experimental data or electrochemical models [15]. Simplified battery thermal models as in [64], [65], [66], [67] often do not consider the electrochemical reactions, visualizing the battery as a solid homogenous body having average thermal properties with a heat source. These types of models require fewer computational parameters and less processing time, making it easy to implement and understand. However, the accuracy of these models is limited as the model adopts average values and assumes homogeneity ignoring the internal variations of the battery thermal properties. They are beneficial where comprehensive electrochemical understanding is not required, providing a means for visualizing the temperature distribution of the system. More complex electrochemical thermal models as in [68], [69], [70], [71], [72] describe the battery's thermal dynamics more accurately, taking into account the electrochemical processes in the battery. However, they require numerous parameters and long processing time, making the model complex. They are useful for visualizing the temperature distribution as well as evaluating battery

performance as a function of temperature. The increased accuracy of electrochemical thermal models compared to simplified thermal models provide increased reliability of results, reducing the need for complex experimental study.

Many battery models concentrate solely on the internal aspects of the battery, without conducting an independent examination of the external environment. This presumes that the environment inherently possesses thermal management capabilities. The focus of this thesis is on the thermal dissipation in the surrounding environment rather than within the battery, evaluating the effect on battery temperatures and by extension, battery operations. The model is developed to provide a framework for studying subterranean battery thermal dynamics and may be applied for exploring BESS operations and performance. Thus, the model is a simplified thermal model assuming homogeneity of materials and adopts average values. A complex electrochemical thermal model is not necessary for this study as the comprehensive details of the battery is not required to investigate a new application or environment for battery operation. In addition, battery manufacturers may design battery units differently, however, the heat released to the environment is ascribed to the signal based on the application.

2.5 Subterranean Environment

The subsurface level of the earth contains materials including soil and rocks with unique thermal properties. The soil is a porous media, which is a composite mixture of minerals, organic matter, liquid, and gases, which varies with location. The typical composition of soil by volume is,

- 45% Minerals: This comprises of clay, silt, gravel, sand, and stones,
- 25% Water: this varies with the level of precipitation and the holding capacity of the soil.
- 25% Air
- 5% Organic matter

Over time, the physical properties of the soil, including the thermal properties, are influenced by climatic factors and activities of living organisms [73].

The rate at which temperature changes in the soil reduces with depth. The depth of influence of diurnal climatic changes reaches within the first 0.8 m below the surface, and the influence of seasonal climatic factors on the changing soil temperatures reach only to an approximate depth of 10 – 20 m, depending on the geographical location and soil properties [74]. The geothermal

gradient, defined as the rate of change in soil temperatures with respect to increasing depth, has an approximate value of 25 – 30 ºC per km [75]. This means that the soil temperatures beyond 20 m, and within a depth range of 1 m in the earth's crust stay within 1 ºC, and the average annual ground temperature increases by 1 ºC per 50 m [76]. The annual temperature fluctuations in the ground at different depths in Ottawa, Canada is illustrated in Figure 2.

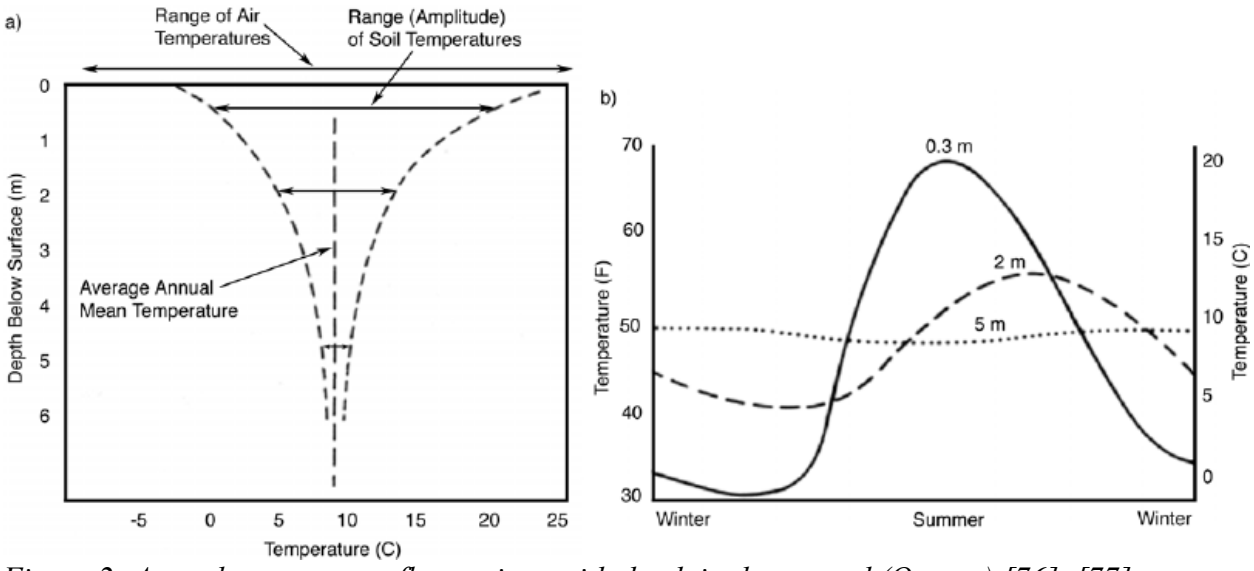

Figure 2: Annual temperature fluctuations with depth in the ground (Ottawa) [76], [77].

For installations situated beyond 2 m depth, the effect of temperature fluctuations decreases with depth, and becomes negligible beyond 20 m, which is helpful for applications where isothermal conditions are of importance. Many studies have been done on the subterranean environment, exploring the feasibility of engineering applications such as nuclear energy waste disposal, buried electrical cables etc. [77], [78], [79], [80], [81]. However, the installation of BESS underground has hardly been explored and the understanding of the heat flow in the soil is necessary as the thermal behaviour is crucial to the operation and performance of the battery. The literature [82], analyses the thermal properties of soil (thermal conductivity, heat capacity, and density) for underground battery operations. The study explores heat transfer mechanisms from the battery to the soil, considering the effect of surface thermal conditions on the temperature distribution of the battery where it is situated close to the surface, and avoiding earth heating through the bottom of the battery. The battery use case for the study applies to providing uninterrupted power for remote telecommunication devices, requiring low power. Unlike the work done in [82], the project in this thesis explores the soil thermal dynamics as a function of BESS operation, at depths where surface

climatic factors have limited effects and earth heating is avoided. Thus, heat is transported radially from the battery through the soil. The battery application is towards residential energy use cases adopting higher power signals with higher heat generation in the battery.

2.5.1 Soil Thermal Dynamics

The soil thermal dynamics describe the changes and movement of thermal energy within the soil. This involves three thermal processes in the soil: heat generation, heat transport and heat storage.

The generation of heat in the earth may be attributed to two sources in almost equal proportions: radiogenic heat and primordial heat. Radiogenic heat generation is due to the decay of radioactive materials present in the earth's mantle and crust, which releases heat in the process. Primordial heat is the residual heat in the earth's core originating from the earth's formation. The heat in the earth is transported outward towards the earth's surface along the geothermal gradient [83].

The transport of heat in a porous media like the soil, may be through conduction, convection, or radiation. Heat transport through radiation, in the lithosphere of the earth is negligible [84]. The effect of radiation in sand is less than 1% of the overall heat transfer under normal atmospheric temperatures, and thus is ignored. The heat transport by convection is attributed to the fluids contained in the soil. This is particularly influenced by the flow of the liquid and gas in the soil. The heat transfer in the soil by conduction occurs through particle contact in the soil without the need for movement of the particles [85]. The dominant heat flow mechanism in the soil is conduction. Convection and radiation have relatively small or negligible effects [74].

The thermal energy storage capacity of the soil is determined by its volumetric heat capacity, which is a function of the specific heat capacities of the material composition of the soil, and the density of the soil.

The thermal dynamics of a soil having isotropic, homogenous properties may be mathematically defined by the general heat equation.

$$\lambda\frac{\partial^2 T}{\partial x^2}+\lambda\frac{\partial^2 T}{\partial y^2}+\lambda\frac{\partial^2 T}{\partial z^2}+\ddot{Q}=\frac{\rho C_p \partial T}{\partial t} \tag{3}$$

The first three terms on the left-hand side of the equation 2 describe the heat transfer in the directions of x, y, z, which is a function of the thermal conductivity *(λ)* and the change in temperature *(T)*. The fourth term '$\ddot{Q}$', represents the internal heat generation inside the soil. The

term on the right-hand side of the equation describes the energy stored in the soil expressed as a function of the specific heat capacity *(C_p),* density *(ρ),* and the change in temperature, *T* with time *(t)* in the soil [86].

The combined effect of thermal energy generation, heat transport, and storage is exhibited by temperature changes in the soil with time and/or spatial dimension, and is dependent on its varying thermal properties (heat capacity and thermal conductivity) [87]. Thus, thermal models predicting the thermal behaviours in the soil require the consideration of the thermal properties.

2.5.2 Thermal Properties of Soil

The thermal properties of the soil primarily depend on the mineral composition, porosity, and moisture content in the soil [88]. Three primary soil types exist as determined by soil scientists, which are sand, silt and clay. The variety of existing soils may be classified by texture using the percentage of the three soil types present in the soil. The sand in a soil sample is identified by the mineral particles of diameters ranging from 2 to 0.05 mm, the portion of the soil sample that contains the mineral particles of diameters ranging from 0.05 to 0.002 mm is recognized as silt, and soil composition with mineral particle size that are less than 0.002 mm in diameter is identified as clay. The soil texture is strongly related to the soil porosity, water retention and diffusion of fluids in the soil, which in turn influences the soil thermal properties [89]. A classification of soil types by the texture is presented in Figure 3 below.

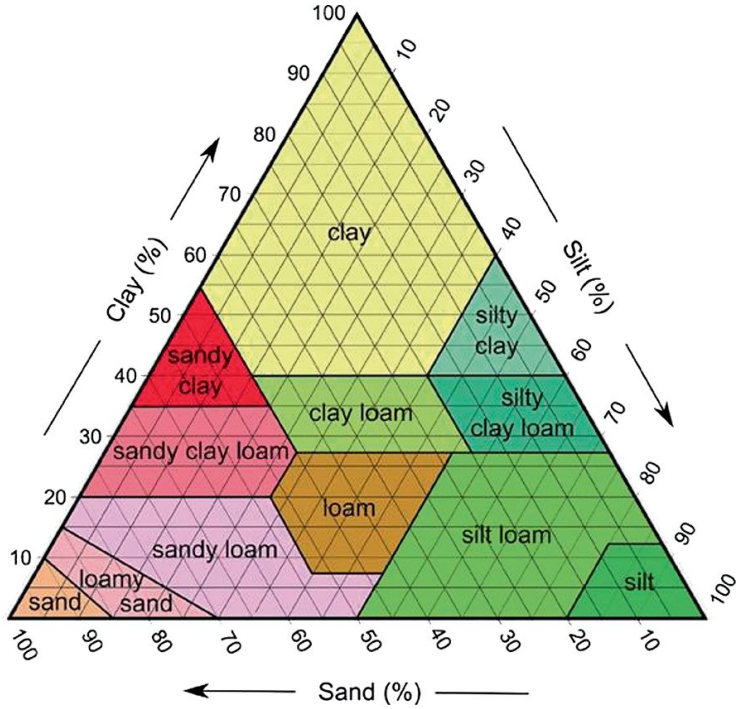

Figure 3: soil types by texture [91]

Soils with a high average particle size like sand and sandy loam, consist mainly of large pores (macro-pores). The flow of water by gravity is unrestrained for these types of soils, and thus water retention is poor. A smaller average of particle sizes in the soils e.g. clay, silty clay, contain smaller pores. The close bond between the particles provides higher water retention abilities against the force of gravity. [90], [91].

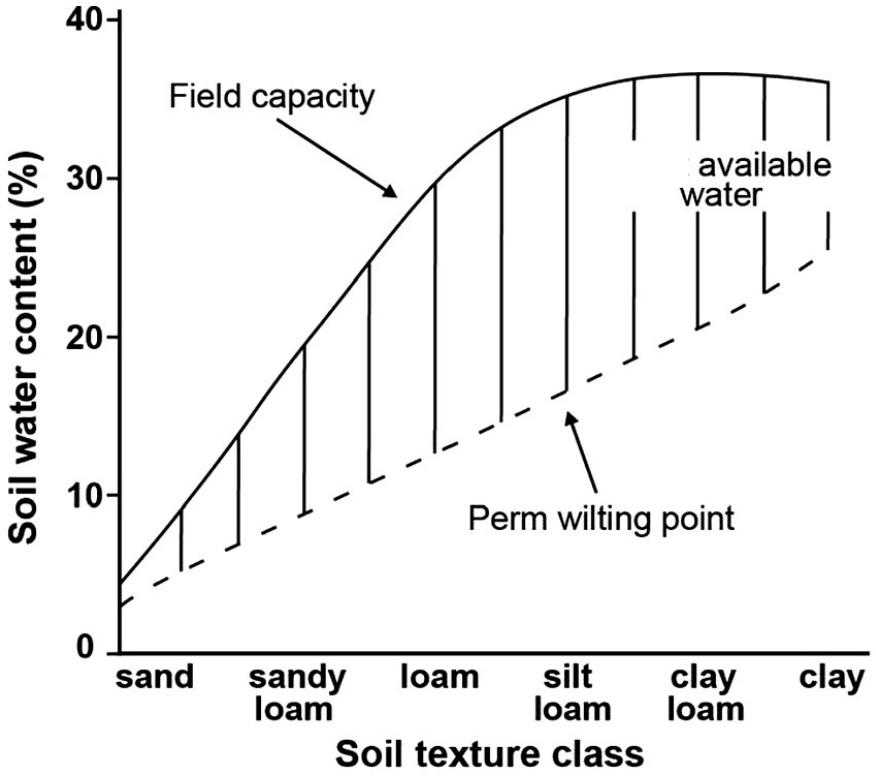

Figure 4: Soil moisture content capacity according to texture adapted from [91]

The Figure 4 shows the water content capacity of different soils based on the texture. The field capacity refers to the water content of the soil after saturation point has been reached and the soil is allowed to drain freely. The loss of moisture from the soil may be due to gravitational drainage, evaporation, or plant use. As water is lost in the soil, the force between the mineral particles and water becomes stronger and more energy is requires for water to move. The wilting point describes the point at which organisms in the soil can no longer used the water in the soil [90], [91]. There are two main soil thermal properties with significant influence on the thermal behaviour shown by the heat equation (equation 3). These are the heat capacity, and thermal conductivity [92].

Thermal Conductivity

Thermal conductivity is a fundamental property that characterizes heat transfer in a medium. The thermal conductivity of any soil is defined as the quantity of heat transported per unit time through a unit cross-sectional area of the soil under a unit temperature gradient in the direction of the flow of heat [74]. The thermal conductivity of the soil varies from the influence of several factors.

However, the primary factors that affect thermal conductivity are the mineral components of the soil, porosity, and water content [93].

The thermal conductivity of soils varies due to the mineral composition. The thermal conductivity of typical soil minerals ranges from 1.70 to 10.68 $Wm^{-1}K^{-1}$ (Table 2). The least thermal conductivity for any soil mineral is 1.70 $Wm^{-1}K^{-1}$, which is sixty-five times that of air which is 0.026 $Wm^{-1}K^{-1}$. Therefore, the impact of mineral composition on soil thermal conductivity is not negligible, especially for dry soil with significantly more pores than moist soil. Summarily, the volume fraction of the distinct minerals in the soil influences the thermal conductivity. Soil containing higher volumes of minerals with higher conductivity, naturally will transport heat better [94].

A soil has a distribution of particle size which decides its density and porosity. The particles may be coarse (particle sizes > 0.5 mm) or fine particles (particle sizes < 0.5 mm) [95], [96]. Soil containing coarse particles may be packed together in many ways and determines the number of contact points between the particles, which determines the porosity. Increased contact between the particles means fewer pores and consequently better heat transfer. Soil containing fine particles hold smaller particle sizes and they have smaller but numerous pores compared to coarse-particle soil. Hence porosity is higher for fine-particle soil and thermal conductivity is lower [74], [97]. Naturally occurring soil may contain a mixture of fine and coarse particle sizes and have intermediate pore distribution sizes and consequently dynamic heat transfer behaviours. In summary, the soil porosity is inversely related to the thermal conductivity of the soil, mainly due to three factors, the quantity of solid matter per unit soil volume, air, or water pores per unit of soil volume, and heat transfer across the particle contacts [74].

The effect of moisture content on thermal conductivity is one that has been study in literature for various soil types. The thermal conductivity of water is 0.598 $Wm^{-1}K^{-1}$ at 20 ^{o}C, which is 25 times that of air. Hence, the addition of moisture in the soil increases the thermal conductivity as air-filled pores are replaced with water-filled pores. However, the effect of increasing moisture content in the soil varies according to soil type. Generally, the rate at which soil thermal conductivity increases is higher at lower moisture content. Continuous addition of moisture has less effect beyond a moisture level of 20% [74].

Heat Capacity

The thermal capacity of the soil is the amount of heat required to cause a temperature change in the soil. The thermal capacity is fundamental to thermal storage and is dependent on the mass, and the specific heat capacity of the material composition [98]. The thermal capacity of the soil is determined by the addition of specific heat capacities of its individual mineral components based on their proportions. The heat capacity can be varied across a narrow range, influenced by moisture content and soil density. This behaviour is distinct to the soil type. Like thermal conductivity, the heat capacity of soil increases almost linearly with increasing moisture content up to 15%. However, for sandy soil, continuous increase in moisture content above 15% has a limited effect on increasing the heat capacity further. In contrast, clay soils exhibit significant further increase in heat capacity with more water added until a saturation point is reached (approaching 30% volumetric water content [99]) [87]. A summary of the specific heat capacity of different soil types at different moisture content is presented in the table below.

Table 1: Specific heat capacity for different soil types and water content [100]

SOIL TYPE	WATER CONTENT (%)	SPECIFIC HEAT CAPACITY (C_P) / $J.g^{-1}K^{-1}$
China clay (D)(saturated)	46.2	2362
China clay (D)(dry)	0	800
Sandy clay	26.5	1696
Sandy clay	19.5	1459
Soft dark grey sandy gravely clay	28.5	1764
Soft grey fine sandy clay	54.6	2646
Soft grey fine sandy clay	41.4	2200
Stiff dark grey sandy gravely clay	10.1	1141
Stiff dark grey sandy gravely clay	9.6	1125
Stiff dark grey-brown sandy gravely clay	9	1104
Very soft grey fine sandy clay	46.2	2362
Grey slightly silty sandy gravel	11.1	1175
Grey limestone (very hard)	0.1	803
Coarse sand (dry)	0	800
Coarse sand (saturated)	20.2	1483
Dark grey clayey fine sand/silt	28	1747
Fine sand (dry)	0	800
Fine sand (saturated)	24.6	1632
Made ground (Silty gravely sand)	13.9	1270
Medium sand (dry)	0	800
Medium sand (dry)	20.3	1483

Thermal Diffusivity

The thermal diffusivity of a soil is the ratio of the thermal conductivity to the volumetric heat capacity. This is related of the rate of change in soil temperatures due to heat conduction. The thermal diffusivity value is directly related to the temperature change rate i.e., the higher the thermal diffusivity, the faster the temperature changes are transmitted through the soil. The

dependence of diffusivity in both thermal conductivity and heat capacity means that it is influenced by all the factors affecting both parameters. [101].

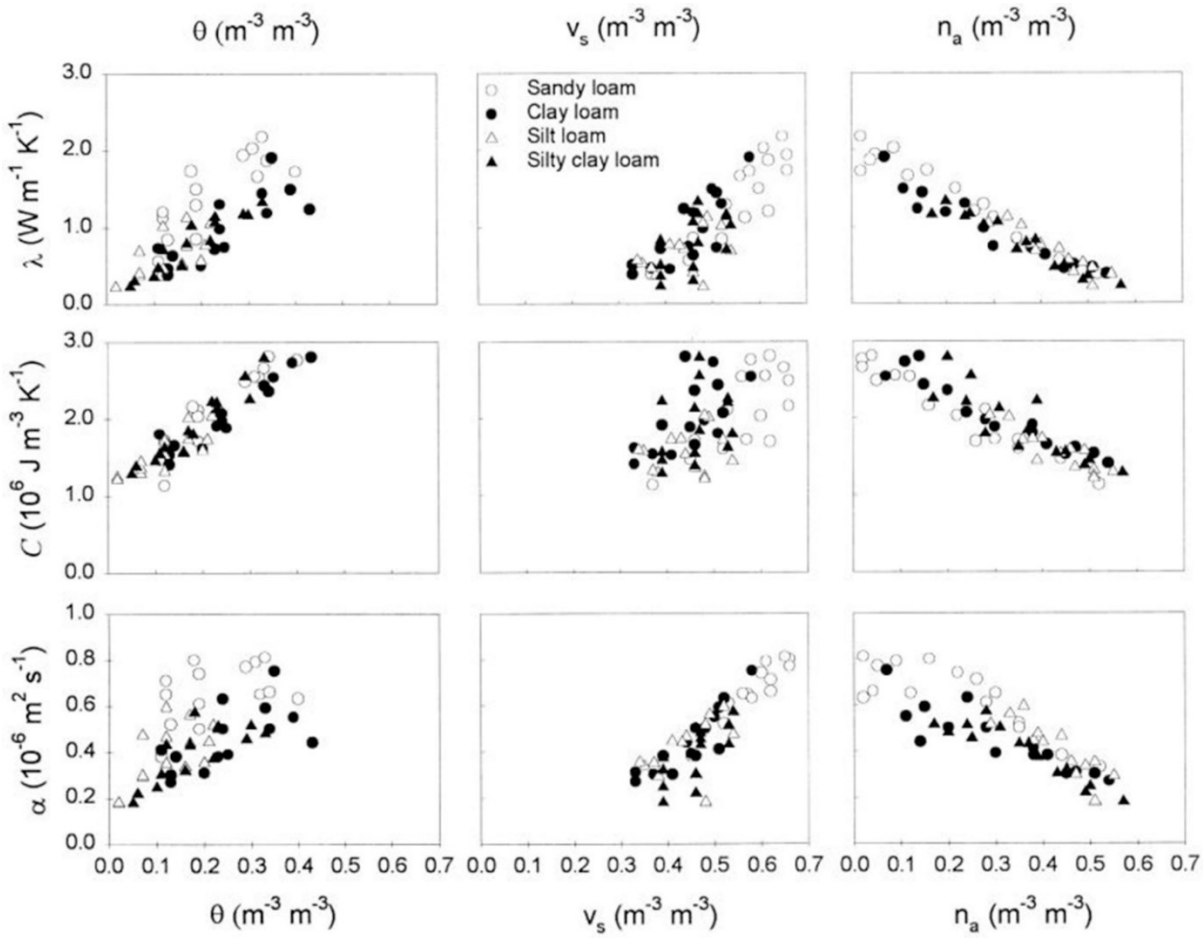

Figure 5: Soil thermal properties: Thermal conductivity (λ), heat capacity (C), and thermal diffusivity (α) versus volume fractions of water (Θ), solids (v_s), and air (n_a) for four medium-textured soils [92].

Figure 5 obtained from [92] illustrates the influence of the volumetric content of moisture, solid matter (i.e. mineral composition), and soil air porosity on the thermal conductivity, volumetric heat capacity and thermal diffusivity of soil. The figure shows a strong correlation of the thermal conductivity to porosity of the soil. The effect of air porosity proves to be the dominant influence in soil thermal conductivity compared to that of moisture content and soil mineral composition. It is shown that the volumetric heat capacity of the soil is influenced by both the moisture content and soil porosity in almost equal measure, whereas the effect of the volume fraction of the minerals come secondary. The thermal diffusivity being a ratio of both thermal conductivity and volumetric heat capacity shows a dependence on soil porosity as is the case of thermal conductivity and

volumetric heat capacity. The figure also shows a strong correlation of volume fraction of solid minerals present to the thermal diffusivity, but less influence of moisture content due to the thermal diffusivity being a ratio of thermal conductivity and heat capacity.

Table 2: Soil mineral components and their thermal properties [94], [102], [103].

MINERAL	**THERMAL CONDUCTIVITY (K) / $W.m^{-1}k^{-1}$**	**SPECIFIC HEAT CAPACITY (C_P) @ 20°C / $J.g^{-1}K^{-1}$**	**DENSITY (ρ) / gcm^{-3}**	**VOLUMETRIC HEAT CAPACITY (C_V) @ 20°C / $J.cm^{-3}K^{-1}$**	**THERMAL DIFFUSSIVITY (α) / 10^6 m^2s^{-1}**
Albite	2.50	0.730	2.62	1.91	1.31
Amphibole	2.81	0.749	3.20	2.40	1.17
Anhydrite	4.80	0.585	2.95	1.73	2.78
Anorthosite	1.80	0.840	3.50	2.94	0.61
Basalt	1.70	0.840	2.87	2.41	0.71
Calcite	3.60	0.815	2.75	2.24	1.61
Chlorite	3.01	0.600	2.80	1.68	1.79
Diabase	2.30	0.860	2.79	2.40	0.96
Dolomite	5.50	0.900	2.80	2.52	2.18
Feldspar	2.25	0.790	2.70	2.13	1.05
Gabbro	2.20	1.000	3.00	3.00	0.73
Gneiss	2.60	0.979	2.70	2.64	0.98
Hematite	10.68	0.620	5.15	3.19	3.34
Hornblende	2.81	0.710	3.08	2.19	1.28
Kaolinite	2.00	0.974	2.65	2.58	0.77
Mica	2.03	0.770	3.00	2.31	0.88
Microcline	2.44	0.700	2.58	1.81	1.35
Plagioclase	2.00	0.730	2.60	1.90	1.05
Quartz	7.70	0.740	2.42	1.79	4.30
Siderite	3.00	0.740	3.90	2.89	1.04

2.6 Depth for Battery Installation

The allocation of infrastructure underground requires careful consideration of the dynamics of the conditions of the environment relative to the operation of such infrastructure. These considerations include the ground or soil conditions, nature of infrastructure, and installation depth. The soil conditions have been discussed in the section 2.5, and the nature of infrastructure (i.e., BESS) in the preceding sections of this chapter. The use of underground space for installation may be classified by the depth of installation, summarized in Table 3.

Table 3: Typical range of depth according to use (in meters) [104]

CATEGORY	LOCAL UTILITIES	BUILDINGS	REGIONAL UTILITIES (TRANSIT)	MINES
Shallow	0 – 2	1 – 10	0 – 10	0 – 100
Medium	2 – 4	10 – 30	10 – 50	100 – 1000
Deep	> 4	> 30	> 50	> 1000

BESS use may be grouped under local utilities or buildings infrastructure, therefore the depth of installation considered, depending on the size, may range from 0 – 10 meters in the ground. An added consideration for depth of BESS allocation in the ground is the temperature conditions, which may influence the battery operations (the effect of temperature on lithium-ion batteries are discussed in section 2.2).

The influence of surface climatic factors on the ground temperature provides a means of determining a range of depth prescribed for BESS installations. The surface climatic changes including temperature fluctuations, have undesired effects on battery operations. Therefore, soil depth within 0 – 1 m below the ground surface are not the best for BESS installations as diurnal climatic changes have prominent effects on ground temperatures within this range. The annual temperature changes are evident up to 10 m below ground surface and decreases with depth. The seasonal amplitude of ground temperatures at a given depth is dependent on the surface amplitude which changes with geographic location. For ground depth between 1 – 10 m, ground temperatures are not rapidly changing and present no adverse effect on the battery. Therefore, they are suitable for BESS installations. For additional layer of protection from surface climatic factors, no less 2

m below ground surface may be adopted for BESS installations. It may be concluded that a prescribed range for BESS installation underground is 2 – 10 m below the ground surface.

2.7 Summary

The literatures reviewed in section 2.1, 2.2 and 2.3 covers the thermal behaviour of lithium-ion batteries, discussing the processes of heat generation within a battery, and the thermal effects on the battery's electrochemical performance and degradation. It has been established that the operation of BESS within a range of desired temperatures is recommended, and the temperatures be maintained as uniformly as possible to within a 5 ^{o}C difference. The works reviewed provides information of the adverse effects of extreme temperatures and temperature difference within a battery. Battery models have been developed both empirically and numerically to describe battery behaviour including the thermal aspects. The findings from the literature have contributed to optimizing the performance of BESS and for research purposes.

Literature cited under battery thermal management discusses the different systems and strategy for managing and controlling battery heat generation and temperature, the influence of current rate and ambient temperatures are investigated. Studies have shown that active and hybrid thermal management strategies are preferred for most applications. The thermal management strategies in literature are developed for above-surface BESS installations and not investigated for sub-surface adoption. It is common for battery manufacturers to include a recommended temperature range in technical data sheets for lithium-ion batteries. This range typically spans from 0 to 45 ^{o}C for charging and -20 to 60 ^{o}C for discharge operations. Maintaining the recommended temperature range can be effectively supported by the installation of BESS underground, using the ground for passive thermal management. The ground soil around the battery may be carefully chosen based on the battery application and the environmental thermal requirements – whether as a heat sink or for heat storage. This research explores the performance of subterranean BESS operations with passive thermal management employed.

The literature cited under subterranean environment discusses the nature, material component and thermal properties in the soil. The factors influencing thermal behaviour in the soil is also reviewed. The reviews provide knowledge related to the heat transport media in this research, which aids the modelling of this work.

The installation of engineering infrastructure below ground surface is practical for limited applications. These include are pipelines, electrical power lines, and geothermal applications. The allocation of battery systems in the ground has not been explored. Literature in [78], [79], [105], [106] investigate the thermal performance of electrical cables. These studies focus on the soil as well as the conductor in their study. Electrical cables are within one to two meters deep in the soil, which is much closer to the surface where climatic factors influence the thermal properties significantly. Unlike electrical cables, batteries are more sensitive to temperatures as it directly affects their electrochemical processes. Hence, they need to be buried deeper where the thermal properties of the soil are more stable. In contrast, geothermal loops go much deeper in the ground, up to a few hundred meters deep [107]. However, the temperatures at this depth are very high, which is not favourable for battery operations. In addition, the heat generation for a battery is much different from that of electrical cables or geothermal heat pumps. Thus, the need for this study.

This thesis contributes to literature by modelling and evaluating the thermal behaviours of subterranean BESS operations using a numerical simulation approach and heat generation obtained from experiments which represent real life energy use profiles.

Chapter 3: Experimental Methodology

This chapter presents the experimental methods used to evaluate the thermal behaviour and limitations of subterranean battery operations. It discusses the experiments carried out for model validation. The content of this chapter describes the selection of the battery module, soil material, and test procedures. The sensors and equipment used for experiments are also described in this chapter.

3.1 The Battery

The battery used for this study is a Lithium-ion module containing cylindrical cells adhering to the 21700s size format, (i.e., 21 mm in diameter, 70 mm in length). Cylindrical cells are a popular format of Lithium-ion battery used for a wide range of applications including residential storage. The cells contain Nickel Cobalt Aluminum (NCA) material in the positive electrode, and silicon-graphite as the negative electrode material. The NCA battery chemistry possess high energy density and power capabilities due to the high Nickel content in the cell [108]. The material specifications for the cells are summarized in Table 4 below, directly sourced from the datasheet [109].

Table 4: Cell specifications

NOMENCLATURE	**CELL SPECIFICATION**
Nominal Capacity (Ah)	5
Nominal Voltage (V)	3.60
Charge Voltage (V)	4.20
Discharge cut-off Voltage (V)	2.50
Maximum Charge Current (C-rate)	1C @ 25°C
Maximum Discharge Current (C-rate)	3C @ 25°C
Internal Resistance (mΩ)	≤ 30
Weight (kg)	≤ 0.072
Storage Temperatures	1 year: -20 ~ 25 °C, 3 months: -20 ~ 25 °C, 1 months: -20 ~ 25 °C

The module is designed as one side of a hexagonal shaped pack with six modules, and thus to achieve industry standard working voltages of approximately 600 VDC, the maximum voltage of the module does not exceed 100 VDC. To stay within this range and keep within a one-meter diameter for the pack, the chosen module configuration is 22S24P i.e., twenty-two cell groups in series each containing twenty-four cells connected in parallel. The module is sized to an Amp-hour capacity of 120 Ah, with an energy capacity of 10 kWh. The battery module is shown in Figure 6.

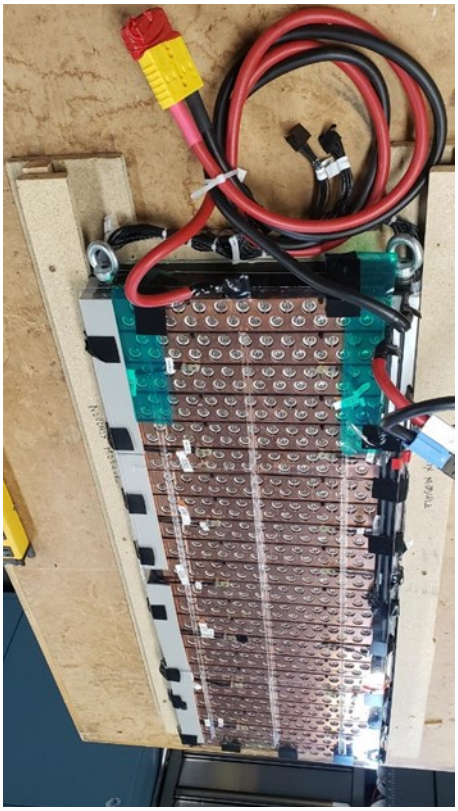

Figure 6: 120 Ah Battery module

The module specification is determined based on the cell information, and the cell configuration in the module. Nominal capacity is determined as the added nominal capacity of the cells in parallel and the module voltage is determined by the added voltage of the number of cell groups in series. The total internal resistance of the module is determined based Ohm's law, and the number of cells in series and parallel.

Table 5: Module specifications

NOMENCLATURE	MODULE SPECIFICATION
Nominal Capacity (Ah)	120
Nominal Voltage (V)	79.2
Charge Voltage (V)	92.4
Discharge cut-off Voltage (V)	55.0
Maximum Charge Current (C-rate)	1C @ 25°C
Maximum Discharge Current (C-rate)	3C @ 25°C
Internal Resistance (mΩ)	$\leq$ 27.5
Weight (kg)	$\leq$ 40
Storage Temperatures	1 year: -20 ~ 25 °C, 3 months: -20 ~ 25 °C, 1 months: -20 ~ 25 °C

3.1.1 The Battery Thermal properties

The thermal properties of the battery are a function of the separate components in the module, which comprises the cells, a cell holder, and a thermally conductive gap pad. The thermal properties discussed here are the thermal conductivity and the heat capacity of the battery. The thermal properties for the cell are not stated in the technical datasheet, hence, estimated values based on published literature are adopted. 21700 NCA cylindrical cells possess a thermal conductivity of 0.83 $Wm^{-1}K^{-1}$ in the radial direction and 11.55 $Wm^{-1}K^{-1}$ in the axial direction (i.e., along the current collector inside the cell) [110]. The heat generated in the cell is transported through the backplate and into the soil, hence the axial conductivity is used. The heat capacity for NCA cell range from 0.8 to 1.1 $Jg^{-1}K^{-1}$ in published articles (Table 6), thus, a value of 1 $Jg^{-1}K^{-1}$ is chosen. The cell holder which houses each cell is a material made of modified Polyamide 6, reinforced with glass fibre and mineral, and halogen free flame retardant. The thermal conductivity of the material is 0.8 $Wm^{-1}K^{-1}$, and the heat capacity is 1.3 $Jg^{-1}K^{-1}$. A thin layer of thermally conductive gap pad is spread at the back of the battery cell holder. This material has a thermal conductivity of 1 $Wm^{-1}K^{-1}$ and heat capacity of 1.3 $Jg^{-1}K^{-1}$, estimated from published articles. Heat

flows from the cell into the cell holder and through the thermal gap pad out of the module. Table 7 summarizes the values of the thermal properties of the module.

Table 6: Heat capacity of NCA battery in published literature

REFERENCE	**HEAT CAPACITY ($Jg^{-1}K^{-1}$)**
[111]	0.9585
[112]	0.83 ± 0.019
[113]	0.825 – 0.92
[114]	1.11
[115]	1.07
[116]	1.047
[117]	0.946
[118]	1.05 ± 0.05

Table 7: Battery Module thermal properties

COMPONENT	**THERMAL CONDUCTIVITY ($Wm^{-1}K^{-1}$)**	**HEAT CAPACITY ($Jg^{-1}K^{-1}$)**
Battery cell	11.55	1
Cell holder	0.8	1.3
Thermally conductive gap pad	1	1.3

3.2 The Soil

The soil chosen for this experiment is a specialized backfill with similar properties and compositions as geographical locations with tropical climates like Florida. The soil is a low-strength soil (2 MPa), which is a mix of fine-coarse sand containing silt, clay, cement, and water.

The soil was tested in a geothermal research laboratory where several trial mixes of the composite material containing varying proportions of each were produced to achieve a consistently high-slump and non-segregated slurry. The thermal conductivity was desired to be greater than 1.00 $Wm^{-1}K^{-1}$, at zero percent moisture content. The soil composition and properties are presented in Table 8, sourced from the datasheet.

Table 8: Soil properties and composition

COMPONENT	**PROPERTY**	**VALUE**	**UNIT**
3/8" Aggregate 530	dry density	530	kgm^{-3}
Fine sand (Jahna green bay sand) 910	dry density	910	kgm^{-3}
Cement	dry density	225	kgm^{-3}
Water	volume m^3	420	kgm^{-3}
Slump	particle size (mm)	~200	mm
Mixed soil	dry density	1650	Kg m^{-3}
Mixed soil (dry)	thermal conductivity	1.15	$Wm^{-1}K^{-1}$

3.2.1 The Soil Thermal Properties

Adequate heat conduction is desired in this experiment. Therefore, the soil thermal properties desired for experimentation are of significant importance. The mineral composition, porosity, and moisture content were considered carefully because these properties have a direct impact on soil thermal conductivity. The heat capacity of the soil is also of importance in this experiment, which is related to the mass of the soil. To satisfactorily conduct the heat from the battery, the selected soil contains a 10% volumetric water content (VWC), with a thermal conductivity of 2.00 $Wm^{-1}K^{-1}$. The heat capacity is estimated to be 1 $Jg^{-1}K^{-1}$. The soil thermal properties are summarized in Table 9 below.

Table 9: Thermal properties of selected soil

PROPERTY	VALUE
Thermal conductivity	2.00 $Wm^{-1}K^{-1}$
Moisture content	10%
Mass	2000 kg
Heat capacity	1 $Jg^{-1}K^{-1}$.

3.3 Test Unit Design and Construction

A vertical trapezoidal prism box is built, which represents one part of the hexagonal battery pack and allows for heat dissipation radially. Due to the symmetrical attributes of the hexagonal shape, the single sided representation is sufficient for this study. The set-up is assembled such that the battery module sits in front of a stainless steel backplate in contact with the soil, which serves to transport the heat from the battery into the soil. The interior of the box, which contains the soil, is lined with a vapour barrier to prevent loss of soil moisture through the wall of the box. An isothermal cavity is built at the back of the enclosure, which houses a heater element, a cooling fan and two circulating fans to maintain a constant temperature of 30 °C with a tolerance of $\pm$0.5 °C. Outside of the range a thermal controller initiates heating or cooling as required. The isothermal cavity represents the undisturbed soil temperatures further away from the battery. ECH20 EC-5 Moisture sensors are positioned midway between the battery and the isothermal cavity, along the height of the box at heights approximately one-third and two-thirds of the soil depth. Four temperature sensors (T-type thermocouples) each are positioned at three distances in the soil; at the back of the battery backplate on the soil side, midway between the battery and the isothermal cavity, and at the soil side of the isothermal cavity. The temperatures are positioned to measure temperatures with respect to time at four positions; center top, center bottom, side top, and side bottom, as heat from the battery is transported through the soil. The test unit is illustrated in Figure 7. To restrict heat flow to only the radial direction, the sides of the enclosure box and the battery (with the exception of the isothermal cavity) are insulated with twelve inches (0.3 m) of Soprema Polyisocyanurate insulation material with a thermal resistance (R – value) of 12 RSI. The heat transfer coefficient is calculated using Equation 16.

$$U = \frac{1}{R} \tag{4}$$

The heat transfer coefficient, U, is calculated to be 0.083 $WK^{-1}m^{-2}$. The heat transfer rate from the insulation is determined using Equation 17.

$$\dot{Q} = UA\Delta T \tag{5}$$

The soil temperatures, inside the enclosed box is kept at 30 ºC, and the outer environment of the box (i.e., laboratory temperature) is kept at 20 ºC. For a total surface area of insulation of 5.33 m^2, the rate of unintentional heat transfer through the insulation material was computed to be 4.4 W. For a typical aggressive load cycle on the battery in conditions of 20 ºC natural convection, the rate of heat loss is 55 W, and 71.5 W for 40 ºC forced convection. Therefore, less than 10% of the heat is lost through the insulation material and it is sufficient to restrict heat flow to more than 90% of the heat transferred radially through the back of the box.

Figure 7 below shows the test unit and the positions of sensor in the unit.

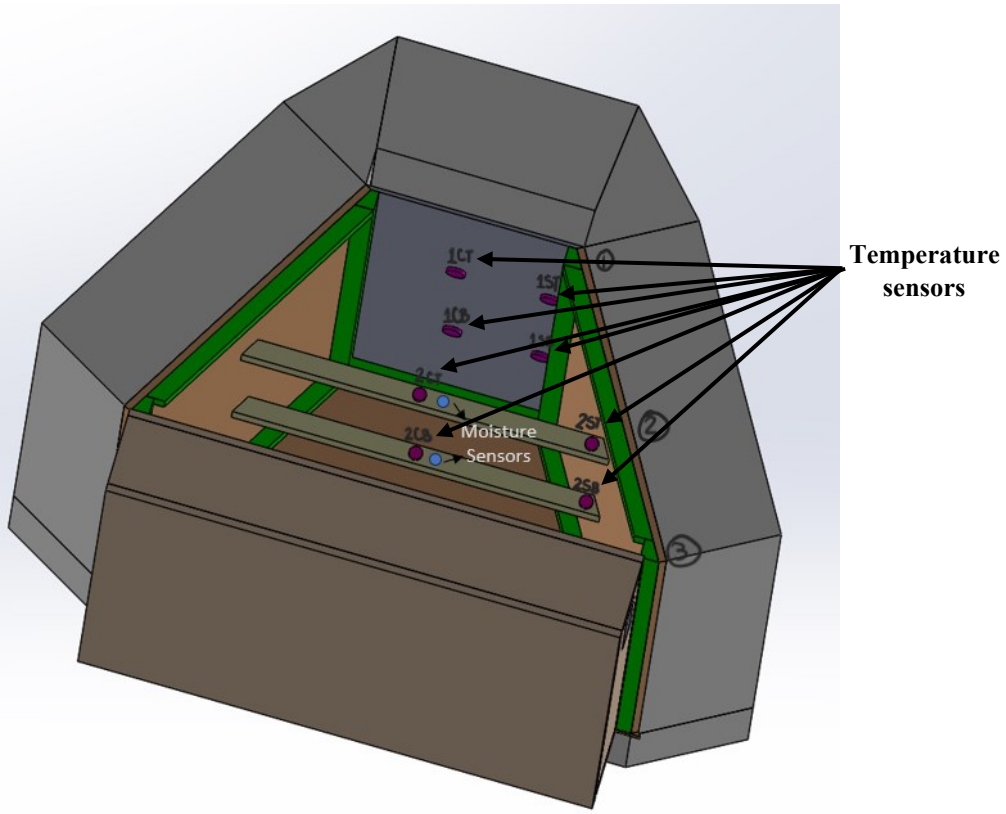

b: Isometric view

c: Side View

Figure 7: Test unit design showing sensor positions

(a) Wooden soil enclosure box

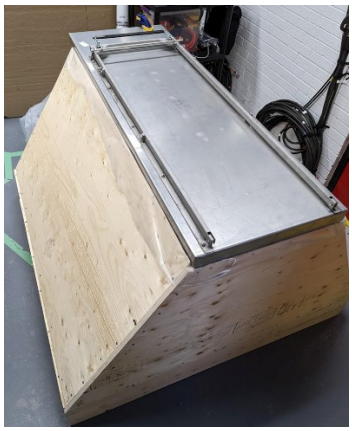

(b) Enclosure box fit with back plate

(c) Interior lined with vapor barrier

(d) Insulation being fitted

(e) Insulation glued to enclosure box

(f) Glued insulation held together using strap ties

(g): Isothermal cavity

(h): Soil compaction

(i) Soil-filled test unit

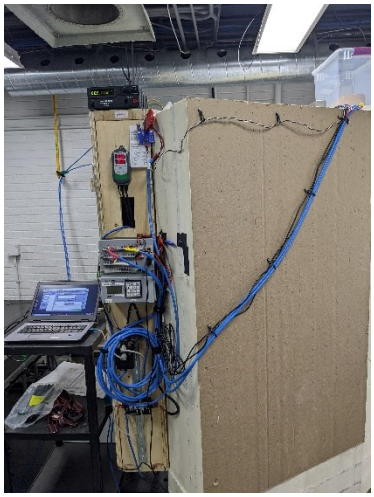

(j) Instrumentation of the unit

(k) Test unit with battery installed

(l) Completed test unit

Figure 8: Build progression of the test unit

3.4 Equipment

The tests done for the experimentation of subterranean battery operation involved the use of several equipment which includes a battery power cycler, battery management systems, measurement and data logging devices, and some other equipment.

3.4.1 Power Cycler

The battery power cycler was chosen to match the battery's voltage range and satisfy the desired cycling rate of the battery. A Gustav Klein battery power cycler operated with Greenlight Innovations Emerald software, is used for all the battery cycling necessary for this experiment. The cycler is designed with several layers of software- controlled and hardware features for reasons including safety. The unit is a grid regenerative cycler equipped with two channels. Each channel has a rated voltage range of 8 – 800 V, and a current rating of $\pm$200 A. The unit power rating of the unit is 100 kW.

Figure 9: GLI-GK battery pack cycler

3.4.2 Battery Management System

A battery management system (BMS) is necessary for measurement and regulation of the cell group voltages and temperatures in the module. The BMS also provides safety protection in the operation of the battery. An Orion battery management system including a thermistor expansion module (TEM) is used for this experiment. The BMS protects the battery by measuring the inputs

from cell voltage taps, total battery voltage and thermistors, and using the outputs to control battery charge and discharge. The BMS is set to keep the battery cell voltages within the limits of 2.5 V to 4.2 V. Balancing between the cell groups is initiated as soon as a cell group reaches a voltage of 4.2 V. The balancing of the battery is continuous until the difference between the cell group voltages is within 5 mV. The TEM is operated together with the BMS and is used for monitoring temperatures on the battery.

a: Orion BMS

b: Orion TEM

Figure 10: BMS devices

3.4.3 Measurement and Datalogging Devices

The measurement of parameters like temperature, moisture content, thermal conductivity, etc., were crucial for this experiment. The devices used for measurement and datalogging includes a weigh scale, multimeter, battery analyzer, temperature sensors, moisture sensor, datalogger, and thermal conductivity meter.

The datalogger used for recording soil temperature and moisture content levels is a Campbell scientific datalogger, CR5000. This is a high-performance data acquisition system with many input channels for large number of sensors. The CR5000's operating system includes measurement, processing, and output instructions for programming the datalogger.

A TEMPOS thermal property analyzer, TEM00001292, is used for measuring the soil thermal conductivity by passing current, generating a known amount of heat through a sensor probe into the soil, and measuring the temperature change in the sensor over a time period until a stable temperature is reached. The sensor is inserted with as little wiggle room as possible to prevent air

gaps and thermal drifts which may affect the output measurements. The operating temperature of the meter ranges from 0 - 50 ºC.

The temperature sensors used include T-type thermocouples and negative temperature coefficient (NTC) thermistors. These were used to measure temperatures at various points on the battery and inside the soil. ECH20 EC-5 moisture sensors are embedded in the soil to measure moisture content levels at different heights.

The scale, and the Fluke multimeter and battery analyzer were used for preliminary tests done on the battery and the soil.

a: CR5000 datalogger

b: TEMPOS thermal properties analyzer

a: Temperature sensor

b: ECH20 EC-5 Moisture sensor

c: Weigh scale

Figure 11: Measuring and datalogging devices.

3.4.4 Other Instrument Used

Other instruments used for this experiment includes a thermal chamber for preliminary soil density analysis, thermal controller, booster fans and circulating fans, and a heater element. A summary of the equipment used, their description and used are presented in Table 10.

Table 10: Equipment used for experiments.

DEVICE	**DESCRIPTION**	**USE**
GLI-GK battery pack cycler [119]	2 channels operated independently or in parallel, Voltage range per channel: 8 to 800 V, Current range per channel: -200 A to 200 A, Power rating: 160 kW	Charging and discharging the battery
Orion BMS [120]	Supports 180 cell inputs and equipped with isolation fault detection. Cell voltage measurement rating: 0 - 5 V, cell voltages resolution: 1.5 mV. Supply voltage: 12 V, active supply current: 250 mA. Cell balancing current: 200 mA.	Cell balancing, voltage regulation, and safety protection.
Orion TEM [121]	Supports 80 thermistor inputs. Operating temperature range: -40 to 80 °C. Supply voltage range: 10 - 16 V, supply current (@12V): 35 -60 mA	Battery temperature measurements
CR5000 datalogger [122]	Supports 40 single ended channels. System power requirements 11 - 16 VDC, baud rates: 1200 to 115200 bps.	Datalogging
TEMPOS thermal property analyzer [123]	Temperature range: 0 - 50 °C, sensor thermal conductivity range: 0.1 - 6 $Wm^{-1}K^{-1}$. Accuracy: $\pm$10%	Soil thermal conductivity measurement
Temperature sensors	T-type thermocouple, NTC thermistors	Temperature measurements

DEVICE	DESCRIPTION	USE
ECH20 EC-5 Moisture sensor [124]	Volumetric water content range: 0 - 100%, resolution: 0.001 m^3/m^3 VWC in mineral soils. Operating temperature range: -40 to 60 °C	Moisture sensing and measurements
Starfrit Weight scale	Max weight 100 g at ± 0.003 g accuracy	Mass measurements
Fluke 510 battery analyzer [125]	Voltage range ± 6 VDC at ± 0.09% accuracy, IR range 3 to 3000 mΩ at ± 0.8% accuracy	Voltage and IR measurements
Fluke 289 multimeter [126, p. 289]	Voltage range 0.05 to 50 VDC ± 0.025% accuracy, current range 500 µA to 10 A with ± 0.05% accuracy	Voltage measurements
Thermal controller (ITC-308) [127]	Temperature control range: -50 - 120 °C. Accuracy: ±1 °C, resolution: 0.1 °C. NTC sensor type. Mode: on or off (heating and cooling)	Temperature control in Isothermal cavity
Booster fan	Rated Power: 14 W	Cooling of isothermal cavity
Circulating fan	Rated Power: 20 W	Air circulation in the isothermal cavity
Electric Heater	Equipped with a fan. Power rating: 830 W	Heating of isothermal cavity
CSZ-32 thermal chamber	1 chamber, -73 °C to 190 °C, Accuracy of ± 0.1 °C.	Soil drying for preliminary soil density analysis

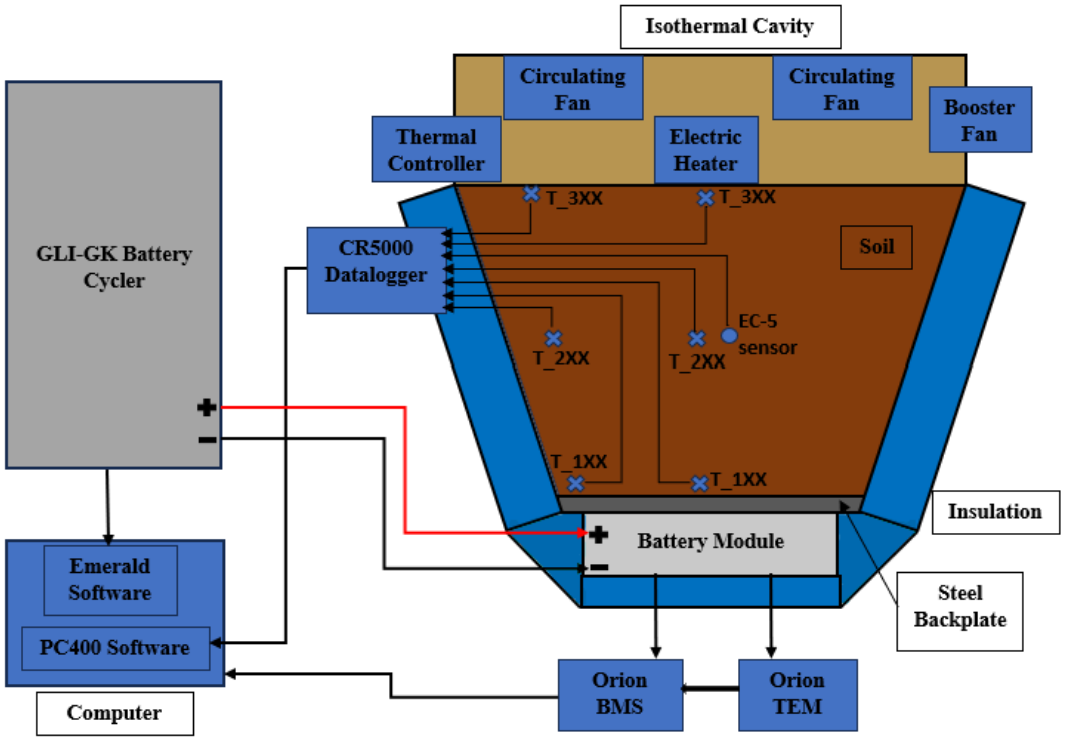

Figure 12: Diagram of test unit hook-up

3.5 Test Procedures

The test procedures for the experimental validation of the model may be grouped in two stages; initial validation tests on the soil and the battery to verify the information in the specification sheet, and the post-validation tests focused on battery operations adapted to residential energy use profiles.

3.5.1 Initial Validation Testing

The initial validation tests involved soil density analysis and moisture content validation, and thermal conductivity test on the soil. For the battery, initial internal resistance and open circuit voltage tests were conducted.

3.5.1.1 Soil density analysis and moisture content validation

The measurement of soil density is important for understanding the properties of the soil, and this plays a vital role in experimental research. The soil bulk density, ρ_b is related to the soil compaction, which is an essential element of its thermal properties. It is calculated as the ratio of

mass of dry soil, $M_{s,dry}$ to the total volume of the soil, V_s, before drying [128], written as Equation 18 below.

$$\rho_b = \frac{M_{s,dry}}{V_s} \tag{6}$$

The density analysis was done on the soil sample in a simple procedure using a weight scale and a thermal chamber. Under laboratory conditions, the soil was filled into a plastic container of known volume, V_c and mass, M_c. The mass of the soil-filled container, M_{s+c}, was measured on the scale and recorded. The soil was then placed in the thermal chamber and oven dried. The mass of the oven- dried soil-filled container, $M_{s+c,dry}$ was measured again on the scale and recorded. The isolated mass of dry soil, $M_{s,dry}$ is obtained from the subtraction of the mass of the container from the total mass of the plastic container filled with dried soil. The equations are:

$$V_s = V_c \tag{7}$$

$$M_{s,dry} = M_{c+s,dry} - M_c \tag{8}$$

The soil bulk density was obtained by substituting equation (19) and (20) into the equation (18). The moisture or water content in the soil is also determined from this process, the gravimetric or mass water content (MWC), was calculated first and then used to determine the volumetric water content (VWC). The MWC is simply the ratio of the mass of water, M_w contained in the soil to the mass of the wet soil, $M_{s,wet}$ i.e., the difference in the mass of wet soil and dry soil, divided by the mass of the wet soil.

$$MWC = \frac{M_W}{M_{s,wet}} \tag{9}$$

The mass of the wet soil is calculated using Equation (22) and substituted into Equation (21).

$$M_{s,wet} = M_{c+s,wet} - M_c \tag{10}$$

The mass of water is calculated using Equation (23) and substituted into Equation (21).

$$M_W = M_{s,wet} - M_{s,dry} \tag{11}$$

The soil bulk density and MWC are used to obtain the VWC, using the mathematical expression,

$$VWC = \frac{M_w \, x \, \rho_b}{M_{s,wet} \, x \, \rho_w} = MWC \, x \, \frac{\rho_b}{\rho_w} \tag{12}$$

ρ_w is the density of water,

The soil test results from the density analysis are summarized in Table 11.

Table 11: Soil bulk density and moisture content

PROPERTY	VALUE
Soil bulk density	1823 kgm^{-3}
Gravimetric moisture content	5 %
Volumetric moisture content	10 %

Compared to the values indicated in the datasheet, where the soil bulk density is 1922 kgm^{-3}, and the VWC is 11%, the test results are lower, but approximate to specified values.

Figure 13: Soil density analysis

3.5.1.2 Thermal conductivity test

To validate for thermal conductivity against the specified values, the soil thermal conductivity was determined experimentally using a TEMPOS thermal conductivity meter together with an RK-3 thermal sensor. This test was done by filling up plastic containers with soil and inserting the thermal sensor at three distinct points in the soil. The TEMPOS meter measures and records the thermal conductivity of the soil. This procedure was done for different packing methods; hand-packed and foot-packed, for dry and non-dry soil in the container.

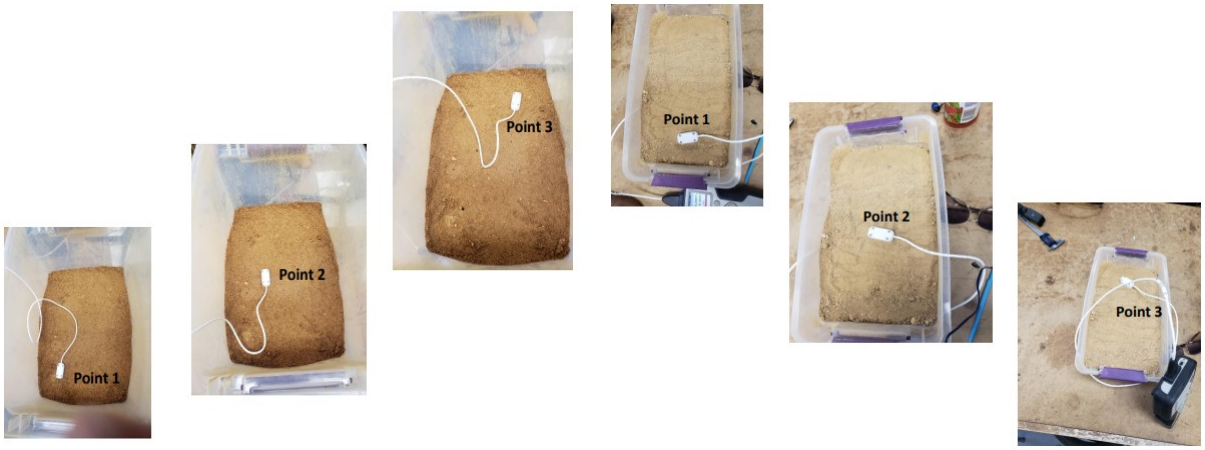

a. Non-dry soil *b. Dry soil*

Figure 14: Soil thermal conductivity Tests

The thermal conductivity measurement from the meter was taken at least ten times for each position of the sensor in the soil, this is necessary due to the frequent occurrence of thermal drifts in the soil, and inconsistencies in the results. Thermal drift occurred when the sensor is not fit tightly in the soil, or there is an air pocket around the sensor in the sample. Soil compaction was done manually, which is not an optimal method of compaction, compared to machines like vibrating tampers, vibrating plate compactors, rammers etc. The sensor probe was inserted manually for this test. The combined effect of using manual methods for soil compaction and insertion of the sensor, leads to undesired air pockets created in the sample and causing a thermal drift. In the occurrence of a thermal drift, the meter displays an error reading, and the test is repeated. The manual processes of this test required that the test be repeated many times and the measured output values be averaged. The results are summarized in Table 12.

Table 12: Thermal conductivity results

	Dry soil	**10% VWC, hand-packed**	**10% VWC, foot-packed**
Average thermal conductivity ($W.m^{-1}K^{-1}$)	0.25	0.79	1.9
Standard deviation	0.0007	0.14	0.09

The thermal conductivity of dry soil saw no change with different packing method and produced poor thermal conductivity for this experiment. This is appropriated to high friction between the

soil particles due to lack of moisture, consequently leading to poor compaction in the soil. The test results for soil containing 10% VWC showed a clear influence of the packing method on the soil thermal conductivity, which is related to the compaction of soil particles. The higher the compaction of soil particles, the higher the thermal conductivity. Based on these results, the soil for this experiment was foot packed.

3.5.1.3 Battery Open Circuit Voltage and Internal Resistance test

A Fluke BT-510 battery analyser was used for initial open circuit voltage (OCV) and internal resistance (IR) measurements to determine the battery's initial state of charge and internal resistance. This process also allows checking for wiring mistakes or imbalance among the cell groups in the module. The feasibility of this research relies on the workings of an unimpaired battery; hence it is necessary to verify adequate performance characteristics and consistency among the cell groups. The results are presented in Figure 15.

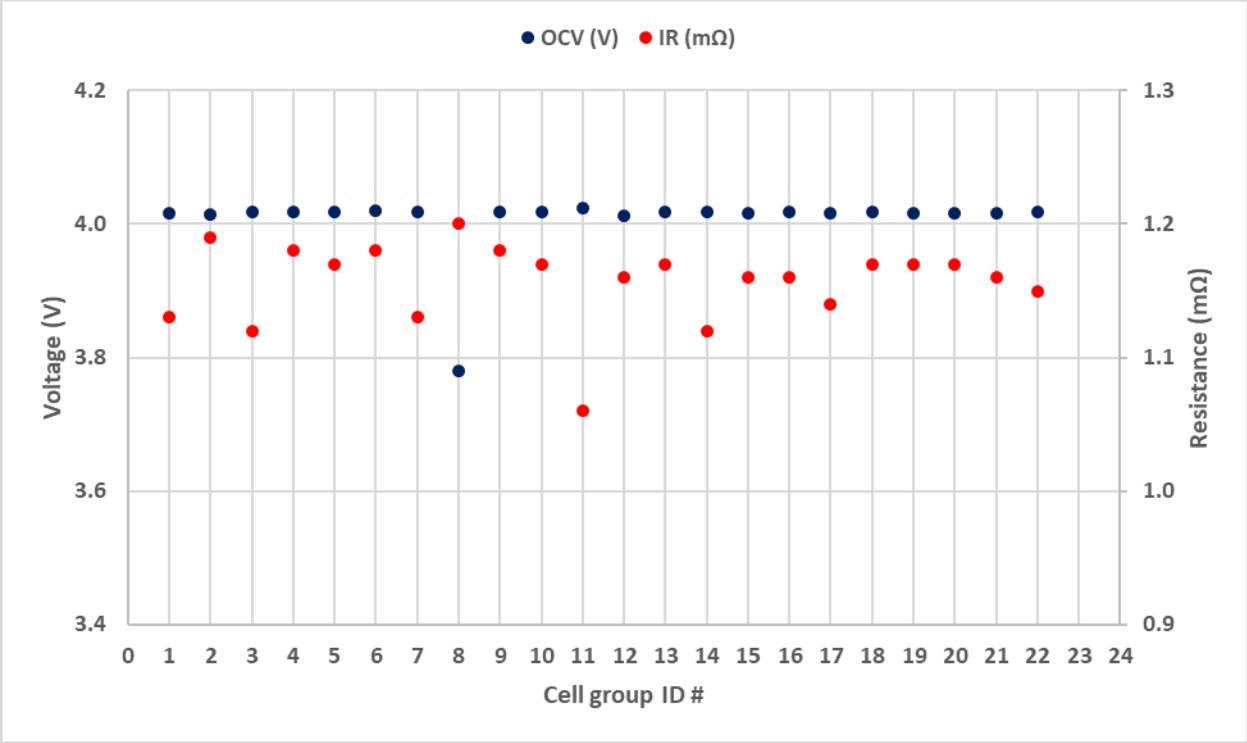

Figure 15: OCV and IR results for individual cell groups in the battery

In the circumstance of an imbalance, as shown in Figure 15, the battery is charged in constant-current-constant-voltage (CCCV) mode, until the cell group voltages are balanced by the BMS to within a maximum voltage difference of 5 mV. At this point, the cell groups are well balanced.

To verify the IR of the battery, each cell group resistance is calculated based on the battery configuration of 24P22S. Each cell is rated to have an internal resistance of $\geq$ 30 mΩ, therefore the total resistance of a cell group containing twenty-four cells in parallel is $\geq$ 1.25 mΩ. The IR tests show that the battery is within the specification of the internal resistance.

3.5.2 Post-Validation Testing

After the initial tests are performed on the soil and battery to certify necessary conditions for battery operations, the post validation tests begin. The results of these tests are analyzed and compared to the model results for validation of the model. The test procedures are developed to mimic residential energy consumption. The tests performed on the battery includes reference performance tests (RPT), and degradation tests for aggressive and non-aggressive battery cycling, and solar test use profiles. The factors considered in the tests are the hour-rate, temperatures, and time.

3.5.2.1 Reference Performance Test (RPT)

The battery degradation cycling is done within a bound state of charge (SOC), therefore those tests provide no information about the battery's usable capacity and efficiency. This information is provided by reference cycling of the battery over the full SOC range to compare the performance to that given in the specification sheet. This is done at intervals in between degradation testing. This is necessary for obtaining performance and degradation metrics such as discharge amp-hour capacity, discharge energy, and energy efficiency. The RPT protocol includes a constant-voltage (CV) charge step, which provides balancing between the cell groups to within a tolerance with a maximum voltage difference of 5 mV. Reference cycling is done in both constant-current (CC) mode and a constant-current-constant-voltage (CCCV) mode. Three cycles are completed in this procedure. In the first cycle, the battery responds to the preceding test done on the battery, the second cycle is done for thermal acclimation of the battery to the current test procedure, after which the third cycle ensures consistency and therefore the result is utilized to draw conclusions on the battery's present status. A discharge step is done after the three cycles to return the battery

to an SOC before the next test is initiated. The test protocol is given in Table 13 and the signal is shown in Figure 16. The negative values represent discharge mode and positive values represent charge.

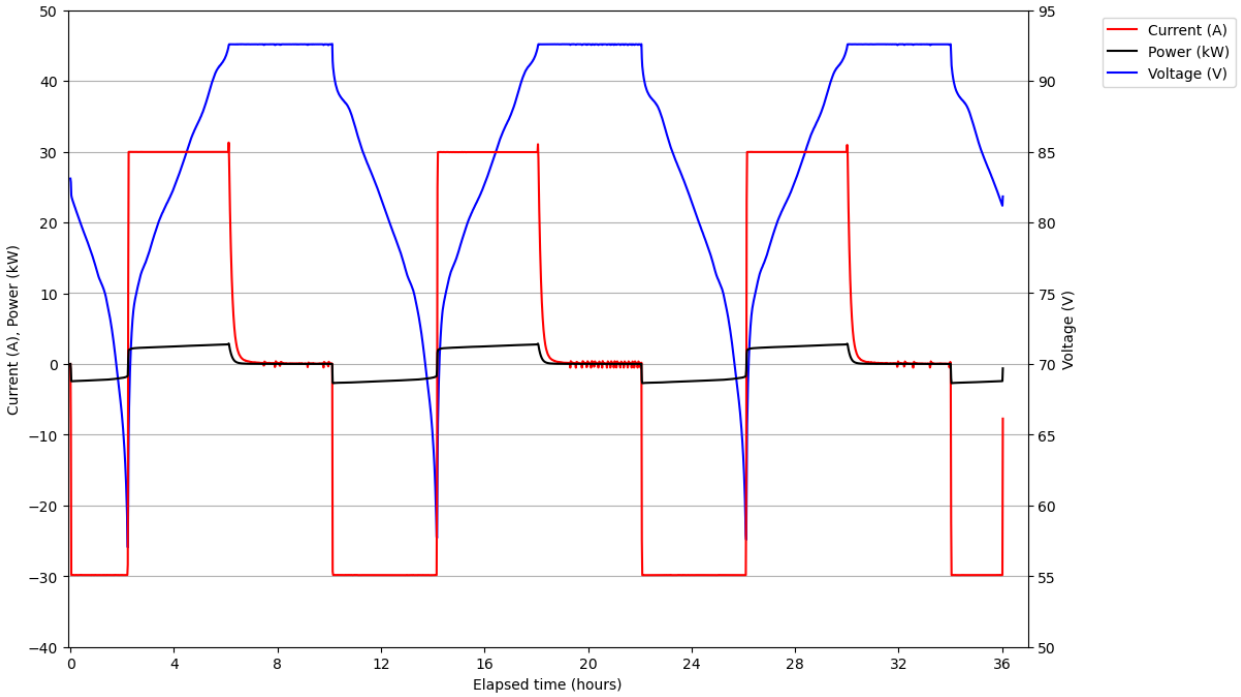

Figure 16: Reference performance test signal

Table 13: Reference performance test procedure

STEP #	STEP TYPE	HOUR RATE	STEP END CONDITIONS
1	Rest	N/A	Maximum measured temp < 55 °C **AND** Step time > 36 s
2	CC Discharge	4 (30 A)	Minimum cell voltage <= 2.5 V
3	Rest	N/A	Maximum measured temp < 55 °C **AND** Step time > 36 s
4	CC Charge	4	Module voltage of 92.4 V (avg 4.2 VPC)
5	CV Charge	4 or less. Module held at 92.4 V (avg 4.2 VPC)	Step time >= 4 h
6	Rest	N/A	Maximum measured temp < 55 °C **AND** Step time > 36 s
7	Loop	N/A	Go back to step 2 (3 cycles total)
8	CC Discharge	4	Step time >= 2 h

3.5.2.2 Solar Test

This test procedure was created for residential solar photovoltaic energy storage application, where energy is stored during solar production in the midday and the battery is discharged in the evenings. The test is designed to avoid solar energy exports during peak production (midday) and peak load in the evenings. This is represented by a CC charge from the hours of 10:00 to 14:00, and a CC discharge from 18:00 to 22:00, with rest periods in between. The signal is designed to operate within a small voltage range, delivering an amp-hour throughput of 68 Ah. This is equivalent to 0.57 full cycles equivalent for every twenty-four hours, which is a light duty signal. The battery is charged and discharged at a 6.5-hour rate, leading to small heat generation from the battery. The battery is first charged up to an 80% SOC before initiation of the 24-hour solar test signal profile. The signal is shown in Figure 17. The negative values represent discharge mode and positive values represent charge. The summary of this test procedure is presented in Table 14.

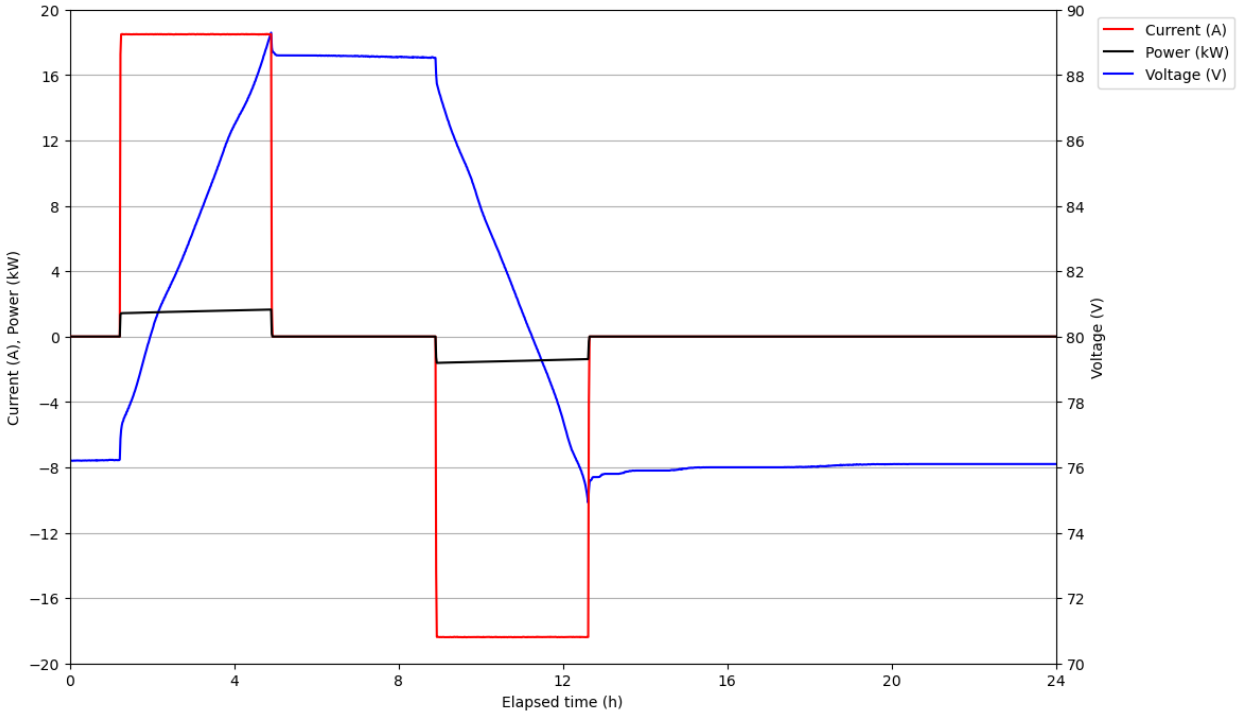

Figure 17: Twenty-four hours solar test signal

Table 14: Solar test procedure

STEP #	STEP TYPE	HOUR RATE	STEP END CONDITIONS
1	Rest	N/A	Maximum measured temp < 55 °C **AND** Step time > 36 s
2	CC Charge	4 (30 A)	Module voltage of 89.32 (avg 4.06 VPC)
3	CV Charge	4 or less. Module held at 89.32 V (avg 4.06 VPC)	Module current < 1.2 A (0.055 APC)
4	Rest	N/A	Maximum measured temp < 55 °C **AND** Step time > 4 h
5	CC Discharge	6.5 (18.5 A)	Step time > 4 h
6	Rest	N/A	Maximum measured temp < 55 °C **AND** Step time > 12 h
7	CC Charge	6.5 (18.5 A)	Step time > 4 h

The battery is charged up to 80% SOC from its initial state before the signal is applied.

3.5.2.3 Non-Aggressive Test

The non-aggressive test procedure was created to cycle the battery in a non-aggressive manner. The test adopts an electrical current signal that varies over a period of twenty-four hours. The signal is a low-power, low-energy signal likened to a light duty load smoothing application that is projected to produce low heat from the battery. The peak discharge current in the signal is 24 A, which is equivalent to a five-hour rate, and the peak charge current is 18 A. The total amp-hour throughput in the signal is 208.5 Ah, inclusive of charge and discharge amp-hours. This is equivalent to 0.9 full cycle equivalent for every twenty-four hours. The signal is intended to start and end at a 50% SOC position for the battery and maintains a SOC band of 40% to 80% SOC for the twenty-four hours. The signal is shown in Figure 18 and Table 15 below outlines the test procedure for non-aggressive battery cycling. The negative values represent discharge mode and positive values represent charge.

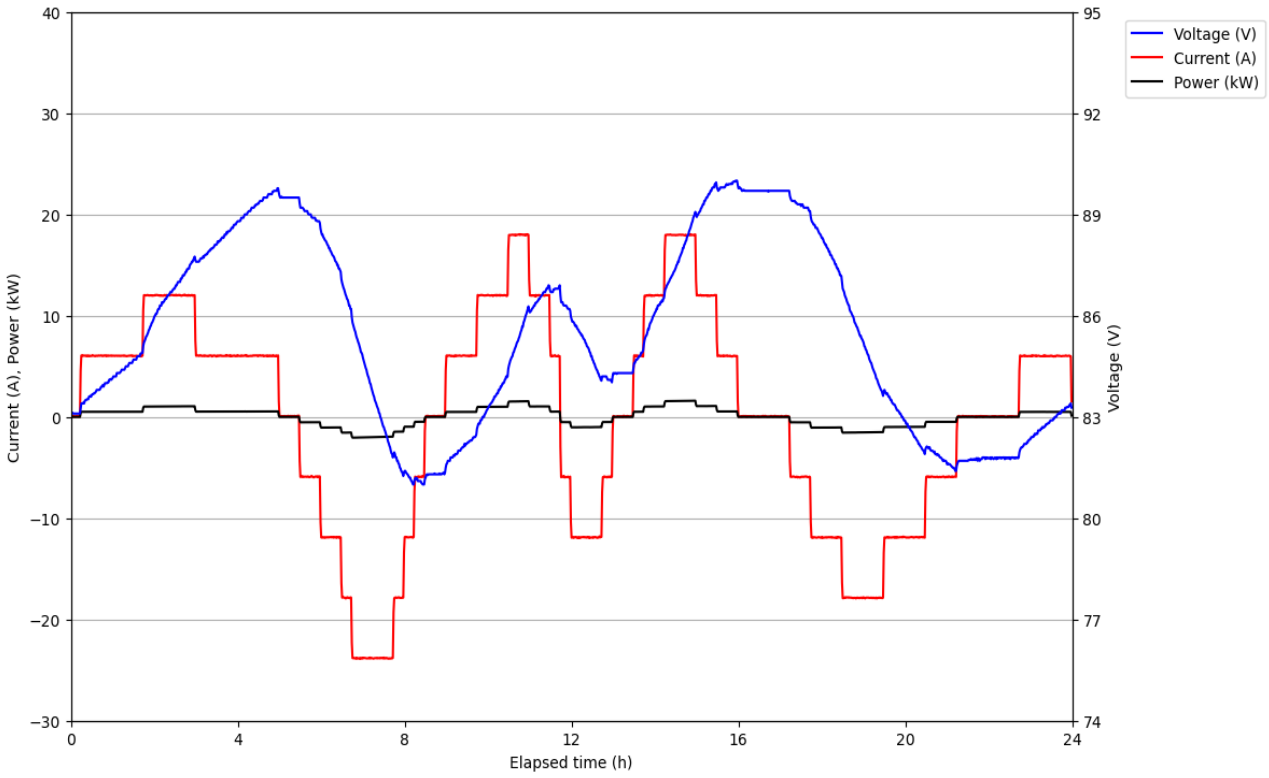

Figure 18: Non-aggressive test signal

Table 15: Non-aggressive test procedure

STEP #	STEP TYPE	HOUR RATE	STEP END CONDITIONS
1	Rest	N/A	Maximum measured temp < 55 °C **AND** Step time > 36 s
2	CC Charge	4 (30 A)	Module voltage of 89.32 (avg 4.06 VPC)
3	CV Charge	4 or less. Module held at 89.32 V (avg 4.06 VPC)	Module current < 1.2 A (0.055 APC)
4	Rest	N/A	Maximum measured temp < 55 °C **AND** Step time > 36 s
5	CC Discharge	4	Discharge 36 Ah to get to 50% SOC
6	Current Signal	6.67 or less	24 h non-aggressive signal
7	Rest	N/A	Maximum measured temp < 55 °C **AND** Step time > 36 s

The battery is charged to 80% SOC from its initial state, and afterwards, repositioned to 50% SOC before the signal is applied.

3.5.2.4 Aggressive Test

The aggressive test on the battery adopts a more aggressive electrical current signal than the non-aggressive signal, varying over the same time. The signal is a high-power, high-energy signal that represents a peak shaving application, and is projected to produce significant heat from the battery, which leads to low efficiency. The peak discharge current in the signal is 130.9 A, which is equivalent to a 55-minute discharge, and the peak charge current is 49 A (2.5 h or 0.4 C). The total amp-hour throughput in the signal is 867 Ah, inclusive of charge and discharge amp-hours. This is equivalent to 3.5 full cycle equivalent (four times that of the non-aggressive signal) for every

twenty-four hours. Continuous battery operation which adopts this signal will lead to greater wear on the battery compared to the non-aggressive or solar test signal. The signal is intended to start and end at an 80% SOC position for the battery and maintains a SOC band of 10% to 80% SOC for the twenty-four hours. Table 16 outlines the test procedure for non-aggressive battery cycling. Figure 19 below shows the 24-hr aggressive test signal. The negative values represent discharge mode and positive values represent charge.

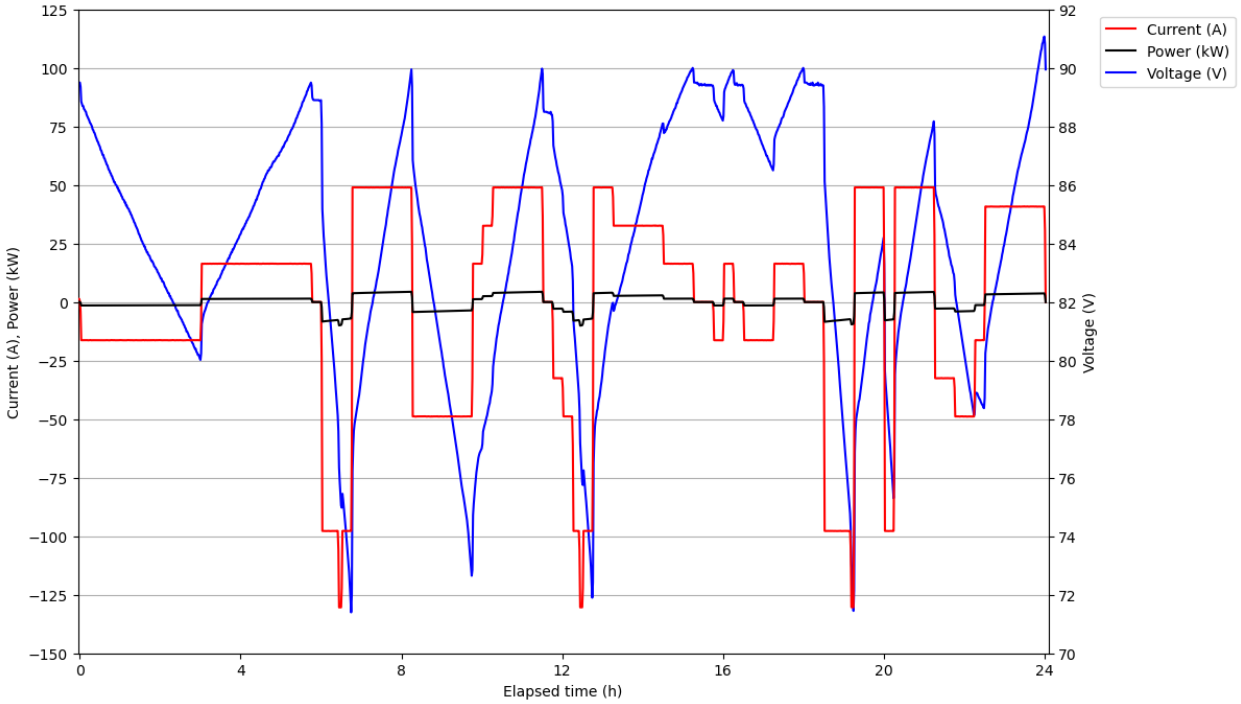

Figure 19: Aggressive test signal

Table 16: Aggressive test procedure

STEP #	**STEP TYPE**	**HOUR RATE**	**STEP END CONDITIONS**
1	Rest	N/A	Maximum measured temp < 55 °C **AND** Step time > 36 s
2	CC Charge	4 (30 A)	Module Voltage of 89.32 (avg 4.06 VPC)
3	CV Charge	4 or less. Module held at 89.32 V (avg 4.06 VPC)	Module current < 1.2 A (0.055 APC)
4	Rest	N/A	Maximum measured temp < 55 °C **AND** Step time > 36 s
6	Current Signal	0.88 or less (Maximum 130 A)	24 h aggressive Signal
8	Rest	N/A	Maximum measured temp < 55 °C **AND** Step time > 36 s

The battery is charged up to 80% SOC from its initial state before the signal is applied.

A summary of the battery application signals is presented in Table 17 and Figure 20 for comparison.

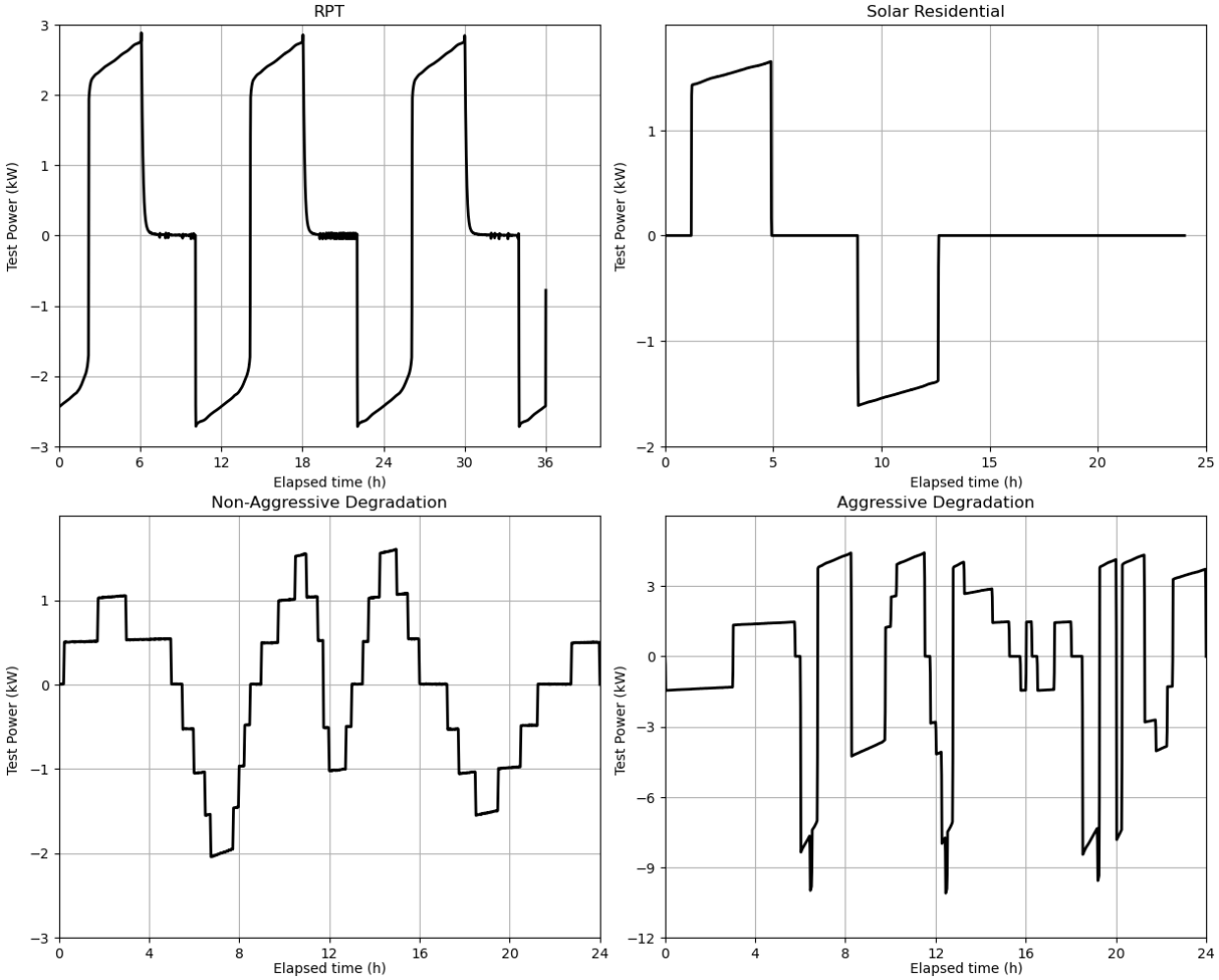

Figure 20: Battery test power signals

Table 17: A comparison of the battery application signals

SIGNAL	**PEAK CHARGE CURRENT (A)**	**PEAK DISCHARGE CURRENT (A)**	**DISCHARGE AMP-HOUR THROUGHPUT (Ah)**	**SOC BAND (%)**
Reference Performance	30	30	120	0-100
Solar Test	18.5	18.5	68	25 – 80
Non-Aggressive	18	24	104.25	40 – 80
Aggressive	49.1	130.9	433.5	10-80

Chapter 4: Modelling Methodology

This chapter discusses the modelling methodology providing a description of the model with identified parameters and the model development processes.

4.1 Model Description

A passive battery thermal management strategy, comprised of a steel plate and the soil surrounding the battery as the heat transport media, is adopted for thermal management in this work, and it is targeted towards residential stationary applications. The thermal model describes the heat flow into the soil. It does not describe the heat distribution within the battery. The battery module is the sole source of heat generation, and it is modelled as a homogeneous heat source (i.e., uniform internal heat generation). The heat flow and temperature distribution from a hexagonal battery pack is illustrated in Figure 22. The heat flow and temperature distribution from all sides of the battery are identical due to the symmetry of the hexagonal shape. Therefore, it is sufficient to model and evaluate only one side of the pack. The geometry of the model represents one-sixth of a full pack buried in the ground. The soil is the heat dissipation medium in this model hence the geometry of the surrounding soil is uniquely a trapezoidal prism to account for heat transfer along the radii of an arc. The heat from the battery flows to the steel plate which then transfers that heat to the surrounding soil. The heat flow diagram is illustrated in Figure 21. The model assumes that the soil is contained of a homogenous material with uniform thermal properties all through. This is a logical assumption because the soil surrounding the battery can be methodically compacted during the installation. The temperature distribution through the soil is predicted, and the time constant for heat transfer and steady state conditions is investigated. The mode of heat transfer considered in this model is conduction.

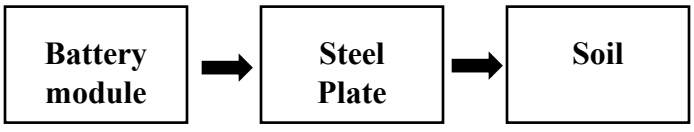

Figure 21: Heat flow for passive BTM

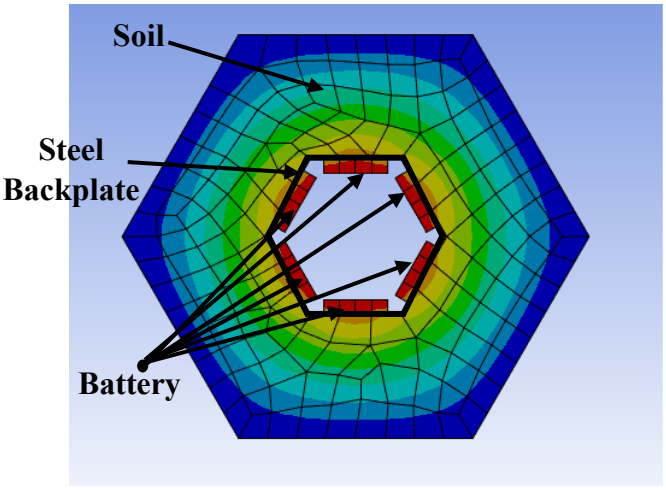

a: Temperature distribution of full battery pack

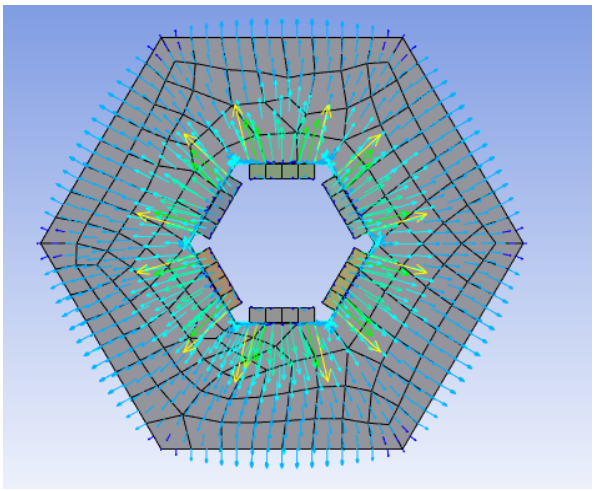

b: Direction of heat flow from full battery pack

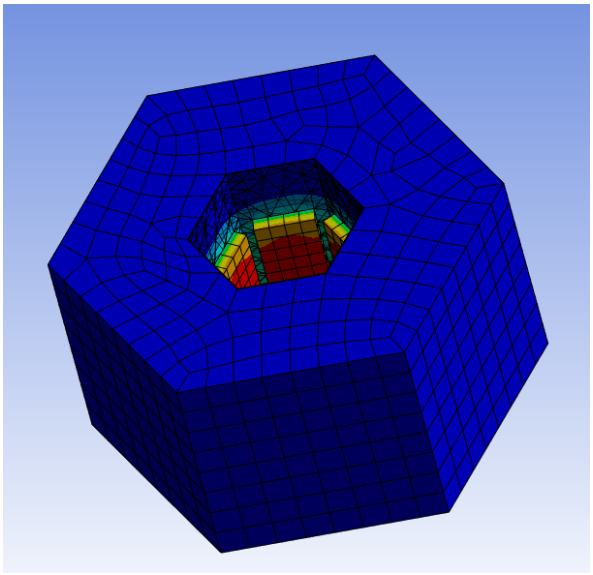

c: 3D model of full pack showing isothermal back planes sides

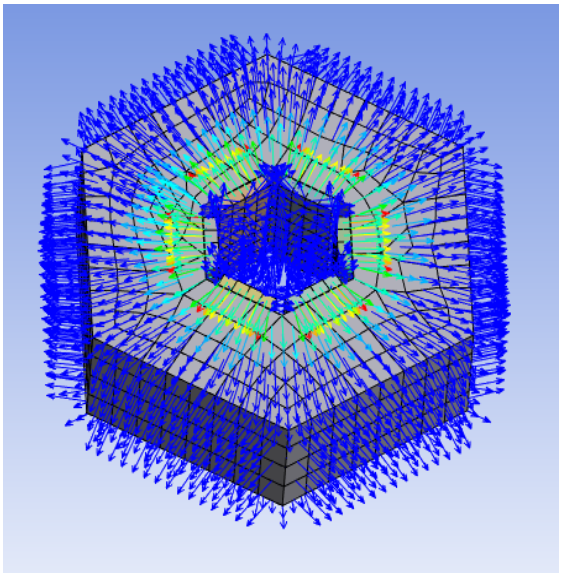

d: cross-section of 3D model showing heat flowing through isothermal back planes alone

Figure 22: Full hexagonal battery pack

4.2 Model Parameters

The model parameters are identified using input and output variables only. The parameter identification is necessary to determine parameters to be substituted for, in the thermal model based on the input and output variables. The input parameters for the model are listed below. The selected values of the model parameters are real representative values of the thermal properties of the model

parts obtained through measurements or documentation, as well as the test signals. Values for each are given in Table 18.

- Thermal conductivities of the materials, λ
- Specific heat capacity of the materials, C_p
- Density of the materials, ρ
- Volumetric heat generation in the battery, $\ddot{Q}$
- Initial temperature, T_o
- Adiabatic conditions
- Isothermal soil temperature at the back of the geometry, T_{iso}
- Simulation time, t

For accuracy of results, whilst also enhancing the processing time, the time step of the simulation is determined by the duration and smallest step time of the test signal. For transient thermal analysis, the time step sizes may be large i.e., minutes or hours, if necessary, based on the duration of the simulation. However, the events that take place under short periods must be captured too. The shortest time for any step in the signals is five minutes, a 1-minute time step is sufficient for capturing all the steps in the battery test signals. For consistency, a uniform time step is chosen for all test signals.

4.2.1 Model of the Battery Module

As a function of the battery module being modeled as a single homogenous entity composed of the cells, cell holder, and thermal pad, an average value is determined for the thermal properties. This is achieved using the volume fraction of each individual material in the module.

The average thermal conductivity for the battery module is calculated using the equation 4,

$$\lambda_{avg} = \sum_{i} (\phi_i \cdot \lambda_i) \tag{13}$$

where ϕ_i is the volume fraction of individual materials, i and λ_i is the corresponding thermal conductivity.

Similarly, an average specific heat capacity of the battery module is calculated using Equation 5,

$$MC_{p,avg} = \sum_{i} (m_i . c_{p,i}) \quad (14)$$

where M is the mass of the module, $C_{p,\,avg}$ is the average specific heat capacity of the module. M_i, $c_{p,i}$ are the individual mass and specific heat capacity of the material components, i, in the module. The output parameters of the model are the temperature distribution within the soil in a set time. The temperature change within the soil provides information on the heating and cooling time as well as the magnitude.

Table 18: Model input parameters

Input Parameters	**Symbol**	**Value**	**Unit**
Thermal conductivity of battery module	λ_b	4.82	$Wm^{-1}K^{-1}$
Thermal conductivity of steel plate	λ_p	18	$Wm^{-1}K^{-1}$
Thermal conductivity of soil	λ_s	1.9	$Wm^{-1}K^{-1}$
Density of battery	ρ_b	1163	kgm^{-3}
Density of steel plate	ρ_p	7800	kgm^{-3}
Density of soil	ρ_s	1823	kgm^{-3}
Specific heat capacity of battery	$C_{p,b}$	1.031	$Jg^{-1}K^{-1}$
Specific heat capacity of steel plate	$C_{p,p}$	0.460	$Jg^{-1}K^{-1}$
Specific heat capacity of soil	$C_{p,s}$	1.000	$Jg^{-1}K^{-1}$
Isothermal surface temperatures	T	30	^oC
Uniform Initial temperatures (battery, backplate and soil)	T_i	30	^oC
Heat flux	$\dot{Q}$	0	Wm^{-2}
Simulation time	t	Heat signal time	s
Time step	t	60	s

4.3 Model Heat Generation Rate Prediction

The heat generation rate in the battery can be described with Equation 2 (section 2.4). The heat dissipated through the surrounding environment (i.e. soil) is determined using the energy loss for a single cycle. This energy is recognized as the irreversible heat generated in the battery, and therefore is the adopted heat signal for this model. This can be appropriated to heat generation as a function of the resistance in the battery. The reversible heating is ignored here, so the equation is simplified into;

$$Q = I^2R \tag{15}$$

The internal resistance of a battery is influenced by temperature and state of charge (SOC). The variation of internal resistance decreases with increase in temperatures, and internal resistance are higher or lower temperatures below 10 ºC. Above 10 ºC, the influence of temperature on the internal resistance becomes less significant [129], [130]. The influence of SOC on the internal resistance of a battery is prominent at low SOC (0-10%) and high SOC (above 90%). Between 10% and 90% SOC, the variation of the battery's internal resistance is negligible and thus the internal resistance is considered to be constant [131], [132]. The operating temperature range for this model is above 30 ºC, and the battery is cycled between an SOC range from 10% to 80%. Therefore, the drastic changes in the internal resistance of the battery are avoided and the effective battery resistance is taken as a constant and is obtained from experimental results. As a function of cycling between a bound state of charge, reversible heating is not accounted for. Although reversible heating is significant at low C-rates, more than 80% of the reversible heat is generated at low states of charge between 0-10% SOC, which is avoided [16].

To determine the effective battery resistance, The total heat loss (i.e., the difference between the charge energy, C.E and discharge energy, D.E), is determined from experimental battery testing for a distinct duty cycle and is divided by time to complete the cycle to obtain an average heat generation rate (W).

$$Q_{avg} = \frac{C.E - D.E}{t} \tag{16}$$

The rate of heat generated is divided by the summation of the squared current signal adopted for the cycle to determine a constant effective battery resistance using Equation 6.

The varying heat generation rate, $Q_{(t)}$ i.e., heat generated at any time, t during the battery operation is calculated from the total heat generated divided by the time interval, ∂t.

$$Q_{(t)} = \frac{I_{(t)}{}^2 . R . t}{\partial t} \tag{17}$$

The varying heat generation rate is converted to a volumetric quantity, dividing by the volume of the battery module, V_b to obtain the internal heat generation, $\ddot{Q}$ which is inputted into the model.

$$\ddot{Q} = \frac{Q_{(t)}}{V_b} \tag{18}$$

4.4 Model Development

The thermal model was built with ANSYS mechanical software. The battery module is represented as a rectangular block, with uniform internal generation. The geometry represents a module built according to industry standards, containing cylindrical cells of 0.07 m in height, and stacked into a block of material designed to hold individual cells and keep the cells spaced apart. The dimensions of the module are given as width of 0.38 m, height of 1.02 m, and a thickness of 0.09 m. The steel back plate is designed as a thin rectangular plate with dimensions of height, 1.5 m, width 0.55 m and a thickness of 0.005 m. The soil medium is represented using a trapezoidal prism, of height, 1.5 m. The parts were created and assembled in Solidworks, and the geometry was imported into Ansys. The input parameters including thermal properties (i.e., thermal conductivity, specific heat capacity, and density) are defined in the ANSYS software. This work uses an adaptive method of meshing based on the geometry. For this model, medium hexahedral mesh elements are chosen over tetrahedral due to the simplicity of the geometry and the absence of curvature. This ensures reasonable contact between elements and accuracy with less computation time than tetrahedral methods. The meshing technique selected generated a total of 11,567 elements and 53,998 nodes (comprised of 14,203 corner nodes and 39,795 mid nodes). The average skewness was 0.16 with a maximum skewness of 0.79, which is below the 0.89 limit of accuracy for hexahedral mesh elements. The model predicts the temperature distribution at all points in the soil, however, for model validation, soil temperatures are measured at twelve positions, defined using coordinate systems, and compared to experimental data.

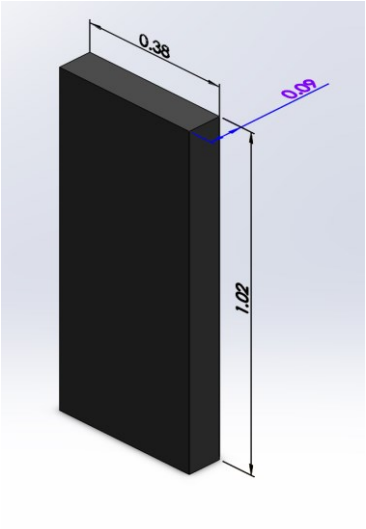

a: Battery model

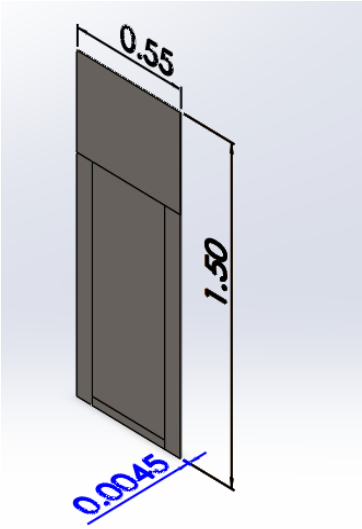

b: Steel back plate model

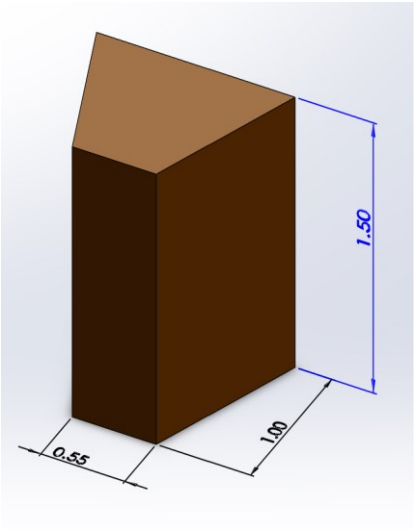

c: Soil model

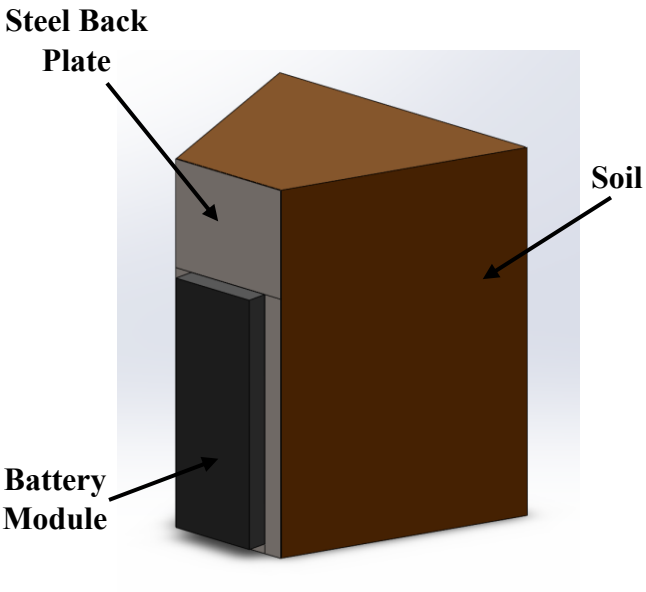

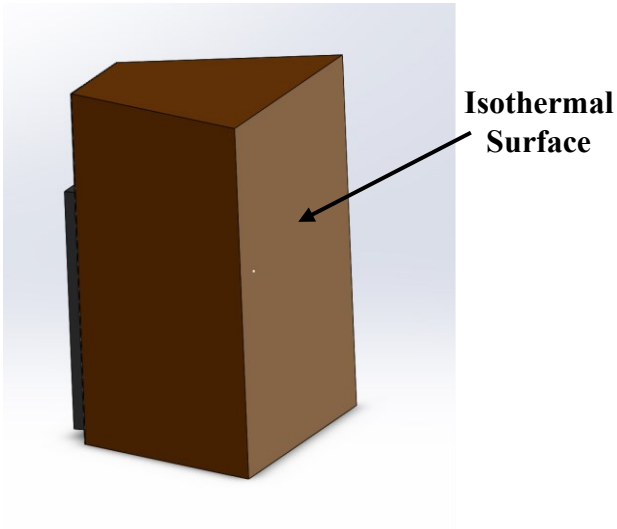

d: Coupled battery-backplate-soil model

Figure 23: Battery model parts with dimensions (in meters)

4.5 Initial and Boundary Conditions

Initial Conditions

Where the battery is not being operated, thermal acclimation occurs, and the temperatures are uniform across all the material parts. Because the soil is an infinite medium, the constant ambient soil temperature becomes the initial temperature of the whole system (i.e., the battery and the immediate surrounding soil). The system temperature at the initial state, $T_{(t=0)} = T_{amb}$.

Boundary Conditions

The boundary conditions for the model determine the heat transfer in the medium. To avoid earth heating of the battery as well as surface climatic heating or cooling from the top, the direction of heat flow is controlled to only radial direction in the model. All sides of the geometry (including the top and bottom) are adiabatic to evaluate the radial heat flow, hence heat flux is set to zero except for the rear face of the geometric structure representing the soil further away from the battery in the horizontal direction. As a function of little variation of soil temperatures with increasing depth in the soil [76], this is represented by maintaining a constant temperature at the isothermal surface of the soil geometry part.

4.6 Governing Equations

Considering the law of conservation of energy, the internal energy of the whole system may be described by Equation 10.

$$Q_{in} - Q_{out} + Q_{gen} = Q_{st} \tag{19}$$

The heat input, Q_{in} is zero for this module. The rate of heat flow out, Q_{out} is the radial heat conduction rate from the battery to the soil, which can be determined using the conduction shape factor, (CSF) by Equation 11.

$$Q_{out} = S.\lambda.\Delta T \tag{20}$$

where λ is the thermal conductivity, ΔT is the temperature difference between the inner and outer boundaries, and S is the conduction shape factor. The CSF is defined as the ratio of the heat transfer area, A to the heat transfer length, L. A simple model is developed in [133] to determine the shape factor of hollow cylinders, whose inner or outer cross-sections may be an n-sided polygon. The model uses an averaging technique due to the changing area of heat transfer from the inner

boundary to the outer boundary of the geometry. Thus, an average heat transfer area is defined by the equation 12.

$$A = \left(\frac{1}{n_o}\right)\left(\sqrt{A_i A_o}\right) + \left(1 - \frac{1}{n_o}\right)\left(\frac{A_o - A_i}{\ln\left(\frac{A_o}{A_i}\right)}\right) \tag{21}$$

where A is the average heat transfer area, n_o is the number of sides of the outer polygon, A_i, A_o are the surface areas of the inner and outer boundaries. The equation 12 can then be substituted in the equation 13 to obtain a shape factor for a fixed heat path length. This is further substituted into equation 11. to determine a one-dimensional heat conduction rate.

$$S = \frac{A}{L} \tag{22}$$

The heat stored in the medium is defined by the equation 14,

$$Q_{st} = \rho C \frac{\partial T}{\partial t} \tag{23}$$

The conservation of energy equation (equation 10) becomes,

$$Q_{gen} - S.\lambda.\Delta T = \rho C \frac{\partial T}{\partial t} \tag{24}$$

where λ is the thermal conductivity, ρ is the soil density, T is temperature, and t is time. Q_{gen} represents the rate of internal heat generation inside the battery module volume. The second term defines the heat conducted, and the last term on the right-hand side describes the energy storage inside the soil.

4.7 Summary

The method used in the model development may be summarized in the following steps.

1) Build and assemble geometry parts in Solidworks,
2) Load ANSYS software and initiate transient thermal simulation,
3) Import assembled parts to ANSYS software and define the material thermal properties (i.e., thermal conductivity, density, and specific heat capacity),
4) Define mesh property and generate mesh,
5) Determine internal heat generation data using Equations (6) – (9),
6) Input internal heat generation to the representative battery block,
7) Set initial conditions: uniform temperature of 30 ^{o}C for the battery, back plate, and soil,

8) Set boundary conditions: isothermal surface of 30 ^{o}C, Heat flux of 0 Wm^{-1} on adiabatic sides of the geometry,
9) Set simulation total time and step time of 60 seconds,
10) Run the simulation and download result,
11) The resulting temperature distribution of the soil is analysed and discussed.

Chapter 5: Results

This chapter presents the results of the developed model predicting the soil thermal behaviour and results from experiments. Distinct soil temperatures and heat power are shown and discussed for different battery signals.

5.1 Experimental Results

The objective of experimentation is to provide a framework for validation of the developed model by comparison. The temperature variation in the soil is examined as the battery is cycled. This section presents the result for the individual test procedures discussed in section 3.5.2.

The experimental results include battery performance results and soil temperature response to the heat generated from the battery. The energy measurements of the battery capacity are logged and downloaded from the energy management system of the power cycler. The soil temperatures are recorded and logged in the CR5000 datalogger, through connected thermocouples. The recorded data contained soil temperatures measured with thermocouples situated at distinct points in the soil. The result files are downloaded as Excel files, and the data was analyzed with Python programming language. The battery energy measurements are recorded at a 15 second time interval and soil temperatures are recorded at 1 second time interval. However, the result files are averaged to one minute for comparison with the model. The soil temperatures plots are labelled in the format "*T_XYZ_C_avg*" to refer to test temperatures measured from the thermocouple locations in the soil. *X* is a numerical value (1,2 or 3), denoting the location from the battery back plate in the soil. "1" indicates soil temperatures nearest to the battery, "2" indicates soil temperatures 0.375 m away from the battery, and "3" indicates soil temperatures 0.75 m away from the battery. *Y* denotes the position relative to the symmetry of the conducting surface area of the battery module. It is represented by a *S* for side, or *C* for center. *Z* denotes the position relative to the height of the battery module. It is represented by a *T* for top height of the battery, or *B* for bottom at half the height of the battery. '*_C_'* indicates that the temperatures are measured in ^{o}C. In summary the naming format is given in the table below.

Table 19: Naming format for recorded soil temperatures

LOCATION	LABEL
Position 1, Center, Top	T_1CT_C_
Position 1, Side, Top	T_1ST_C_
Position 1, Center, Bottom	T_1CB_C_
Position 1, Side, Bottom	T_1SB_C_
Position 2, Center, Top	T_2CT_C_
Position 2, Side, Top	T_2ST_C_
Position 2, Center, Bottom	T_2CB_C_
Position 2, Side, Bottom	T_2SB_C_
Position 3, Center, Top	T_3CT_C_
Position 3, Side, Top	T_3ST_C_
Position 3, Center, Bottom	T_3CB_C_
Position 3, Side, Bottom	T_3SB_C_

5.1.1 Reference Performance Test Results

Figure 24 shows the test power, maximum battery temperature, and soil temperature variations in the soil as heat is generated in the battery and transported through the soil. The result show that less heating occurs at the beginning of discharge, keeping the temperatures almost constant, but towards the end of discharge, significant heating occurs, raising the temperatures substantially. The trend is similar for the constant-current charge. However, in the constant voltage charge, the power output is very low and less heat is generated, hence the module temperature declines significantly. Three cycles are completed following each other with no wait period in between, hence the battery temperatures increase with each cycle due to insufficient time for cooldown. The battery temperature peaks at 47 ºC in the third cycle. Soil temperatures nearest to the battery respond quickly as the heat begins to flow through. At this position, soil temperatures are higher because the cross-sectional area of the heat conduction path is smallest, therefore the 'heat concentration' is highest at this position in the soil. Further away from the battery, the cross-sectional area increases creating more pathways for heat flow thus temperatures are lower at positions 2 and 3, and respond slower. It is also observed that nearer to the battery, the soil

temperatures at the top are lower because there are additional heat pathways above the top due to additional backplate material, which is not the case at the lower height of the battery. The soil temperatures rise at high heat generation rates, and fall as the rate of heat generation reduces. Soil temperatures continues to rise with each cycle, and a steady state is not yet reached.

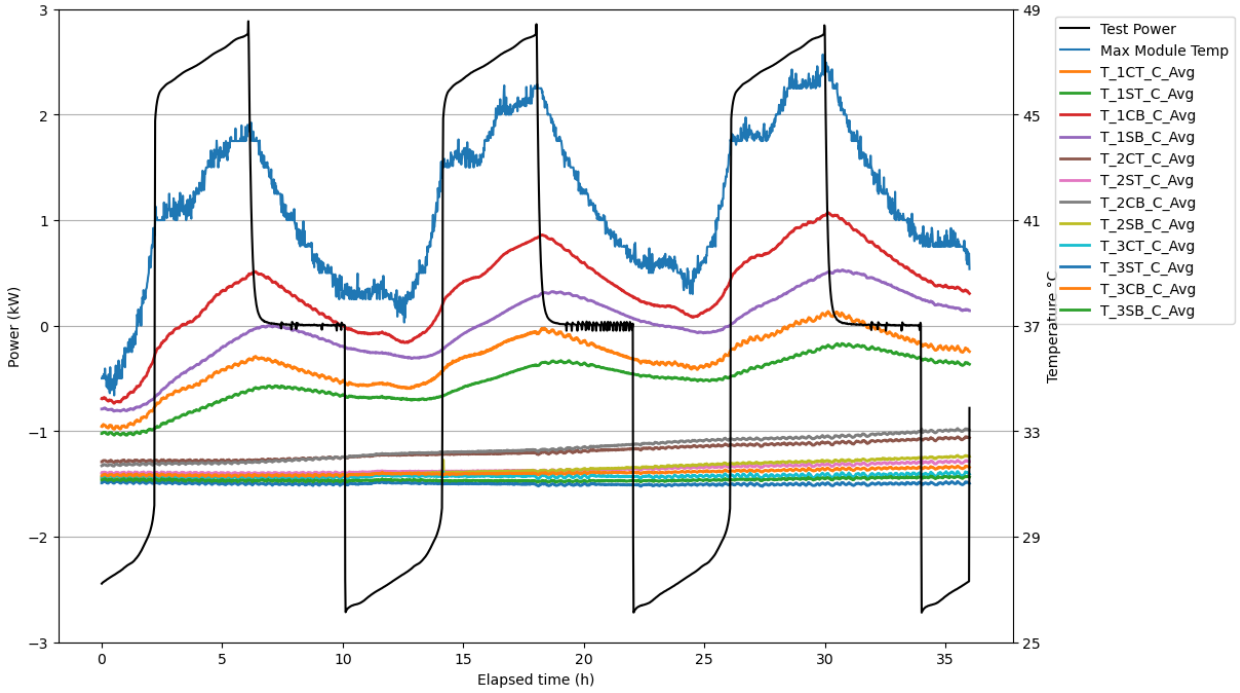

Figure 24: Reference performance test soil temperatures

5.1.2 Solar Test Result

Figure 25 shows test power, maximum battery temperature, and soil temperature response for the solar test described in section 3.5.2.2. The procedure involves very low rate cycling and significant rest periods between charge and discharge modes in the procedure. The battery temperature increases as heat is generated and declines during the rest periods in the signal. The maximum battery temperature peaks at 34.4 ºC and remains below 35 ºC through consecutive cycles. The battery temperature returns to its initial temperature during the rest period before a new cycle begins. The soil temperatures respond to battery heat, rising as heat is generated and cooling as the heat is transported through the soil. Soil temperatures close to the battery only increase by 2 ºC, indicative of low heat generation for this procedure, and cools back to its original temperatures during the extended rest period. Soil temperatures at positions 2 and 3 do not increase notably following four consecutively cycles. This points to sufficient thermal mass of the soil to store the

little heat generated. A steady temperature trend or steady state is observed through each cycle. This means that extended continuous battery cycling for solar test application of this mode can be achieved, and the battery temperature be kept below 40 ºC.

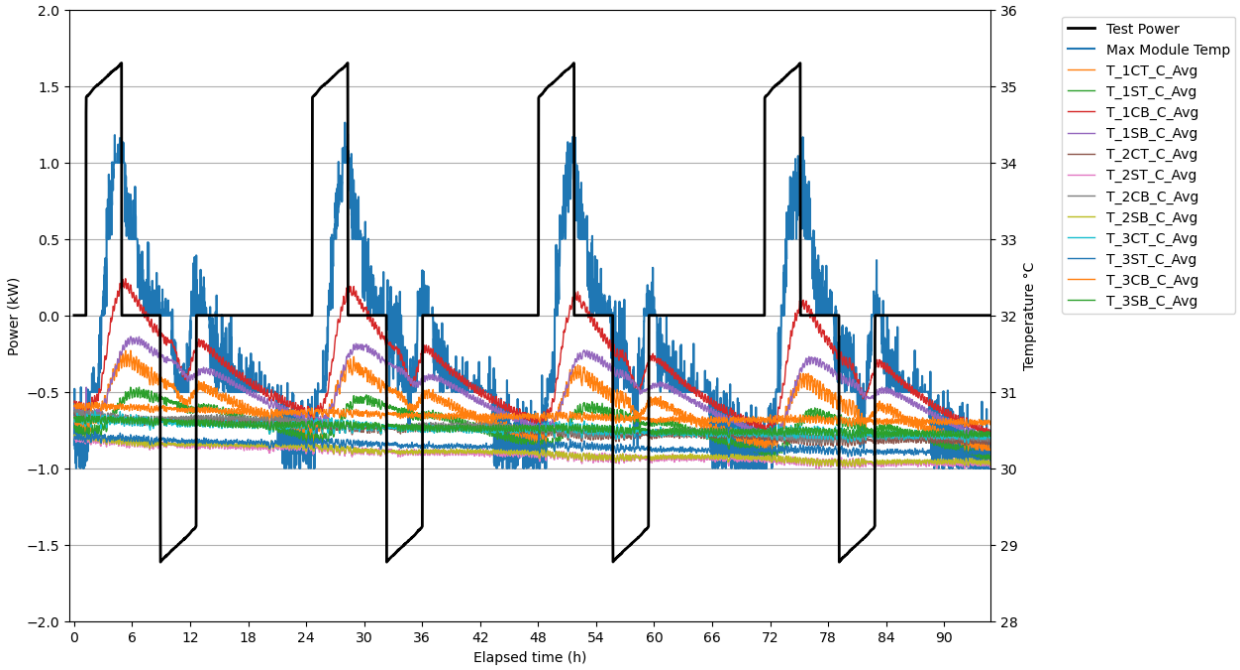

Figure 25: Solar test soil temperatures

5.1.3 Non-Aggressive Test Result

The test begins with a repositioning charge of the battery before the current signal is adopted, therefore the time step for this initial step is shown negative, and the 0 hour corresponds to the start time of the non-aggressive signal. Figure 26 shows the test power, maximum battery temperature, and soil temperatures for five cycle of non-aggressive battery testing. The battery temperature increases as heat is generated and declines during the periods of decreasing heat generation in the signal. The maximum battery temperature peaks at 34.4 ºC during the initial charge step, however the battery temperature only increase by 3 ºC through consecutive cycles. The battery temperature returns to its initial temperature before a new cycle begins. The soil at position 1 respond immediately to heat from the battery, but the temperatures only rise by 2 ºC. Soil temperatures at position 2 and 3 do not show increase through five cycles. Although there are no lengthy rest periods in this signal, the signal is a low power signal, which generates little heat. The soil temperatures are identical with each cycle which suggests a steady state with consecutive

non-aggressive cycling. This means that extended continuous battery cycling for a non-aggressive application such as this can be achieved, and the battery temperature be kept below 40 ºC.

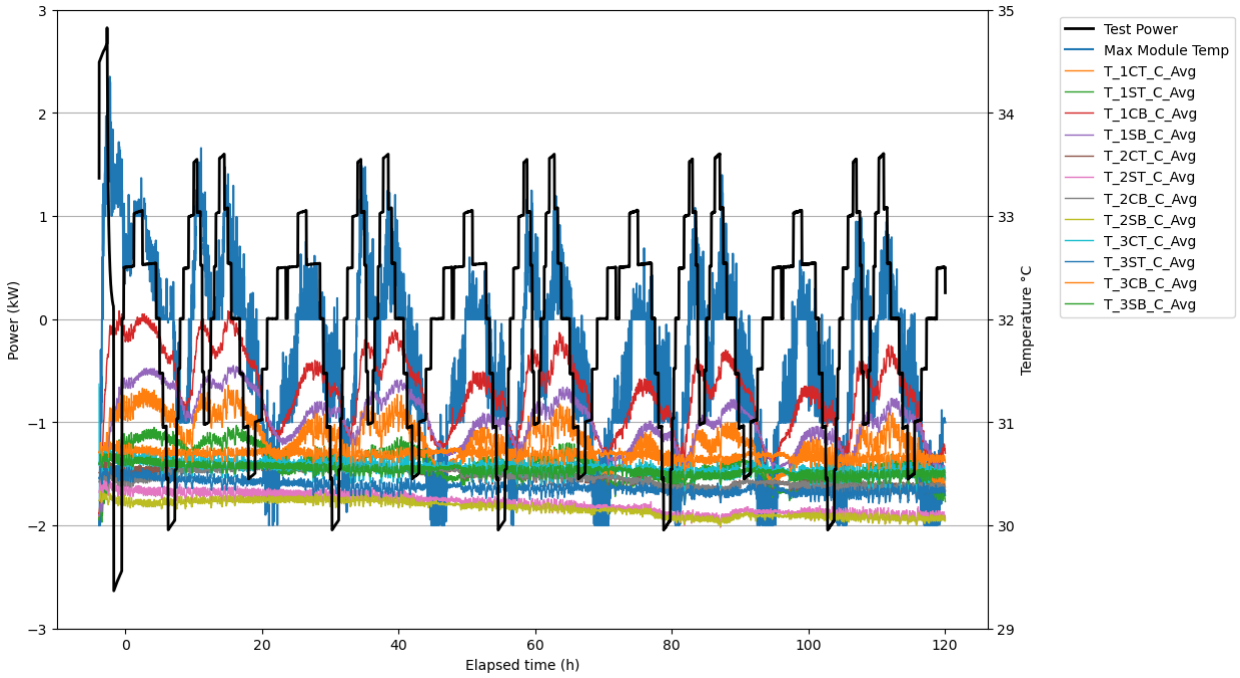

Figure 26: Non-aggressive test soil temperatures

5.1.4 Aggressive Test Result

The test begins with a repositioning charge of the battery before the current signal is adopted, therefore the time step for this initial step is shown negative, and the 0 hour corresponds to the start time of the aggressive signal. Figure 27 shows the test power, maximum battery temperature, and soil temperatures for one cycle of aggressive battery testing. The test signal contains high power outputs at several points, leading to significant heat generation. The battery temperature increases as heat is generated and declines during the periods of decreasing heat generation in the signal. The battery temperature peaks at 58 ºC. Soil at position 1 respond immediately to heat from the battery and have higher temperatures, peaking at 46 ºC. Positions 2 and 3 do not record rising temperatures until much later in the signal as more heat is generated. Soil temperatures at position 2 starts to increase after twelve hours of battery operation. Position 3 stays constant, only responding to the heat with a small temperature increase towards the end of the cycle. This indicates that the soil has insufficient thermal mass and thermal conductivity for the heat generated

in this signal, and substantial time for heat propagation in between aggressive battery cycles is required. Thus, consecutive aggressive cycles may be detrimental to the battery.

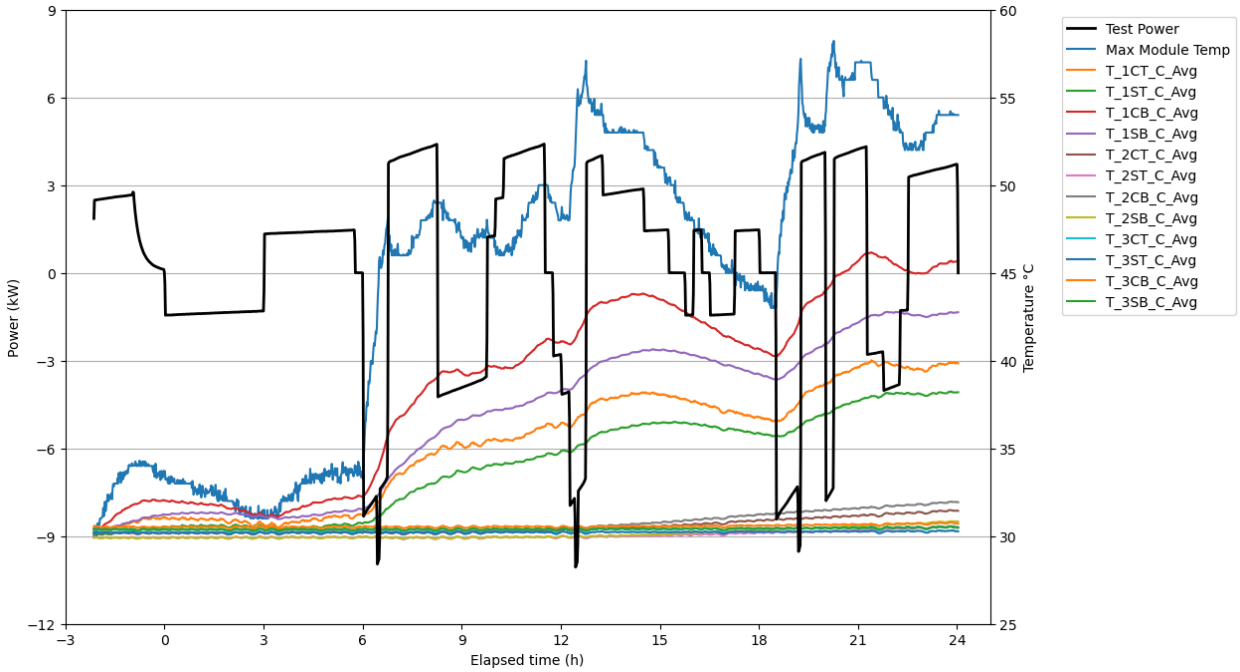

Figure 27: Aggressive test soil temperatures

5.1.5 Summary of Tests Heat Generation

Table 20 presents information used to obtain the heat power rate, which includes the total heat loss for each signal, the total time for a single duty cycle, average heat generation rate, and the maximum heat power generated.

Table 20: Summary of heat loss calculation

SIGNAL	TOTAL HEAT LOSS (kWh)	CYCLE TIME (h)	AVERAGE HEAT RATE (kW)	MAXIMUM HEAT RATE (kW)
RPT	0.43	12	0.035	0.058
Solar test	0.12	24	0.005	0.016
Non-Aggressive	0.12	24	0.005	0.026
Aggressive	1.83	24	0.076	0.67

5.2 Model Results

The model results are presented in this section. The model results are obtained from ANSYS as Excel files and processed with Python programming language. Soil temperatures are recorded at twelve locations, defined by coordinate system, relative to the battery: four positions (each one at the side top (ST), side bottom (SB), center top (CT), and center bottom (CB)) directly behind the battery (position 1), 0.375 m away from the battery (position 2), and 0.75 m away from the battery (position 3). Figure 28 below shows the coordinate positions for the recorded soil temperatures presented in the results. In the developed model, the isothermal soil surface is defined at a distance 1 m away from the battery module, whereas the isothermal cavity of the laboratory test unit is located behind the soil temperature sensors, which are positioned at 0.75 m from the battery module. This is because the soil temperature sensors at position three, 0.75 m away from the battery, are placed in the soil inside the test unit, and the isothermal cavity is built outside the soil enclosure box. Thus, the isothermal is set beyond 0.75 m in the model because at 0.75 m away from the battery, the soil is not isothermal.

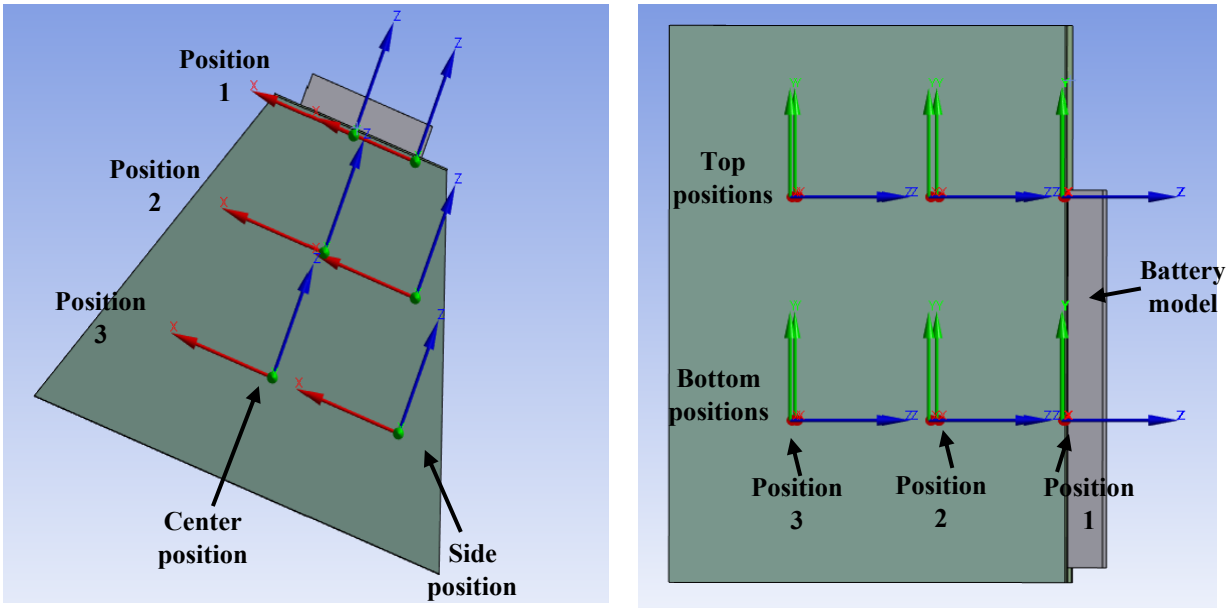

Figure 28: coordinate position of recorded soil temperatures in the model

The model results include information about the battery temperatures and soil temperature response to the heat generated from the battery. The soil temperatures plots are labelled in the format "*M_XYZ_C_*". '*M_*' is to indicate the soil temperatures from the model. *X* is a numerical

value (1,2 or 3), denoting the location from the battery back plate in the soil. “1” indicates soil temperatures nearest to the battery, “2” indicates soil temperatures 0.375 m away from the battery, and “3” indicates soil temperatures 0.75 m away from the battery. *Y* denotes the position relative to the symmetry of the conducting surface area of the battery module. It is represented by a *S* for side, or *C* for center. *Z* denotes the position relative to the height of the battery module. It is represented by a *T* for top height of the battery, or *B* for bottom at half the height of the battery. ‘*_C_’* indicates that the temperatures are measured in ^{o}C. In summary the naming format is given in the table below and is similar to experimental naming format.

Table 21: Naming format for model soil temperatures

LOCATION	**LABEL**
Position 1, Center, Top	M_1CT_C_
Position 1, Side, Top	M_1ST_C_
Position 1, Center, Bottom	M_1CB_C_
Position 1, Side, Bottom	M_1SB_C_
Position 2, Center, Top	M_2CT_C_
Position 2, Side, Top	M_2ST_C_
Position 2, Center, Bottom	M_2CB_C_
Position 2, Side, Bottom	M_2SB_C_
Position 3, Center, Top	M_3CT_C_
Position 3, Side, Top	M_3ST_C_
Position 3, Center, Bottom	M_3CB_C_
Position 3, Side, Bottom	M_3SB_C_

5.2.1 Model Input Heat Power Generation

The internal heat generation input signal of the model that is used to obtain the model results are discussed here. The heat power signals are calculated from the current signals and the loss efficiency obtained from experimental testing results for each signal (see section 5.1.5). The test signals are illustrated in section 3.5.2, and the equations used are discussed in section 4.3. Figure 29 shows the obtained heat power generation rate for each of the battery signals.

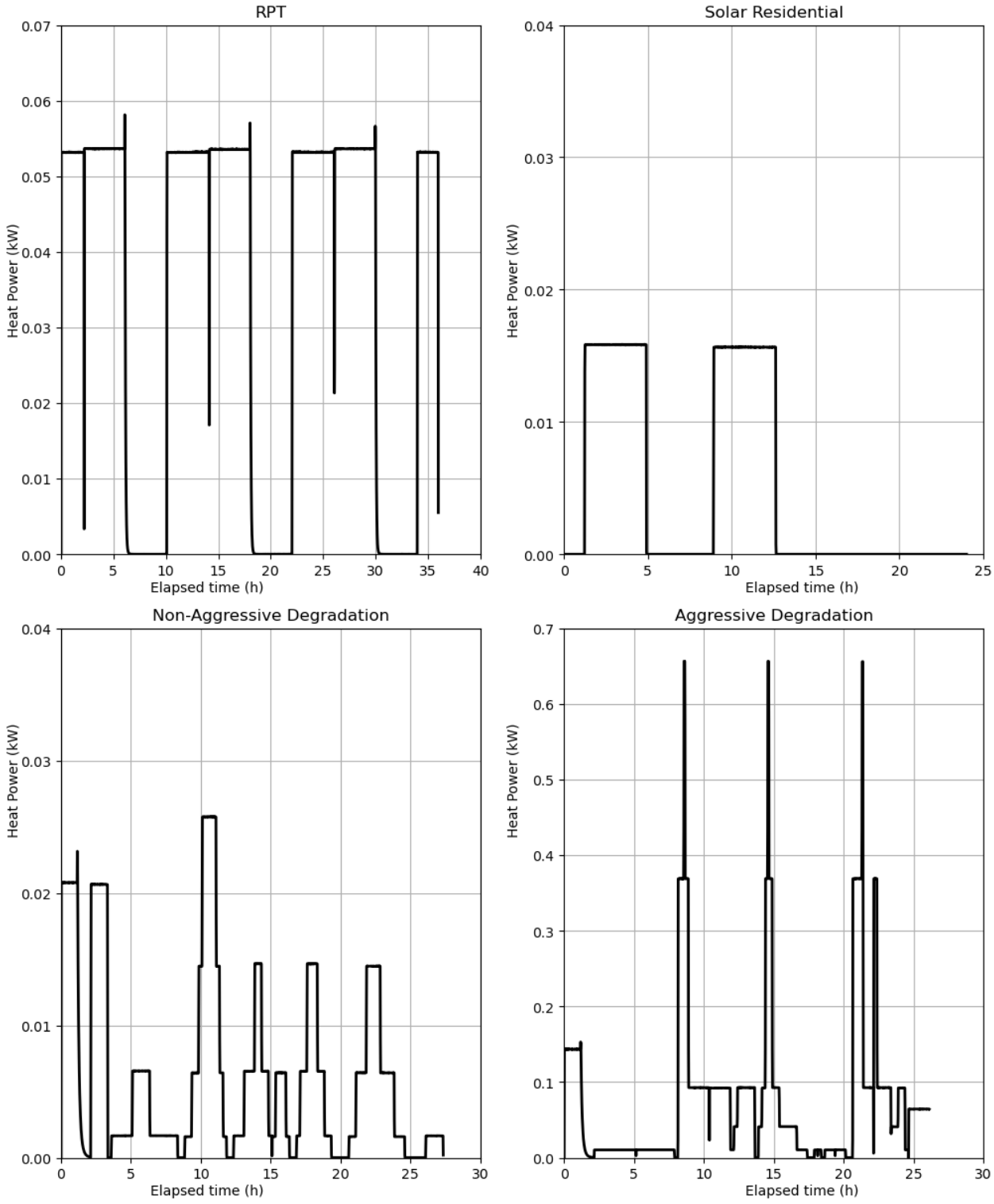

Figure 29: Heat power for the battery signals

5.2.2 Reference Performance Model Results

The figure shows the predicted soil temperatures and the maximum battery temperature when the battery is fully cycled in CCCV mode multiple times. The calculated heat power is also shown in Figure 30. The model predicts increasing temperatures with each cycle as heat from battery cycling is generated. The RPT signal is a four-hour rate signal, which lasted 36 hours for 3 cycles. The battery temperature rises and fall as the heat is generated with each cycle, and peaks at 43 ^{o}C. The cycles are completed following each other, with no extended rest periods in between cycles. Cooling occurs when the battery is in CV mode and less heat is generated, however, this CV time is not sufficient to bring the temperatures to its initial temperature before the next cycle begins. Soil temperatures for position 1 respond quickly to the battery heat, whereas the temperatures at position 2 and 3 respond more slowly. The soil 0.375 m away from the battery rises slowly to 34 ^{o}C. Soil temperatures at position 3 appears to decrease first and slightly increases towards the end of the last cycle of the RPT signal. This suggests heat transport from position 3 further away before the heat from the battery reaches that position and the temperatures begin to increase. The result indicates high thermal mass of the soil and the need for sufficient cooling time for the battery as well as soil temperatures near the battery to fall below a desired temperature before immediately cycling the battery with a high-power signal.

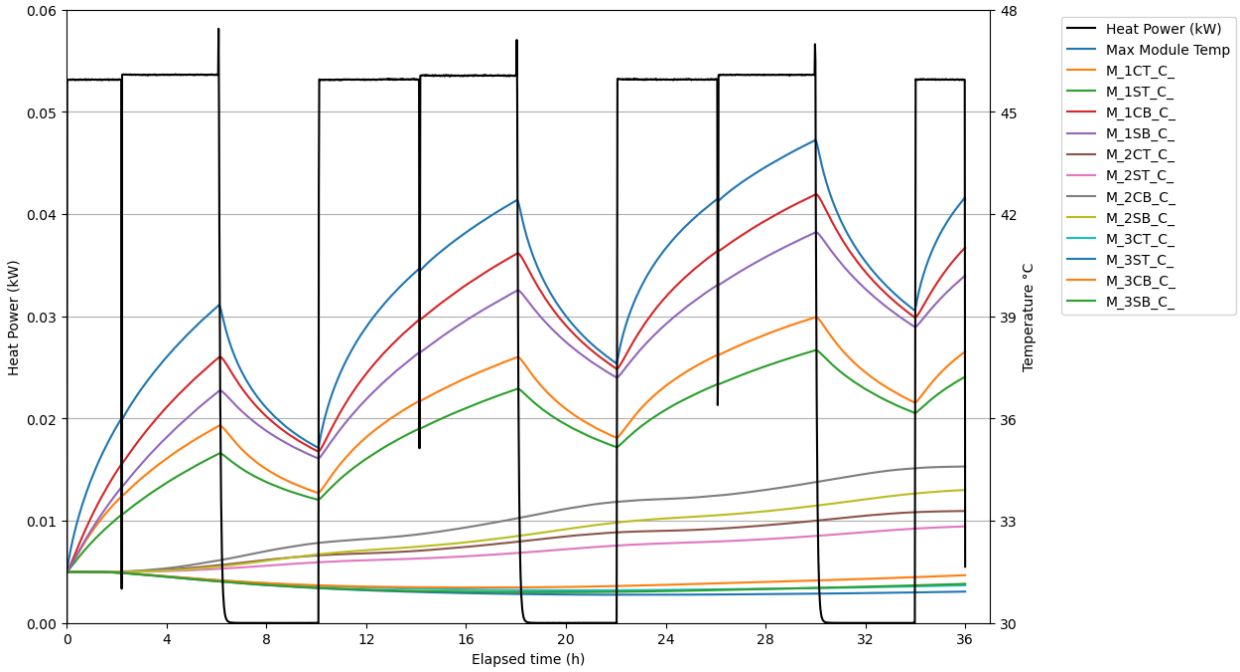

Figure 30: RPT model soil temperature results

The battery temperatures predicted from the model are shown in Figure 31. The chart includes the average temperature of the battery module, and the averaged temperatures from the face of the battery, presumed to be the hottest (the front of the battery), and coolest (the battery face touching the back plate). The temperatures at the front of the battery are presumed to be the hottest and the coolest part of the battery is the face in contact with the back plate. This is because the heat is removed through the back plate. Hence, for a uniform heat generating entity as is represented with the battery module, the heat closest to the back plate is dissipated first, and the temperatures are lower there. Similarly, the front face of the battery will record the highest temperatures as illustrated in the figure below. A maximum temperature difference of 2 ºC is observed between the front and back of the battery.

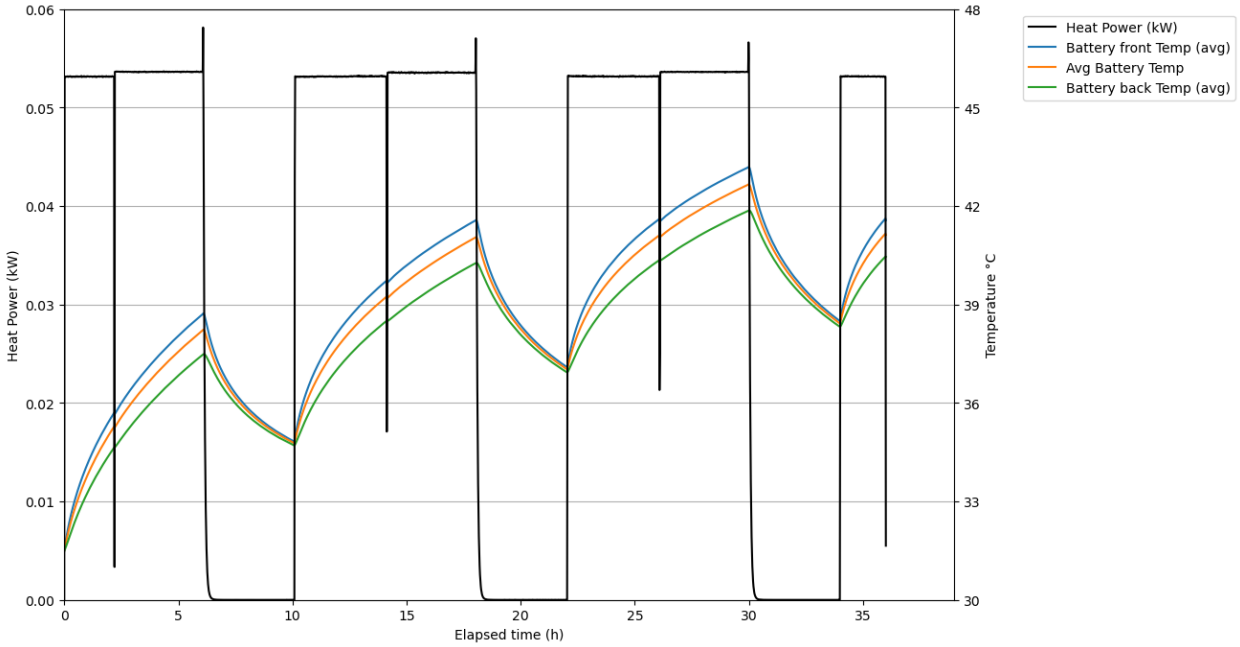

Figure 31: RPT model battery temperatures

5.2.3 Solar test Model Results

The solar test signal is a low energy signal with lengthy rest periods in between. The predicted soil temperatures, maximum battery temperature, and calculated heat power are shown in Figure 32. The result is shown for four consecutive solar test battery cycles, lasting a duration of 4 days. The battery temperature rises and fall as the heat is generated with each cycle, and peaks at 33.5 ºC on the fourth day. The cycles are completed following each other. The model predicts soil temperatures rising very slowly due to low heat rate from the battery. Four consecutive cycles show only a 3 ºC rise from position 1 nearest to the battery. Soil temperatures at position 2 remain almost constant with minute temperature increases as heat travels through with consecutive cycling. Soil temperatures at position 3 appears to decrease first and slightly increases through the four cycles of the signal. This suggests heat transport from position 3 further away before the heat from the battery reaches that position and the temperatures begin to increase. Cooling occurs during the rest period returning the soil temperatures at position 1 almost to its initial temperature. Soil temperatures at position 2, and 3 remain within 1 ºC of the initial temperatures, even after four consecutive cycles, and the maximum battery temperature falls below 32 ºC with each rest period. This suggests that this cycle can be continuously repeated, whilst maintaining a safe working temperature for the battery.

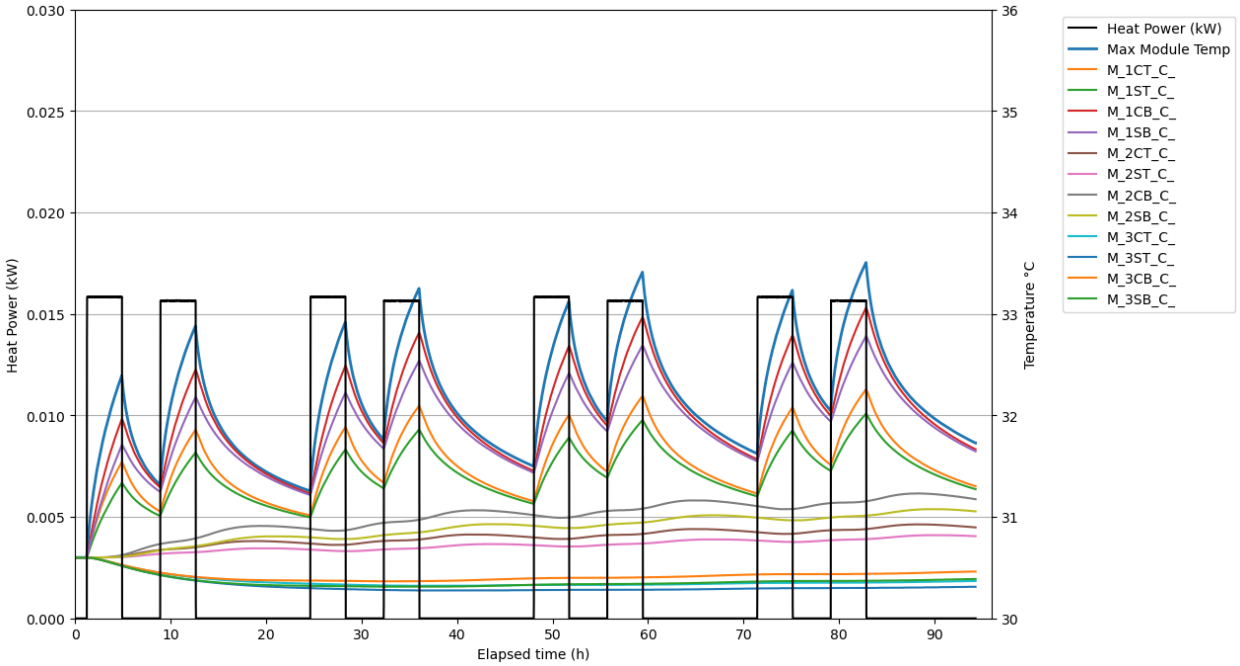

Figure 32: Solar test model soil temperatures result

The battery temperatures predicted from the model are shown in Figure 33. The chart includes the average temperature of the battery module, and the averaged temperatures from the face of the battery, presumed to be the hottest (the front of the battery), and coolest (the battery face touching the back plate). A maximum temperature difference of 0.4 ºC is observed between the front and back of the battery. The battery temperatures remain almost uniform throughout the cycling period for continuous solar battery cycling.

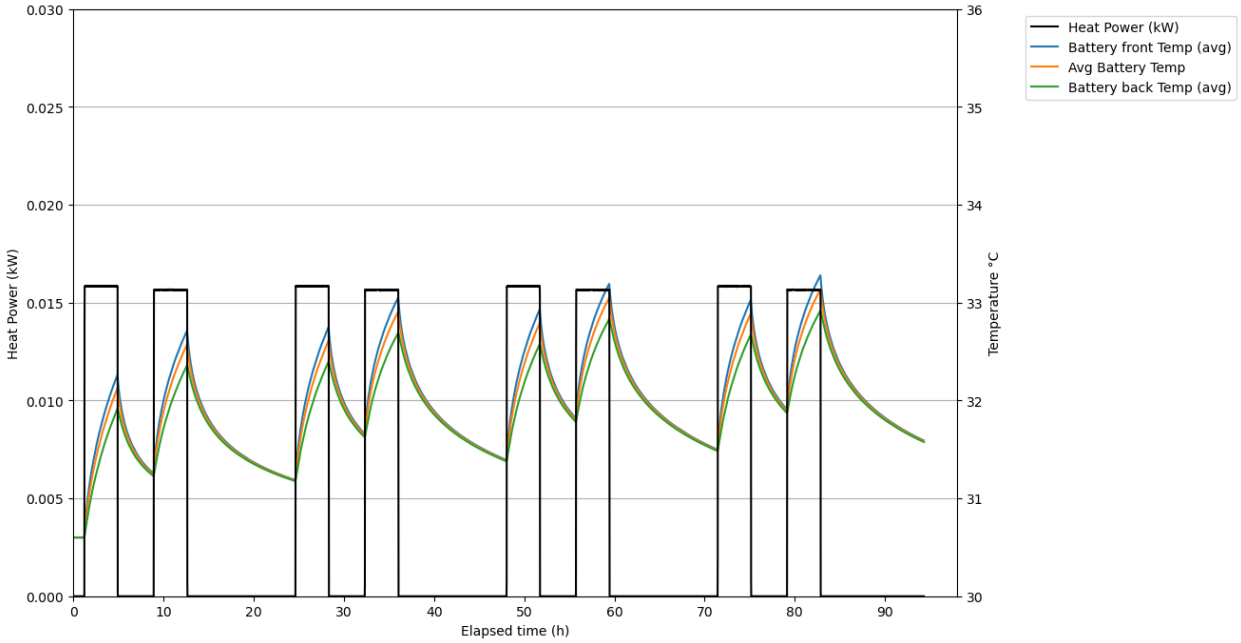

Figure 33: Solar test model battery temperatures

5.2.4 Non-Aggressive Model Results

The non-aggressive battery signal is a low-power output signal with no lengthy periods of rest in the signal. The predicted soil temperatures, maximum battery module, and calculated heat power are shown in Figure 34. The figure shows the soil temperatures for five cycle of non-aggressive battery testing. The battery temperature rises and fall as the heat is generated with each cycle, and peaks at 33.4 ºC on the fifth cycle. The cycles are completed following each other, with no extended period of rest in between cycles. Soil at position 1 respond immediately to heat from the battery, but the temperatures only rise by 2 ºC after five cycles. Soil temperatures at position 2 slowly increase by 1 ºC. Soil temperatures at position 3 appears to decrease first and stay almost constant, slightly increasing through five cycles of the signal. This suggests heat transport from position 3 further away before the heat from the battery reaches that position and the temperatures begin to increase. Cooling occurs during periods of low heat generation in the battery and the maximum battery temperature remains below 34 ºC through five cycles. This suggests that this cycle can be continuously repeated, whilst maintaining a safe working temperature for the battery.

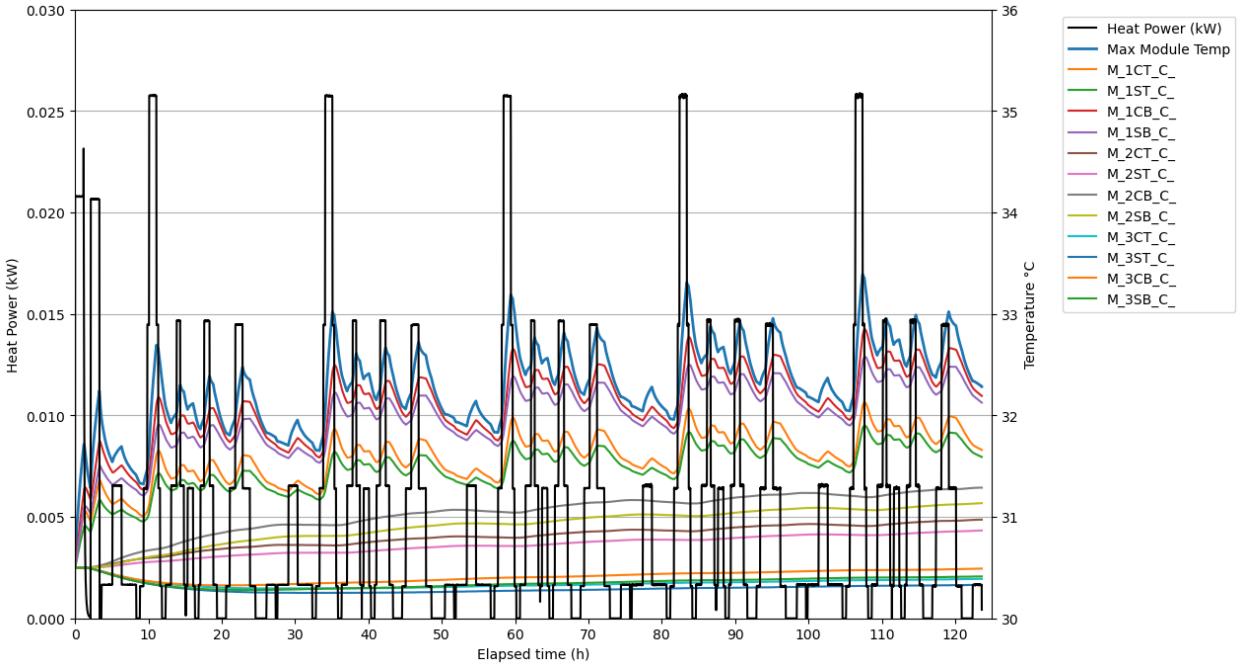

Figure 34: Non-aggressive model soil temperatures result

The battery temperatures predicted from the model are shown in Figure 35. The chart includes the average temperature of the battery module, and the averaged temperatures from the face of the battery, presumed to be the hottest (the front of the battery), and coolest (the battery face touching the back plate). The maximum temperature difference observed between the front and back of the battery remains within 0.5 ^{o}C. The battery temperatures remain almost uniform throughout the cycling period for continuous non-aggressive cycling.

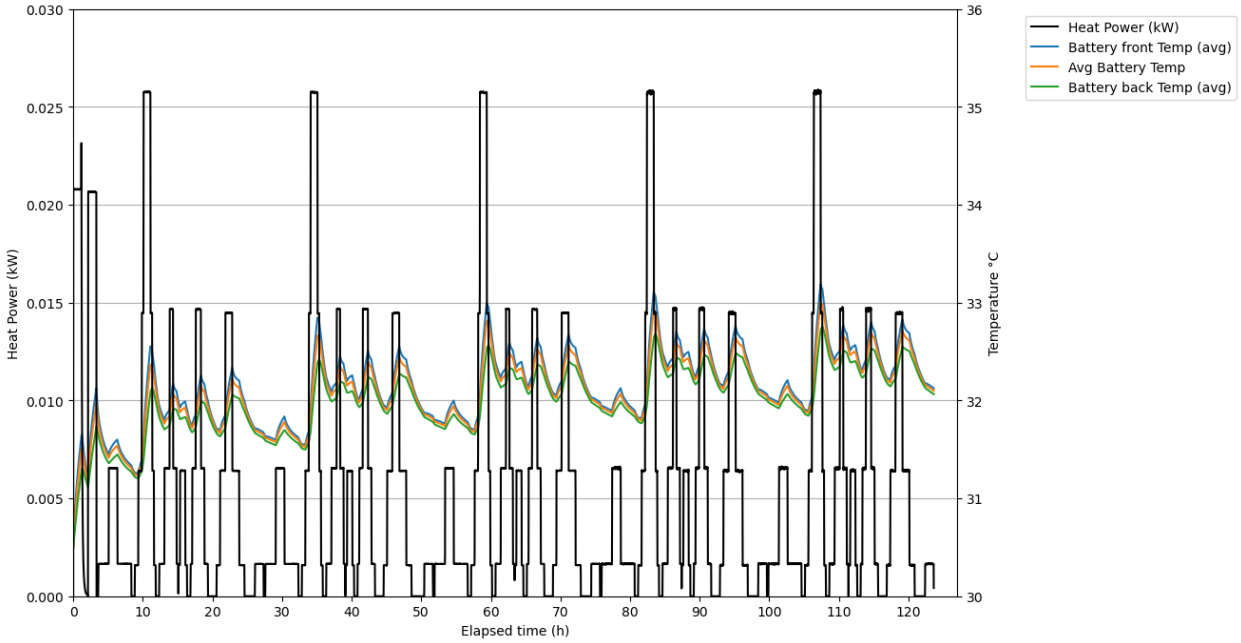

Figure 35: Non-aggressive model battery temperatures

5.2.5 Aggressive Model Results

The aggressive battery signal is a high-power output signal with no lengthy periods of rest in the signal. The predicted soil temperatures and calculated heat power are shown in Figure 36. The figure shows the temperatures for only one cycle of aggressive battery testing. The battery temperature rises and fall as the heat is generated with each cycle, and peaks at 58 ºC Soil at position 1 respond immediately to heat from the battery, rising significantly as the heat rate increases. Soil temperatures at position 2 increases slowly as heat travels through the soil, rising by 5 ºC at the end of the cycle. At position 3, further away from the battery, soil temperatures stay almost constant. Peak soil temperature is 52 ºC from the soil nearest to the battery's mid-point (1CB).

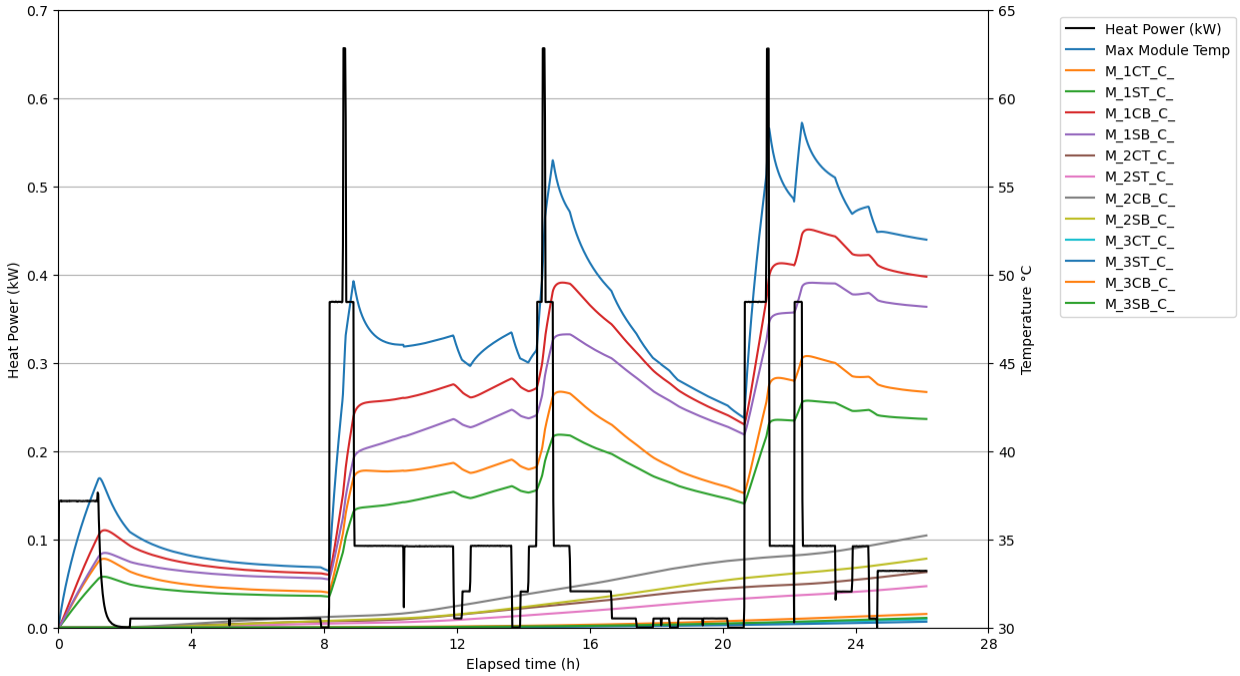

Figure 36: Aggressive model result

The battery temperatures predicted from the model are shown in Figure 37. The chart includes the average temperature of the battery module, and the averaged temperatures from the face of the battery, presumed to be the hottest (the front of the battery), and coolest (the battery face touching the back plate). The model predicts a maximum temperature difference of 7 ^{o}C between the front and back of the battery. This is more than the recommended temperature difference of 5 ^{o}C that is specified in literature

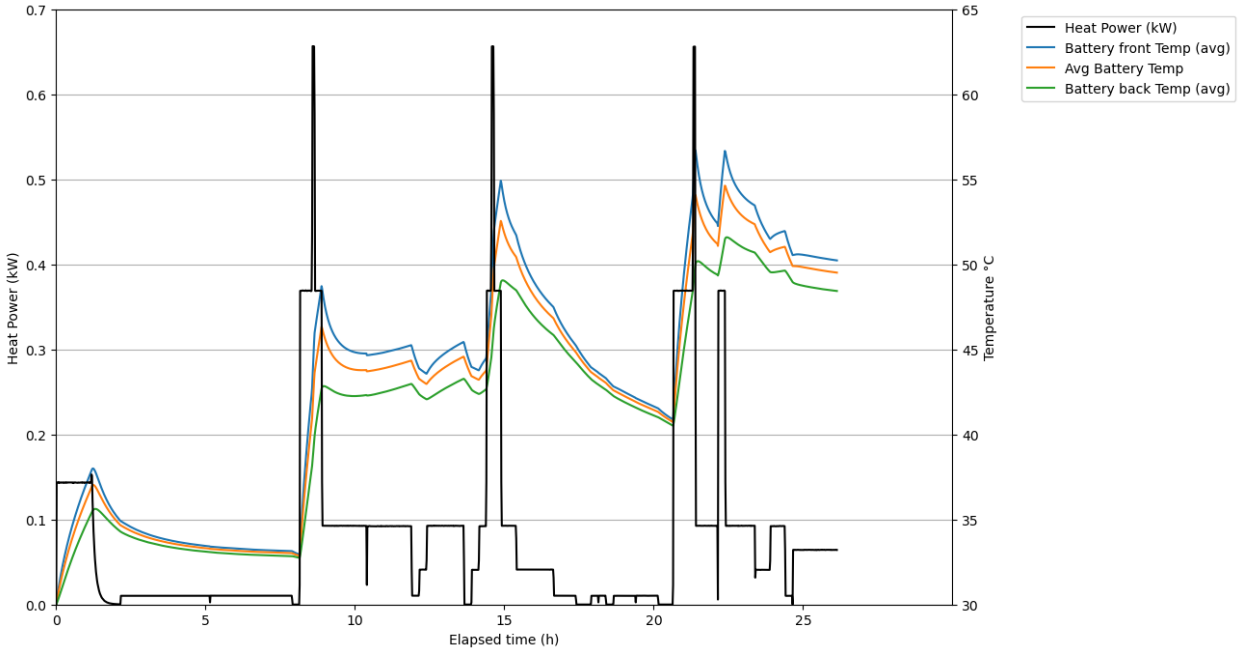

Figure 37: Aggressive model battery temperatures

A summary of the model results is provided in Table 22 below.

Table 22: Summary of model results

SIGNAL	**TOTAL HEAT LOSS (Wh)**	**MAX BATTERY TEMPERATURE**	**MAX SOIL TEMPERATURE (POSITION 1)**	**MAX SOIL TEMPERATURE (POSITION 2)**	**MAX SOIL TEMPERATURE (POSITION 3)**
RPT	426.6	49.9	42.9	34.6	31.5
Solar test	120	34.1	32.4	30.9	30.6
Non-Aggressive	124	33.8	32.2	30.9	30.5
Aggressive	1831	71.9	52.6	35.3	30.9

Chapter 6: Numerical Model Validation

Analytical or numerical model are developed for predicting system behaviours under specified operations or conditions, without needing to carry out experiments. However, the models must be validated with experimental data to determine accuracy and instil confidence in the model before they can be adopted as a representation of the reality for research purposes or project development. This chapter provides a comparison of model results with the results obtained from experiments.

The current study focuses on the thermal dissipation in the soil highlighting the time dependent temperature response of the soil during BESS operation, which may be useful for prescribing a recommended duty cycle for subterranean BESS operation as is appropriate for the intended application. A graphical method of comparison between simulation results and experimental results is adopted and the maximum relative error between experiment and model results are listed in Table 23. comparison between model and experimental results are done individually for each soil location (i.e., 1, 2, and 3), away from the battery, and this is done for the different battery signals. In comparing the model results with experimental results, the initial uniform temperature for each signal is set as the average value. This is due to fluctuating soil temperatures during lab testing as a function of previous experiments. Thus, the initial temperatures, which should be uniform at all points is averaged and used as the initial temperature condition in the model.

Figures 38 compares the battery peak temperature and the soil temperatures at position 1, 2, and 3 for the reference performance battery signal. Figures 39 compares the battery peak temperature and soil temperatures at position 1, 2, and 3 for solar test application signal. Figures 40 compares the battery peak temperature and soil temperatures at position 1, 2, and 3 for the non-aggressive battery signal. Figures 41 compares the battery peak temperature and soil temperatures at position 1, 2, and 3 for the aggressive battery signal. Only one cycle of each signal is used for validation of the model.

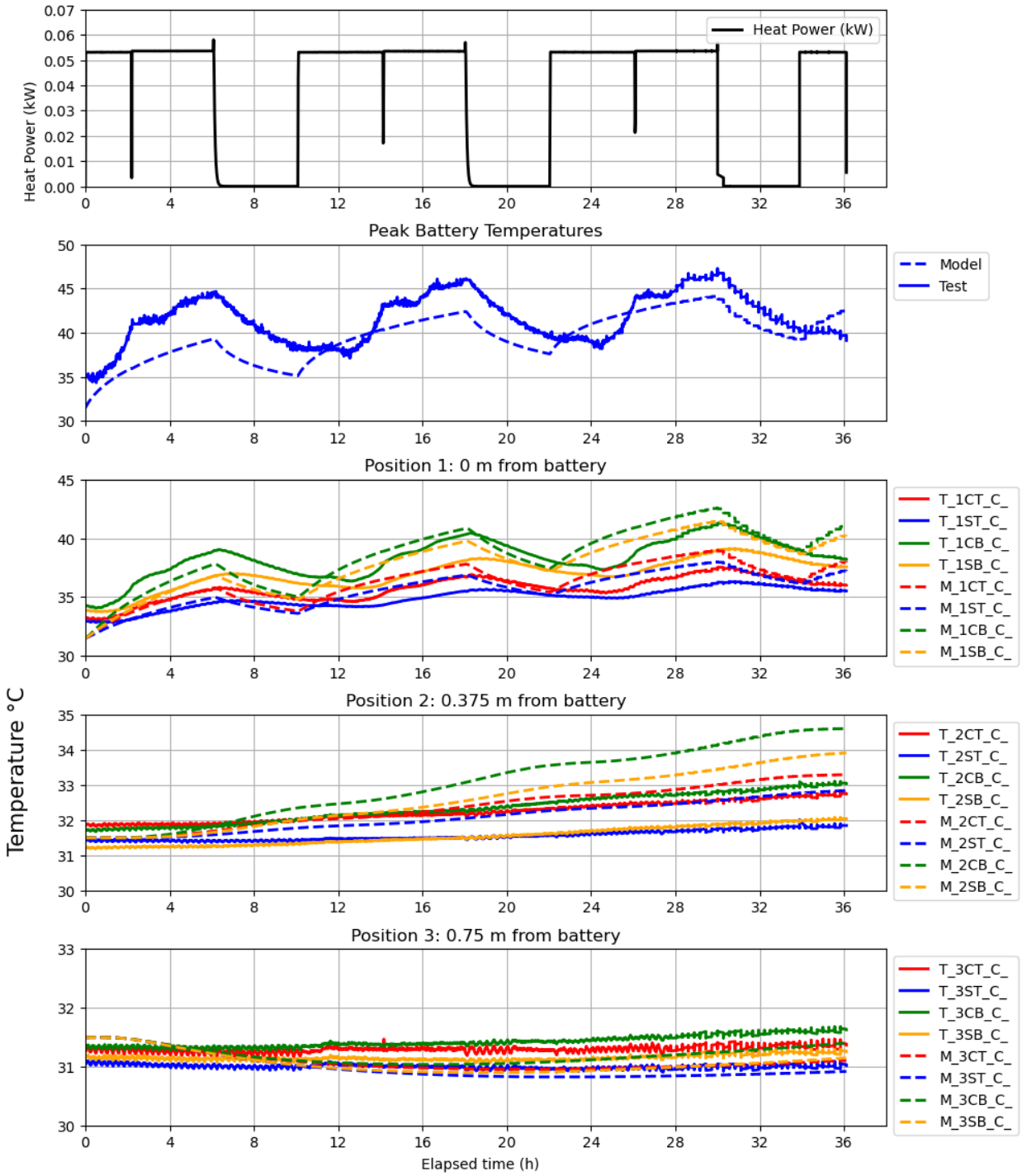

Figure 38: Graphical comparison of model results, ('M_') vs experimental test results, ('T_), for reference performance battery signal

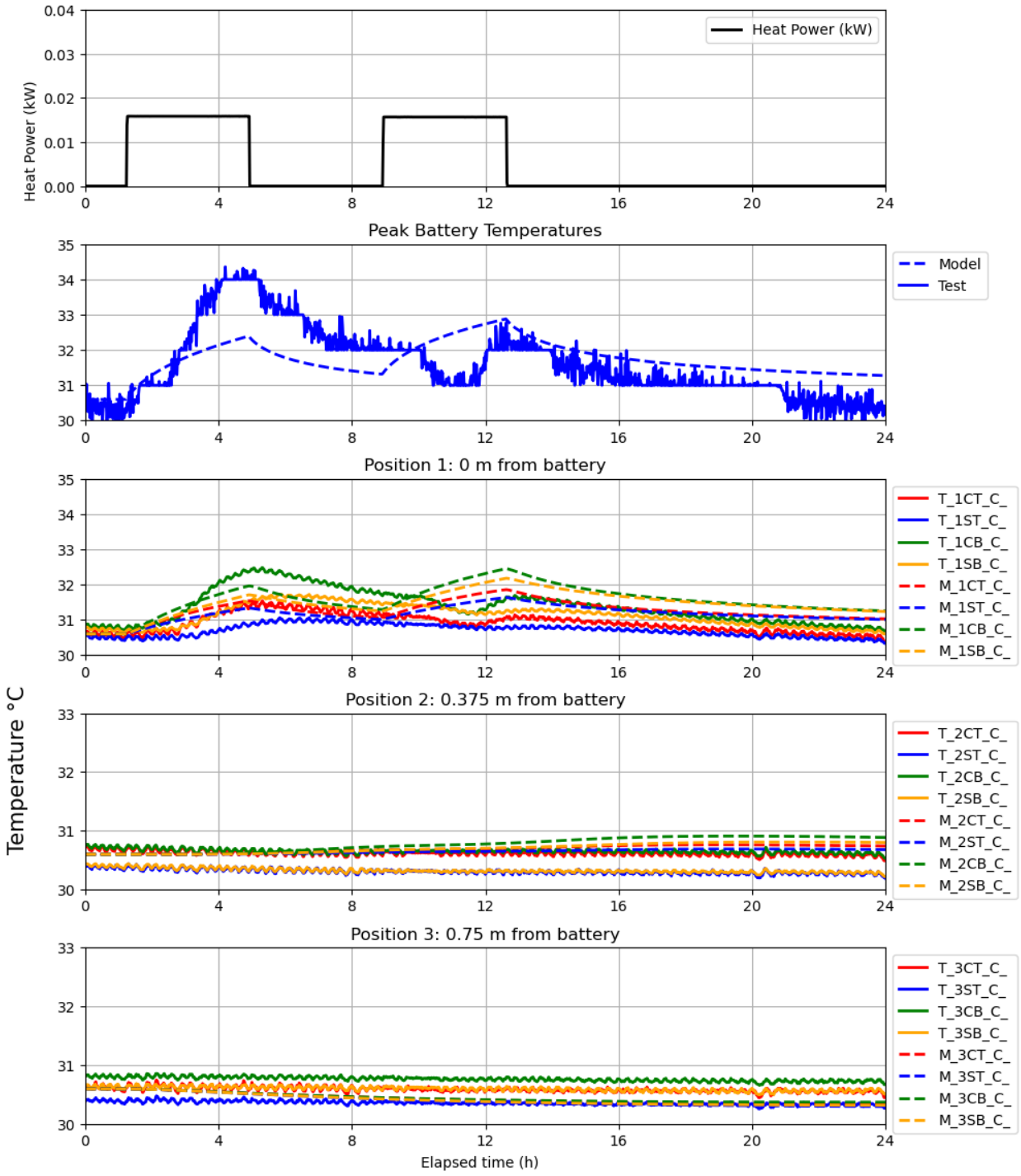

Figure 39: Graphical comparison of model results, ('M_') vs experimental test results, ('T_), for solar test application signal

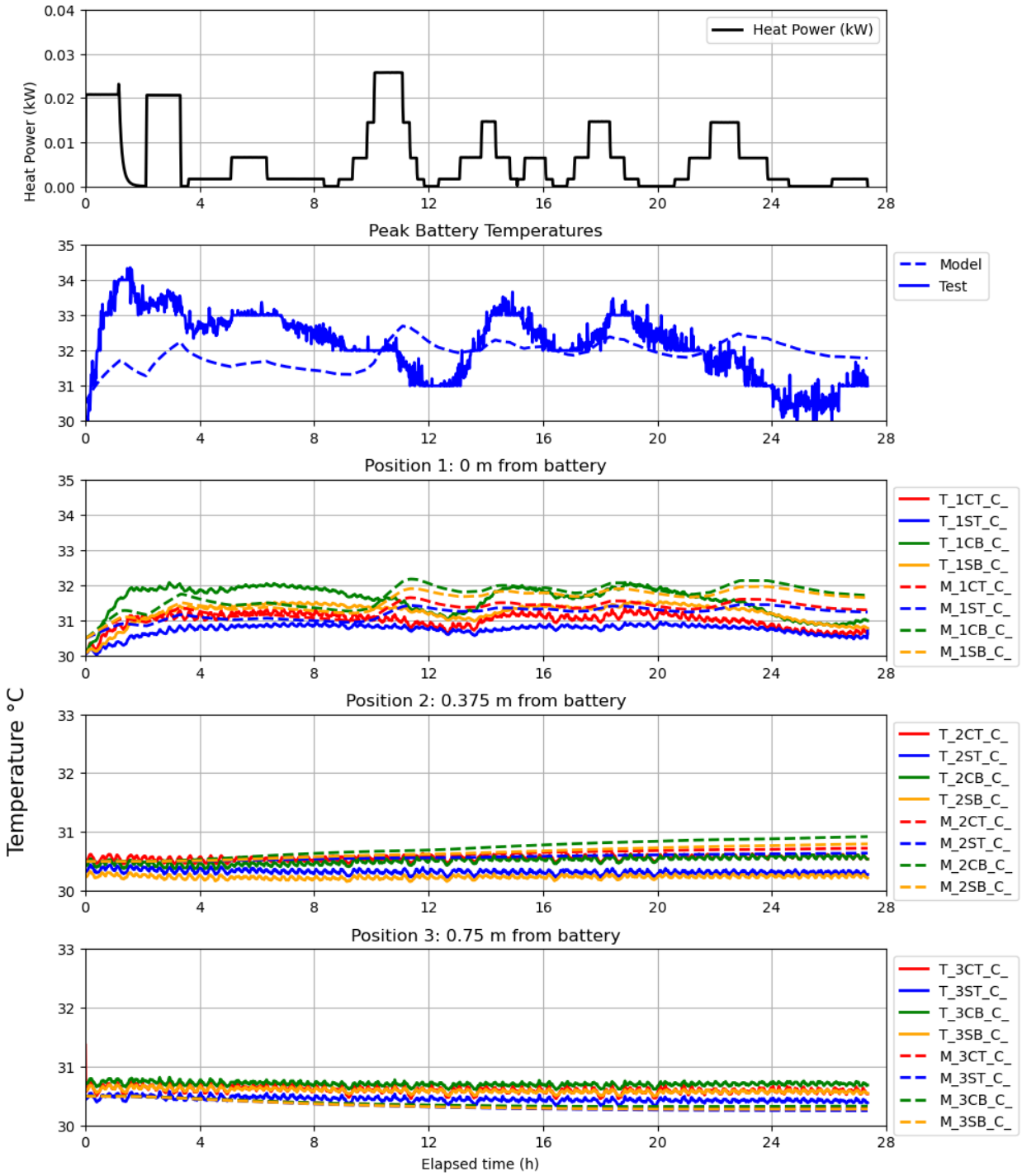

Figure 40:Graphical comparison of model results, ('M_') vs experimental test results, ('T_), for non-aggressive battery signal

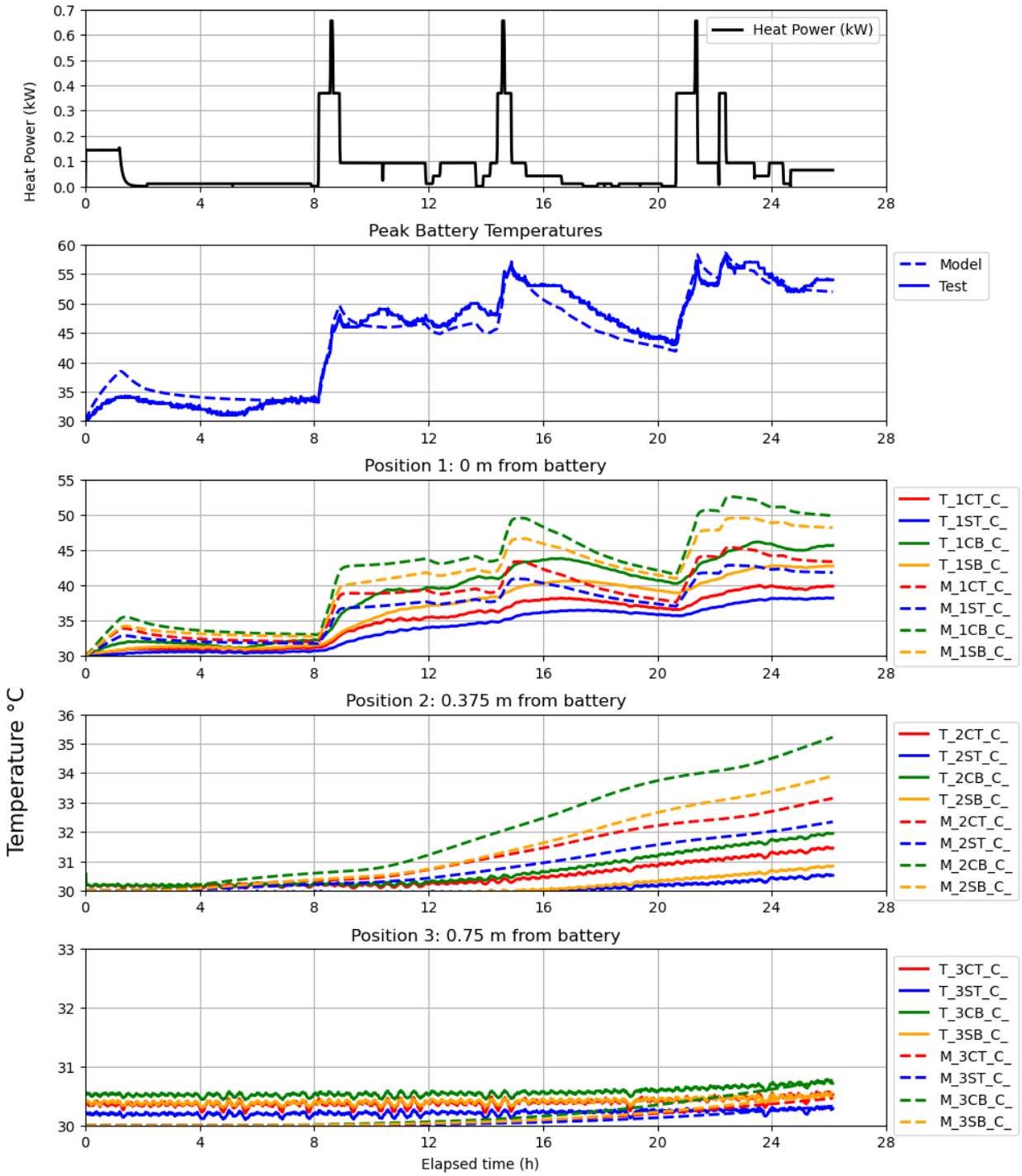

Figure 41:Graphical comparison of model results, ('M_') vs experimental test results, ('T_), for aggressive battery signal

The validation metric used in this work is the root mean square error (RMSE) between the model result temperature values (MV) and the test result temperature values (TV). This is given by the Equation 25 below.

$$RMSE = \sqrt{\frac{\sum_i (TV - MV)^2}{n_i}} \quad (25)$$

where n_i is the number of entries.

Table 23: Root mean square between model and experimental temperature (°C) results

	REFERENCE PERFORMANCE SIGNAL	SOLAR TEST SIGNAL	NON-AGGRESSIVE SIGNAL	AGGRESSIVE SIGNAL
Peak Battery Temperature	2.93	0.86	1.07	2.04
1 CT	1.02	0.44	0.42	3.43
1 ST	1.07	0.51	0.49	3.24
1 CB	1.38	0.49	0.52	3.93
1 SB	1.53	0.48	0.47	4.41
2 CT	0.32	0.12	0.09	0.91
2 ST	0.60	0.35	0.26	0.96
2 CB	0.91	0.18	0.23	1.72
2 SB	1.15	0.40	0.42	1.61
3 CT	0.27	0.17	0.26	0.30
3 ST	0.19	0.09	0.13	0.16
3 CB	0.28	0.32	0.34	0.41
3 SB	0.19	0.19	0.26	0.31

For determining model performance lower RMSE values are desired. The RMSE values are higher for higher heat concentration. The maximum value for RMSE between the model results and test results is 4.41 °C occurring in the center bottom closest to the battery from the aggressive battery signal. The model performance is stronger for low-power signals with low heat generation as the RMSE value is higher for higher power signals. The error may be attributed to unintended heat loss through the insulation of the test unit, or the estimation of the soil heat capacity for the model. Other factors include the measurement of thermal conductivity during laboratory experiments. Thermal conductivity of the soil was tested in small buckets before filling the test unit. There is likelihood of inefficiencies during soil compaction in the actual test unit. Similarly, although the

test unit was lined with vapour barrier, there is a possibility of moisture drift thus affecting the thermal conductivity of the soil where temperature sensors were situated.

Lower battery peak temperatures are observed in the model compared to experimental values. This is attributed to the averaging of the module properties in the model, which implies that the heat from the battery is uniformly generated in the module. However, in reality, the heat is only generated from the battery cells and is transported through the other materials in the module into the soil. Laboratory testing procedures measures and records the temperature at the cell terminal, which is the actual heat source and consequently is the hottest surface on the battery module. The model distributes the heat through the module resulting in lower predicted peak battery temperature. In addition, reversible heat is not considered in this model, however reversible heating does occur during battery cycling. Although the test protocols avoid most of this as reversible heating is dominant at low SOC for low C-rates, low amounts of endothermic heat occurs between 40-60% SOC for the low-rate signals during discharge modes. Thus, this contributes to error between the model and test battery temperature.

The thermal model in this work may be used for further analysis relating to the thermal behaviour of subterranean battery operations and the sensitivity of the adjustable parameters in the model.

Chapter 7: Sensitivity Analysis of the Model

A sensitivity analysis is carried out to determine the dependence of the model on the adjustable parameters of the model. This study focuses on the thermal behaviour in the soil, therefore the two input parameters of significant importance in this study are the thermal parameters: the thermal conductivity and the specific heat capacity. A sensitivity analysis of these two parameters is discussed in this chapter. The aggressive signal is chosen as the signal for exploring the sensitivity of the model to the two thermal parameters because the notable temperature variation observed in the result.

7.1 Variation of Soil Thermal Conductivity

The thermal conductivity of the soil is varied, and results are studied with all the other input parameters kept the same. The heat capacity of 1000 $Jkg^{-1}K^{-1}$, is the same for all scenarios. Figure 42 shows the heat power, and soil temperatures predicted for different thermal conductivities. The test result is included (labeled '*T_XYZ_C_*'). The peak battery temperature from the model result correlates well with test results where the thermal conductivity is 2 $Wm^{-1}K^{-1}$. The soil temperatures nearest to the battery module (i.e., position 1), respond rapidly to heat from the battery, as the heat is initially localized here, and the diffusion area is smallest at this position. Higher soil temperatures are observed where the thermal conductivity value is low as expected because the soil's ability to conduct heat efficiently is poor. At higher thermal conductivities, the soil temperatures are lower because the soil transports heat more efficiently and thus the heat is dissipated faster.

For higher thermal conductivities, quicker rising soil temperatures are observed further away from the battery module, at position 2; 0.375 m away from the battery, and position 3; 0.75 m away from the battery. This is because the heat from the battery conduction is faster and thus the soil temperature response is quicker at higher thermal conductivities. At lower thermal conductivities, heat conduction is poor and inefficient, hence the soil temperatures further away from the source of heat (i.e., the battery) respond slower, as shown in the figure. Nearest to the battery, the measured soil temperature from testing is most similar to the response of the soil, where the thermal conductivity is 4 $Wm^{-1}K^{-1}$. However, further away from the battery, the behaviour of soil temperatures where the thermal conductivity is 1 $Wm^{-1}K^{-1}$ is more similar to the test result. The

correlation between the varying thermal conductivity and the test result does not seem conclusively clear.

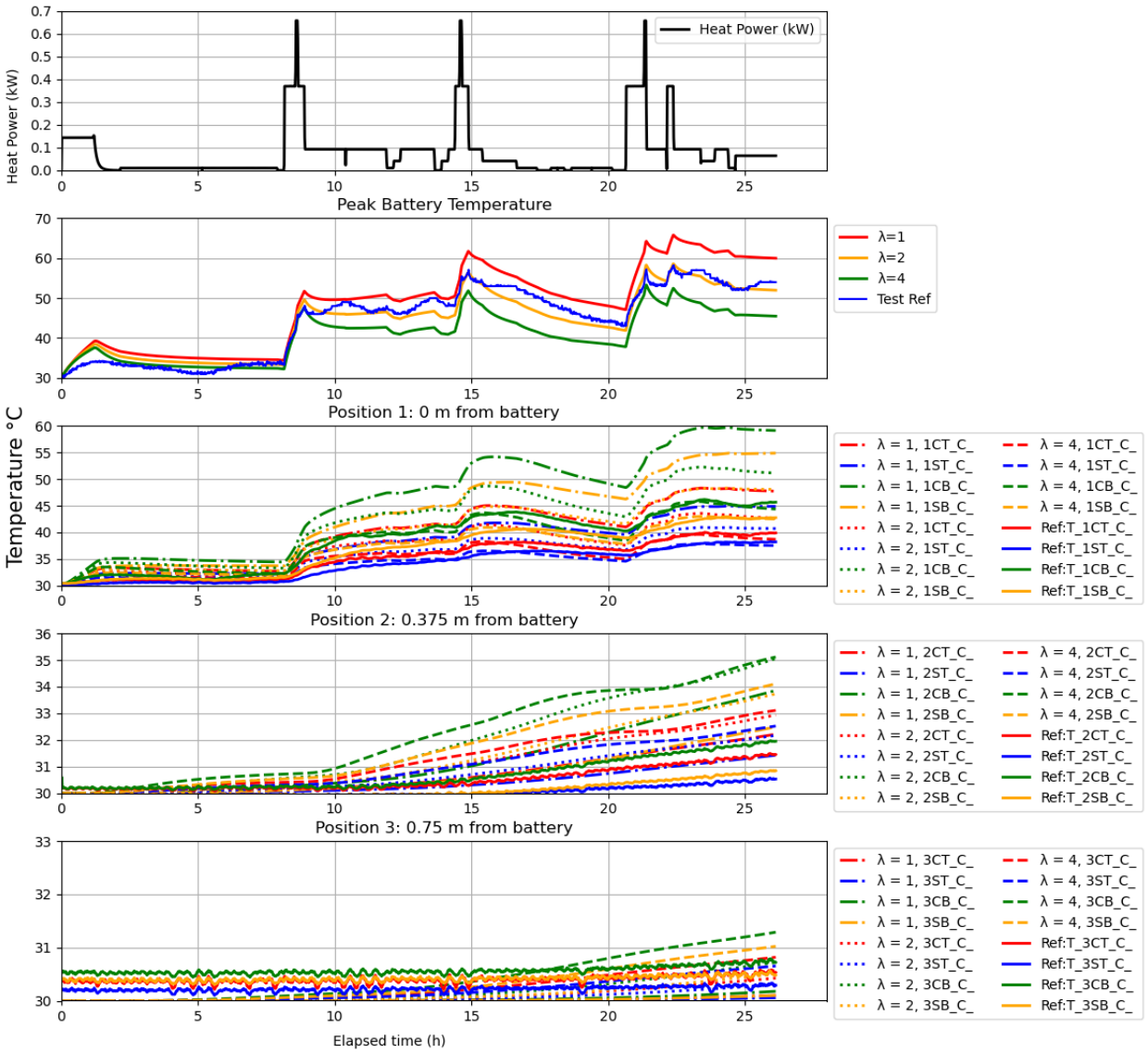

Figure 42:Soil temperatures for different thermal conductivities.

7.2 Variation of Soil Specific Heat Capacity

The specific heat capacity of the soil is varied, and results are studied with all the other input parameters kept the same. The thermal conductivity of 2 $Wm^{-1}K^{-1}$ is the same for all scenarios as measured during soil testing. Figure 43 shows the heat power, maximum battery temperature and soil temperatures predicted for different heat capacities. The test result is included (labeled 'T_XYZ_C_'). The peak battery temperature from the model result correlates well with test results

where the thermal conductivity is 1000 $J.kg^{-1}K^{-1}$. Nearest to the battery, where the heat is initially localized, the soil temperatures are higher for lower specific heat capacity values because the soil's thermal storage capacity is lower. At higher specific heat capacity values, the soil has a higher capacity to hold heat with low temperature increase, hence lower temperatures are observed.

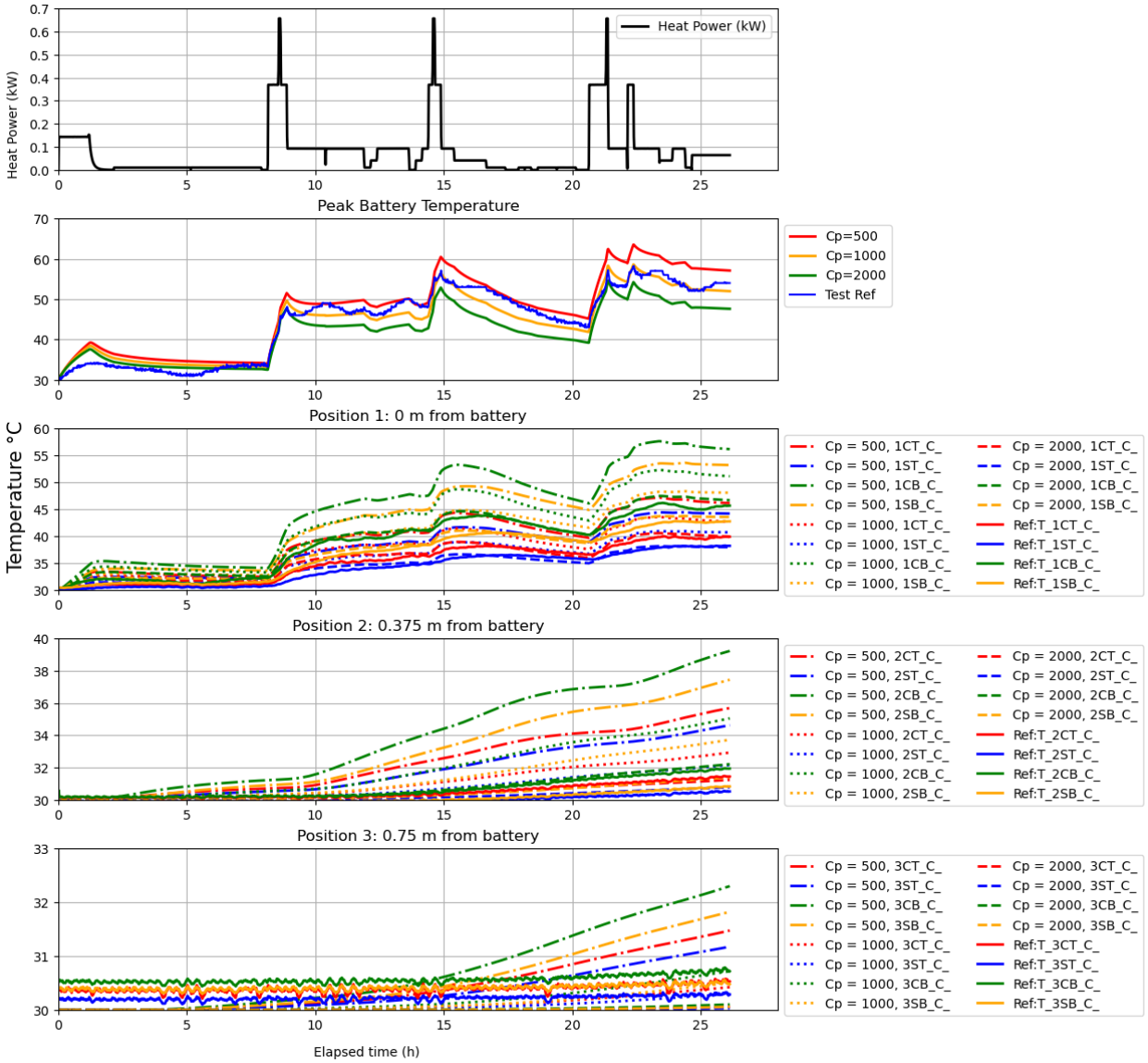

Figure 43:Soil temperatures for different soil specific heat capacity

The figure shows quicker rising soil temperatures further away from the battery module, with lower specific heat capacity values. This is due to low heat retention capabilities; hence the soil warms up quicker, and thus the soil temperatures are higher. At higher specific heat capacities, heat retention is high and temperature changes are less, hence lower soil temperatures are observed

further away from the battery as shown in the figures. The soil temperature result is most closely aligned with the measured test result when considering a heat capacity of 2000 $J.kg^{-1}K^{-1}$, at all positions in the soil.

Figures 42 and 43 show that the variation of either thermal input parameters, the thermal conductivity of the soil and the specific heat capacity of the soil, influences both the soil temperatures and the heating or cooling time. An optimization of these parameters tailored to the battery operation may be done for best battery performance.

7.3 Optimization of Parameter Variation

The thermal conductivity and specific heat capacity of the soil are varied, with all the other input parameters kept the same. From section 7.1 and 7.2, the soil temperatures from the test result closely aligns with the model results where the soil has a heat capacity of 2000 $J.kg^{-1}K^{-1}$, and there was no clear alignment with the variation of thermal conductivity values. Therefore, the soil thermal response is compared for heat capacity of 2000 $J.kg^{-1}K^{-1}$ with different thermal conductivities and compared to the test result. The resulting soil temperature response is most closely aligned with the test result when considering a heat capacity of 2000 $J.kg^{-1}K^{-1}$ and thermal conductivity of 2 $Wm^{-1}K^{-1}$.

Near the battery, the highest soil temperatures are observed for soil with low thermal conductivity. This is due to poor heat conduction through the soil, hence the soil temperatures are higher. Similarly, where the soil possesses high thermal conductivity, efficient heat conduction and retention capabilities of the soil leads to lower temperatures, which is shown in the Figure 44. Further away from the battery, the reverse is the case as the heat travels quicker for higher thermal conductivities, causing the soil temperatures to increase more rapidly.

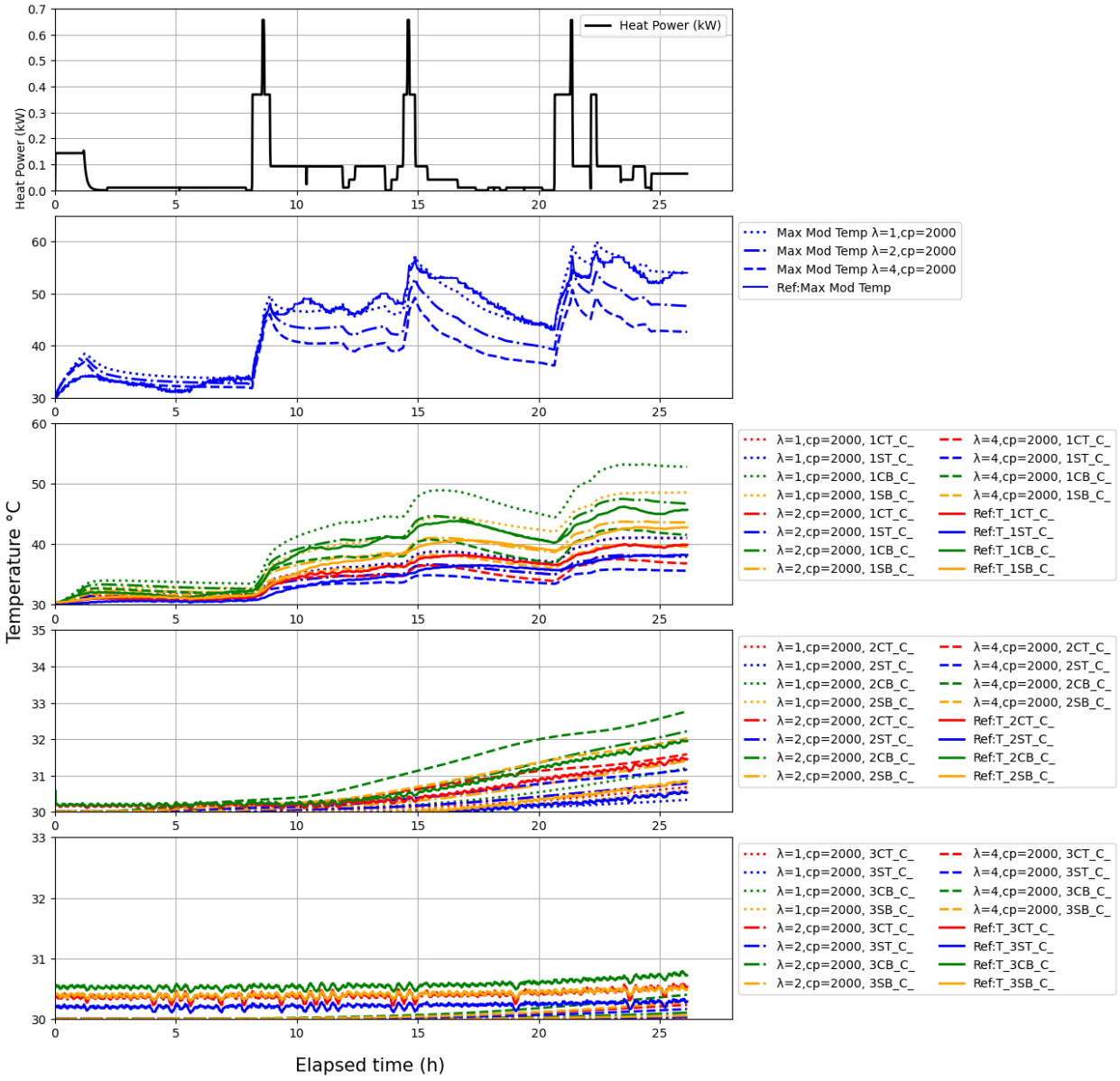

Figure 44: Soil temperatures variation for changing thermal conductivity and specific heat capacity value of 2000 J.kg⁻¹K⁻¹.

Chapter 8: Parametric Analysis of the Model

A parametric analysis is done to study the impacts of ground temperatures, geometry, and different isothermal surface distances from the battery, on the heat diffusion rate and resulting battery temperatures. The aggressive signal is used for this parametric study because of the notable temperature variation in the model results. In this analysis, every other input parameter is kept the same apart from the varied parameter of concern for the analysis. Individual soil positions (1, 2, or 3) are shown.

8.1 Variation of Ground Temperatures

The influence of ground temperatures on the soil thermal response for subterranean battery operations are discussed in this section. The soil temperatures at position 1, 2, and 3 follow the same trend as the model result presented in section 5.2.5. The influence of the initial ground temperature parameter on the result is shown in the peak temperatures reached for both the battery and the soil. However, there are no observable influence of ground temperatures on the cooling or heating rate of the battery and the soil. Lower ground temperatures result in lower peak temperature for the battery and the higher ground temperatures result in higher peak battery temperature as heat is generated from the battery and transported through the soil. This is shown in Figure 45. The results show that for a 5^{o}C lower ground temperature, the peak battery temperature is reduced also by 5 ^{o}C, indicating a linear relationship between ground temperatures and peak battery temperatures.

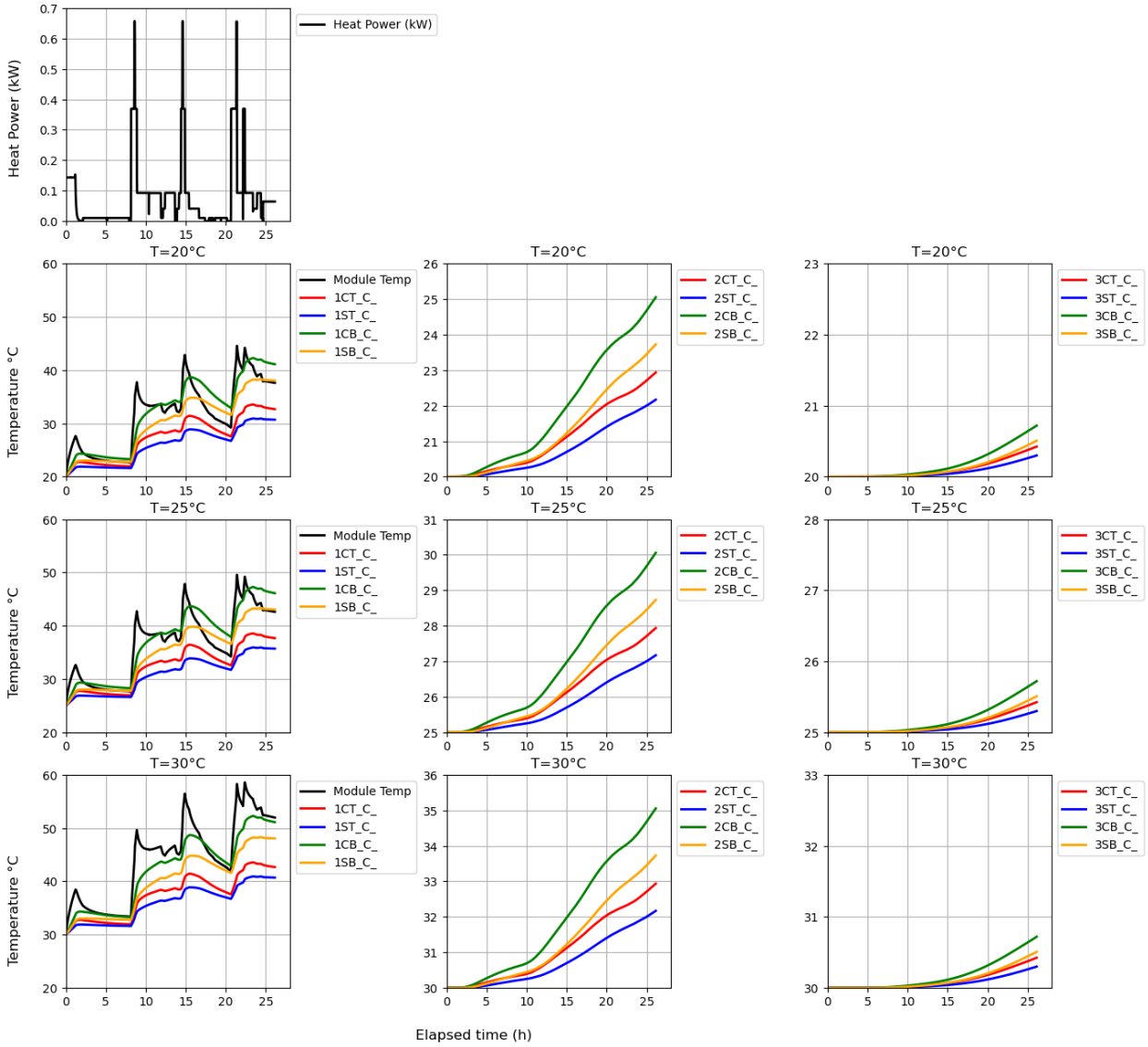

Figure 45:Model results at different ground temperatures

8.2 Variation of Geometry

The soil thermal response for a different geometry shape of the battery is studied in this section. The geometry is altered such that the battery pack is now a four-sided polygon as seen in Figure 46, and the heat is transported from the battery through the soil across a wider arc creating more heat pathways and increased volume of soil for heat storage. Figure 47 shows the battery temperature and changing soil temperatures through the soil at positions nearest to the battery, 0.375 m away from the battery and 0.75 m away from the battery.

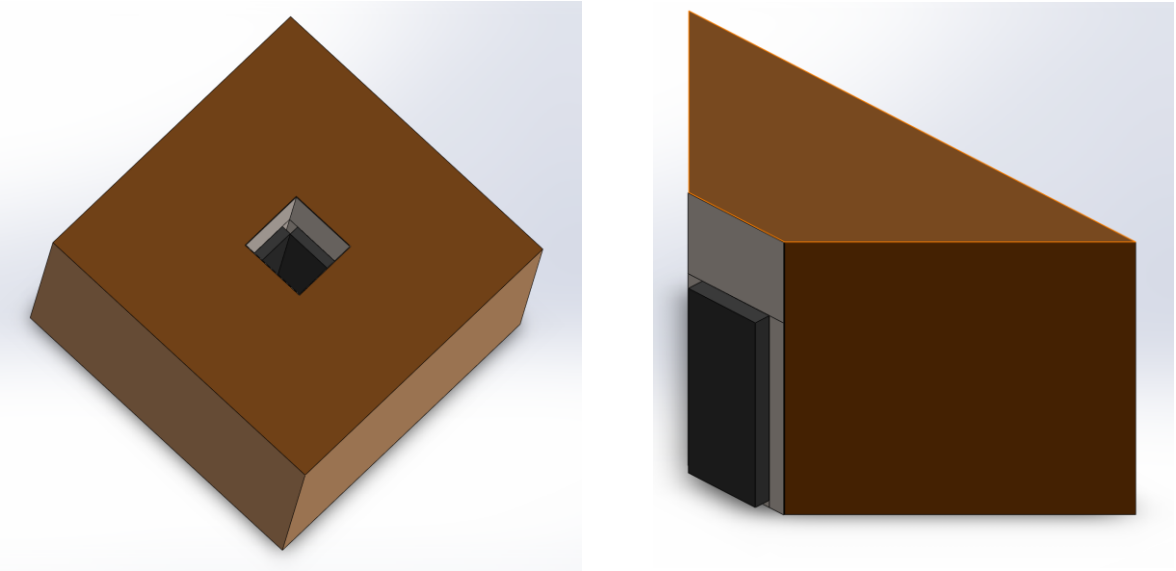

Figure 46: model with four -sided pack geometry

Figure 47 shows that the soil temperatures follow the trend of the model result presented in section 5.2.5, lower temperatures are observed which can be appropriated to the heat pathway of the geometry. Compared to the six-sided pack, a higher heat diffusion rate is observed for a four-sided pack due to the added pathways for heat flow and the peak battery temperatures are reduced by 4 ^{o}C, which is not a big difference. Therefore, the shape of the battery pack does not reflect a strong influence on the maximum battery temperature. The center bottom position where heat dissipation is least efficient due to having the least number of heat pathway is shown in Figure 47

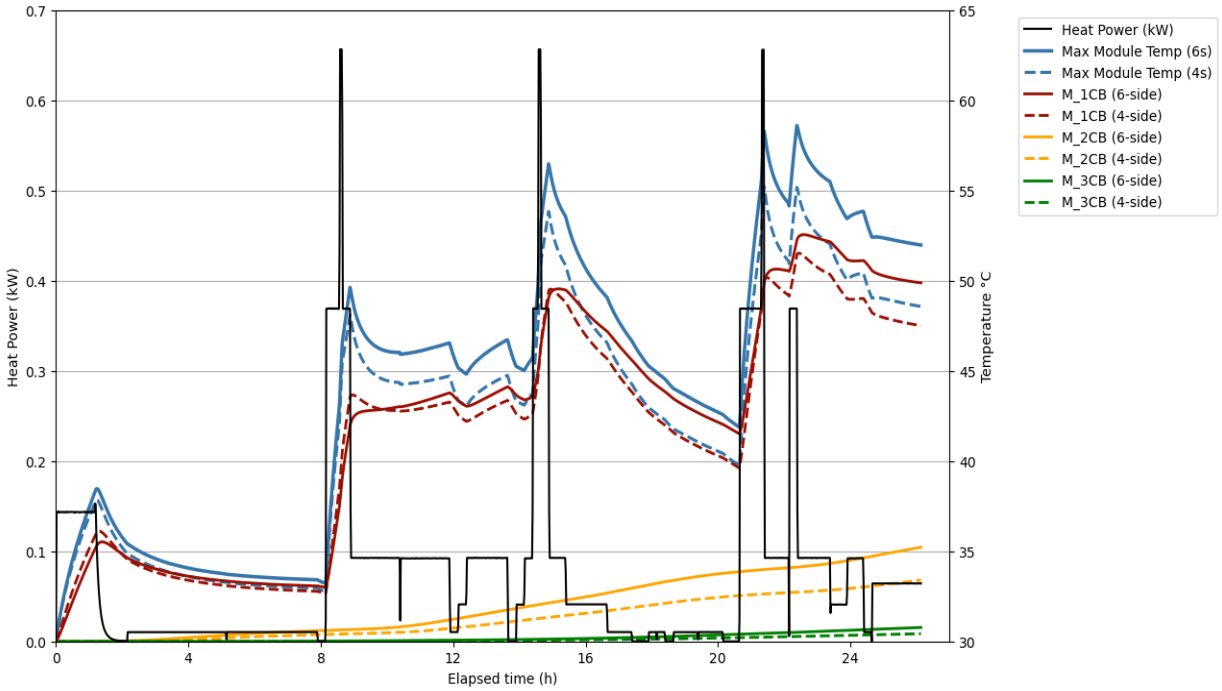

Figure 47: Soil temperatures for rectangular pack geometry vs hexagonal pack geometry

8.3 Variation of Isothermal Surface Distance

The isothermal surface distance was varied for studying the effects, if any on the heat diffusion and soil temperatures. Previous model results are given for a distance on 1 m between the battery and the isothermal surface. In investigating this impact of this distance, the model was adapted, and the isothermal surface was set at 4 m away from the battery. Soil temperatures are measured and recorded at the same positions previously set and compared. The center bottom position where heat dissipation is least efficient due to having the least number of heat pathway is shown in Figure 48.

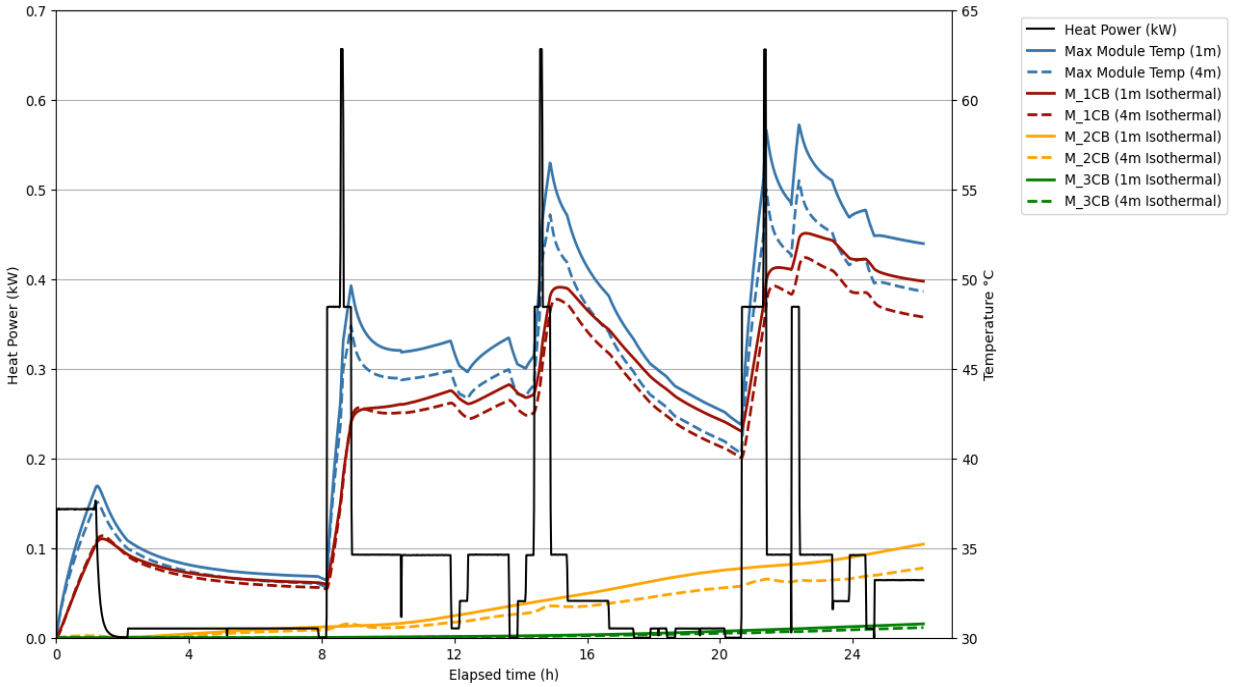

Figure 48: Soil temperatures for an aggressive cycle where isothermal surface is 4 m vs 1 m away from the battery

Figure 48 shows a peak battery temperature of 55 ºC for the isothermal surface set at 4 m away from the battery which is 3 ºC less than the peak battery temperature of 58 ºC, where the isothermal is set at 1 m. The heat diffusion rate for a 4 m isothermal surface is higher compared to that a 1 m isothermal surface. This is not a big difference as the temperatures are only 3 ºC lower, indicating that the influence of the distance of the isothermal surface from the battery is limited beyond 1 m. For a single aggressive cycle, the soil temperature at 0.75 m away from the battery remains almost constant, only increasing by 1 ºC. Continuous cycling of this duty cycle having significantly more heat transported through the soil would prompt a more notable response at this position with increasing cycles. However, for a low-power signal with low heat generation, the soil temperature at 0.75 m away from the battery remains unchanging, only increasing after many days of constant cycling. There are only a few degrees difference between the results between an isothermal soil surface of 1 m away from the battery, and that of 4 m. This is noteworthy for scenarios where multiple subterranean battery units sited at 1 m from each other, are cycled aggressively, it is most likely that heat generated from one battery will have an impact on the other. However, at a 4 m spacing between units, the likelihood of impact from one BESS unit on the next is minute suggesting an optimum distance between the units lies between 1 m and 4 m. Consecutive aggressive cycles with no cooling period in between cycles will result in increasing soil

temperature and consequently larger impacts on nearby BESS units. This may be investigated in future research.

8.4 Summary

In summary, the variation of parameters such as the ground temperatures, geometry or battery operation signal influences the soil temperatures and heat dissipation time for heating or cooling. A high-power signal will generate more heat and thus lead to higher temperatures of the battery and through the soil. This is an important for determining battery application for subterranean battery installations and the iteration of battery operation. The underground temperatures influence peak temperatures around the battery linearly but has no impact on the heating or cooling rate of the battery or the soil. Higher ground temperatures result in higher peak temperatures, as heat travels through the soil, and lower ground temperatures produce lower peak temperatures. The geometry also influences the thermal dynamics as it is dependent on the heat diffusion area for heat dissipation. Less diffusion area means less heat pathways and thus higher soil temperatures and more diffusion time. A wider area for heat diffusion leads to faster heat diffusion and lower temperatures. However, the impact of the battery pack geometry is minor, and the soil temperatures will vary only slightly.

Chapter 9: Conclusion and Recommendations

The installation of stationary BESS continues to grow as renewable energy systems are integrated in the electricity grid. Residence and commercial establishment adopt this technology for various applications. Though BESS has proven to be a key player in the energy system, there are obstacles to the widespread adoption of this technology due to concerns from homeowners or owners of commercial establishments. These concerns surround the installation site of the system such as safety concerns, noise pollution, structural footprint etc. Burying the battery in the ground provides a strategy for addressing these concerns and increasing BESS installations. Previous work done on BESS highlights the importance of battery thermal management, therefore battery installations are predominantly above-ground for increased accessibility. However, the consideration of the ground as an infinite heat sink or storage medium for battery thermal management is not considered in previous studies. To support these types of battery installations and operations, this thesis studies the thermal dynamics of a subterranean battery's ambient environment (i.e., the soil) during battery operation. The thesis used current signal data applicable to residential load applications to determine heat generation in the battery and simulate the thermal response of the soil.

The conclusions from this study drawn from the results and research objectives in section 1.2, are discussed in this chapter and are presented below:

- The model results show that the temperature response of the soil during battery operation is influenced by several factors such as the operation signal, geometry of the battery module, and the soil thermal properties. These parameters may be optimized for maintaining desired temperature conditions suitable for a unique application or environment.
- The rate of heat dissipation is predominantly dependent on the thermal properties of the soil. This is highlighted by the results discussed in chapter 7. Therefore, for subterranean battery operations in colder climates, where heating is essential, a specialized soil type of higher specific heat capacity and lower thermal conductivity of the soil may be filled in the immediate areas that surround the battery module. Therefore, the heat from the battery is stored in the soil and warms up the battery when needed. Where cooling is prioritized, high thermal conductivity and specific heat capacity of the soil should be filled nearer to the battery.

- The ground temperature linearly impacts the peak battery temperature, i.e., by defining the initial ground temperatures at 5 ºC lower than previous value, the resulting peak battery temperatures are reduced by 5 ºC. Similarly, increasing the initial ground temperature by 5 ºC increases the resulting peak battery temperatures by 5 ºC. The ground temperatures have no influence in the heating/cooling rate of the battery.
- The geometry of the battery pack determines the heat pathways from the battery. However, it has little impact on the peak battery temperatures.
- The occurrence of an average steady temperature trend is determined by the battery signals and the frequency of recurrent cycles. Sufficient rest or periods of low heat generation rate provides time for the temperatures to return to the initial state before the next duty cycle, thus leading to a steady temperature trend for each duty cycle. The ambient (soil) temperatures directly affect the battery temperature; thus, a steady temperature trend implies a consistent degradation pattern of the battery as a function of temperature.
- The operation of BESS underground is subject to the temperature response for each individual battery signal. Therefore, cycling and power capabilities may be limited. For example, the aggressive signal for peak shaving applications results in high soil temperatures up to 50 ºC near the battery. Consecutive cycles of this nature with no cooling period in between cycles will result in significantly increasing temperatures which directly affects battery temperature and degradation rate. However, the non-aggressive signal from light-duty residential load exhibits lower soil temperatures and the cycle may be repeated multiple times consecutively, while remaining below 40 ºC. In order to maintain battery operation within a desired temperature range and for optimal performance, it may be necessary to create a duty cycle considering the temperature response of each signal, rest periods, and periods of low heat generation from the signal.
- Subterranean BESS operation for residential applications may be continuously utilized efficiently for a single low-power application with limited concerns, however for higher-powered applications, this may not be feasible, hence a combination of multiple applications such as peak-shaving and light-duty residential application may be recommended.

9.1 Future Research Areas

The model developed in this work is a basic one which assumes the battery as a single homogenous entity with uniform thermal properties. This assumption may have led to overestimation of some parameters. Hence, there are several areas that may be improved, which are discussed in this section alongside other areas of consideration for future works on subterranean battery operations.

- The battery is modeled as a single homogenous entity, which is not the reality. Although the battery temperature trend provides useful information for cycling and power limitations, the battery temperature may not be viewed as a very accurate temperature values during battery cycling. A more detailed cell-level model of the battery may be utilized for this study, which will produce more accurate results.
- The model may be adapted for varying geometries, ground temperatures and soil thermal properties for specific scenarios.
- Nearer to ground surface, soil temperatures are influenced by climatic factors. Thus, for BESS installations in this region (between 0 – 20 m), the temperature of the ground will vary along the height of the system. Future works on this topic includes an investigation of the impact of this variation on the battery's thermal dynamics.
- This work assumes that heat will flow only radially. However, in reality, heat will flow through the top and bottom of the pack, which will impact the heating/cooling rate of the battery and the battery peak temperatures. This can be investigated in the future.
- A potential research area for future investigation of subterranean battery operation is a recommended optimal distance between the placement of battery packs to mitigate the mutual influence of heat dissipation from the batteries. This investigation may provide a means of adopting subterranean BESS installations at a bigger scale than residential such as utility or community scale.
- The model may be further studied for other BESS applications such as frequency regulation, load shifting etc., and thus control strategies would need to be developed for optimal BESS operations to maintain steady temperature trends for continuous operation and a steady degradation pattern.

- A method of combining various stationary energy storage applications based on the temperature response of the soil to each unique application may be developed for continuous BESS operation underground depending on the environment.

References

[1] J. Leadbetter and L. G. Swan, "Selection of battery technology to support grid-integrated renewable electricity," *J. Power Sources*, vol. 216, pp. 376–386, Oct. 2012, doi: 10.1016/j.jpowsour.2012.05.081.

[2] H. Chen, T. N. Cong, W. Yang, C. Tan, Y. Li, and Y. Ding, "Progress in electrical energy storage system: A critical review," *Prog. Nat. Sci.*, vol. 19, no. 3, pp. 291–312, Mar. 2009, doi: 10.1016/j.pnsc.2008.07.014.

[3] P. Pon Ragothama Priya, S. Baskar, S. Tamil Selvi, and C. K. Babulal, "Optimal Allocation of Hybrid Renewable Distributed Generation with Battery Energy Storage System Using MOEA/D-DRA Algorithm," *Int. Trans. Electr. Energy Syst.*, vol. 2023, p. e7316834, May 2023, doi: 10.1155/2023/7316834.

[4] X. Su *et al.*, "Sequential and Comprehensive BESSs Placement in Unbalanced Active Distribution Networks Considering the Impacts of BESS Dual Attributes on Sensitivity," *IEEE Trans. Power Syst.*, vol. 36, no. 4, pp. 3453–3464, Jul. 2021, doi: 10.1109/TPWRS.2021.3051629.

[5] M. R. Jannesar, A. Sedighi, M. Savaghebi, and J. M. Guerrero, "Optimal placement, sizing, and daily charge/discharge of battery energy storage in low voltage distribution network with high photovoltaic penetration," *Appl. Energy*, vol. 226, pp. 957–966, Sep. 2018, doi: 10.1016/j.apenergy.2018.06.036.

[6] W. Zhang and S. Wang, "Optimal Allocation of BESS in Distribution Network Based on Improved Equilibrium Optimizer," *Front. Energy Res.*, vol. 10, 2022, Accessed: Sep. 12, 2023. [Online]. Available: https://www.frontiersin.org/articles/10.3389/fenrg.2022.936592

[7] M. C. Barla and D. Sarkar, "Optimal placement and sizing of BESS in RES integrated distribution systems," *Int. J. Syst. Assur. Eng. Manag.*, vol. 14, no. 5, pp. 1866–1876, Oct. 2023, doi: 10.1007/s13198-023-02016-w.

[8] "Free Access - NFPA 855: Standard for the Installation of Stationary Energy Storage Systems." Accessed: Oct. 17, 2023. [Online]. Available: https://link.nfpa.org/free-access/publications/855/2023

[9] "2427285.pdf | WebViewer." Accessed: Oct. 17, 2023. [Online]. Available: https://view.csagroup.org/x6K4ke

[10] D. Bernardi, E. Pawlikowski, and J. Newman, "A General Energy Balance for Battery Systems," *J. Electrochem. Soc.*, vol. 132, no. 1, p. 5, Jan. 1985, doi: 10.1149/1.2113792.

[11] D. Galatro, M. Al-Zareer, C. Da Silva, D. A. Romero, and C. H. Amon, "THERMAL BEHAVIOR OF LITHIUM-ION BATTERIES: AGING, HEAT GENERATION, THERMAL MANAGEMENT AND FAILURE," *Front. Heat Mass Transf.*, vol. 14, May 2020, doi: 10.5098/hmt.14.17.

[12] D. Velumani and A. Bansal, "Thermal Behavior of Lithium- and Sodium-Ion Batteries: A Review on Heat Generation, Battery Degradation, Thermal Runway – Perspective and Future Directions," *Energy Fuels*, vol. 36, no. 23, pp. 14000–14029, Dec. 2022, doi: 10.1021/acs.energyfuels.2c02889.

[13] D. Chalise, W. Lu, V. Srinivasan, and R. Prasher, "Heat of Mixing During Fast Charge/Discharge of a Li-Ion Cell: A Study on NMC523 Cathode," *J. Electrochem. Soc.*, vol. 167, no. 9, p. 090560, Jan. 2020, doi: 10.1149/1945-7111/abaf71.

[14] Y. Zeng, D. Chalise, S. D. Lubner, S. Kaur, and R. S. Prasher, "A review of thermal physics and management inside lithium-ion batteries for high energy density and fast charging," *Energy Storage Mater.*, vol. 41, pp. 264–288, Oct. 2021, doi: 10.1016/j.ensm.2021.06.008.

[15] T. M. Bandhauer, S. Garimella, and T. F. Fuller, "A Critical Review of Thermal Issues in Lithium-Ion Batteries," *J. Electrochem. Soc.*, vol. 158, no. 3, p. R1, Jan. 2011, doi: 10.1149/1.3515880.

[16] M. Song, Y. Hu, S.-Y. Choe, and T. R. Garrick, "Analysis of the Heat Generation Rate of Lithium-Ion Battery Using an Electrochemical Thermal Model," *J. Electrochem. Soc.*, vol. 167, no. 12, p. 120503, Aug. 2020, doi: 10.1149/1945-7111/aba96b.

[17] Y. Chen, L. Song, and J. W. Evans, "Modeling studies on battery thermal behaviour, thermal runaway, thermal management, and energy efficiency," in *IECEC 96. Proceedings of the 31st Intersociety Energy Conversion Engineering Conference*, Aug. 1996, pp. 1465–1470 vol.2. doi: 10.1109/IECEC.1996.553943.

[18] "A comprehensive review of lithium-ion batteries used in hybrid and electric vehicles at cold temperatures," *Appl. Energy*, vol. 164, pp. 99–114, Feb. 2016, doi: 10.1016/j.apenergy.2015.11.034.

[19] S. S. Zhang, K. Xu, and T. R. Jow, "Low temperature performance of graphite electrode in Li-ion cells," *Electrochimica Acta*, vol. 48, no. 3, pp. 241–246, Dec. 2002, doi: 10.1016/S0013-4686(02)00620-5.

[20] Y. Ji, Y. Zhang, and C.-Y. Wang, "Li-Ion Cell Operation at Low Temperatures," *J. Electrochem. Soc.*, vol. 160, no. 4, p. A636, Feb. 2013, doi: 10.1149/2.047304jes.

[21] S. S. Zhang, K. Xu, and T. R. Jow, "The low temperature performance of Li-ion batteries," *J. Power Sources*, vol. 115, no. 1, pp. 137–140, Mar. 2003, doi: 10.1016/S0378-7753(02)00618-3.

[22] S. Ma *et al.*, "Temperature effect and thermal impact in lithium-ion batteries: A review," *Prog. Nat. Sci. Mater. Int.*, vol. 28, no. 6, pp. 653–666, Dec. 2018, doi: 10.1016/j.pnsc.2018.11.002.

[23] X. H. Rui, Y. Jin, X. Y. Feng, L. C. Zhang, and C. H. Chen, "A comparative study on the low-temperature performance of LiFePO4/C and Li3V2(PO4)3/C cathodes for lithium-ion batteries," *J. Power Sources*, vol. 196, no. 4, pp. 2109–2114, Feb. 2011, doi: 10.1016/j.jpowsour.2010.10.063.

[24] Y. Liu, Y. Xia, and Q. Zhou, "Effect of low-temperature aging on the safety performance of lithium-ion pouch cells under mechanical abuse condition: A comprehensive experimental investigation," *Energy Storage Mater.*, vol. 40, pp. 268–281, Sep. 2021, doi: 10.1016/j.ensm.2021.05.022.

[25] Z. Li, J. Huang, B. Yann Liaw, V. Metzler, and J. Zhang, "A review of lithium deposition in lithium-ion and lithium metal secondary batteries," *J. Power Sources*, vol. 254, pp. 168–182, May 2014, doi: 10.1016/j.jpowsour.2013.12.099.

[26] M. Petzl, M. Kasper, and M. A. Danzer, “Lithium plating in a commercial lithium-ion battery – A low-temperature aging study,” *J. Power Sources*, vol. 275, pp. 799–807, Feb. 2015, doi: 10.1016/j.jpowsour.2014.11.065.

[27] P. Ramadass, B. Haran, R. White, and B. N. Popov, “Capacity fade of Sony 18650 cells cycled at elevated temperatures: Part II. Capacity fade analysis,” *J. Power Sources*, vol. 112, no. 2, pp. 614–620, Nov. 2002, doi: 10.1016/S0378-7753(02)00473-1.

[28] J. Shim, R. Kostecki, T. Richardson, X. Song, and K. A. Striebel, “Electrochemical analysis for cycle performance and capacity fading of a lithium-ion battery cycled at elevated temperature,” *J. Power Sources*, vol. 112, no. 1, pp. 222–230, Oct. 2002, doi: 10.1016/S0378-7753(02)00363-4.

[29] J. R. Belt, C. D. Ho, C. G. Motloch, T. J. Miller, and T. Q. Duong, “A capacity and power fade study of Li-ion cells during life cycle testing,” *J. Power Sources*, vol. 123, no. 2, pp. 241–246, Sep. 2003, doi: 10.1016/S0378-7753(03)00537-8.

[30] Q. Wang, P. Ping, X. Zhao, G. Chu, J. Sun, and C. Chen, “Thermal runaway caused fire and explosion of lithium ion battery,” *J. Power Sources*, vol. 208, pp. 210–224, Jun. 2012, doi: 10.1016/j.jpowsour.2012.02.038.

[31] L. Lu, X. Han, J. Li, J. Hua, and M. Ouyang, “A review on the key issues for lithium-ion battery management in electric vehicles,” *J. Power Sources*, vol. 226, pp. 272–288, Mar. 2013, doi: 10.1016/j.jpowsour.2012.10.060.

[32] W. Wu, S. Wang, W. Wu, K. Chen, S. Hong, and Y. Lai, “A critical review of battery thermal performance and liquid based battery thermal management,” *Energy Convers. Manag.*, vol. 182, pp. 262–281, Feb. 2019, doi: 10.1016/j.enconman.2018.12.051.

[33] X. Feng, C. Xu, X. He, L. Wang, G. Zhang, and M. Ouyang, “Mechanisms for the evolution of cell variations within a LiNixCoyMnzO2/graphite lithium-ion battery pack caused by temperature non-uniformity,” *J. Clean. Prod.*, vol. 205, pp. 447–462, Dec. 2018, doi: 10.1016/j.jclepro.2018.09.003.

[34] C. Kuper, M. Hoh, G. Houchin-Miller, and J. Fuhr, “Thermal Management of Hybrid Vehicle Battery Systems,” Jan. 2009.

[35] A. Pesaran, “Battery Thermal Management in EVs and HEVs: Issues and Solutions,” *Battery Man*, vol. 43, Jan. 2001.

[36] A. G. Olabi *et al.*, “Battery thermal management systems: Recent progress and challenges,” *Int. J. Thermofluids*, vol. 15, p. 100171, Aug. 2022, doi: 10.1016/j.ijft.2022.100171.

[37] J. R. Patel and M. K. Rathod, “Recent developments in the passive and hybrid thermal management techniques of lithium-ion batteries,” *J. Power Sources*, vol. 480, p. 228820, Dec. 2020, doi: 10.1016/j.jpowsour.2020.228820.

[38] “14.3.1.2 Thermal Convection - Knovel.” Accessed: Oct. 18, 2023. [Online]. Available: https://app.knovel.com/web/view/khtml/show.v/rcid:kpEEAIED01/cid:kt012RML27/viewerType:khtml/root_slug:exploring-engineering/url_slug:thermal-convection?&b-toc-cid=kpEEAIED01&b-toc-root-slug=exploring-engineering&b-toc-title=Exploring%20Engineering%20-%20An%20Introduction%20to%20Engineering%20and%20Design%20%285th%20Edition

%29&b-toc-url-slug=what-do-engineers-do&kpromoter=federation&view=collapsed&zoom=1&page=6

[39] K. Yu, X. Yang, Y. Cheng, and C. Li, "Thermal analysis and two-directional air flow thermal management for lithium-ion battery pack," *J. Power Sources*, vol. 270, pp. 193–200, Dec. 2014, doi: 10.1016/j.jpowsour.2014.07.086.

[40] J. Xie, Z. Ge, M. Zang, and S. Wang, "Structural optimization of lithium-ion battery pack with forced air cooling system," *Appl. Therm. Eng.*, vol. 126, pp. 583–593, Nov. 2017, doi: 10.1016/j.applthermaleng.2017.07.143.

[41] G. Zhao, X. Wang, M. Negnevitsky, and H. Zhang, "A review of air-cooling battery thermal management systems for electric and hybrid electric vehicles," *J. Power Sources*, vol. 501, p. 230001, Jul. 2021, doi: 10.1016/j.jpowsour.2021.230001.

[42] G. Karimi and A. R. Dehghan, "Thermal analysis of high-power lithium-ion battery packs using flow network approach," *Int. J. Energy Res.*, vol. 38, no. 14, pp. 1793–1811, 2014, doi: 10.1002/er.3173.

[43] X.-H. Yang, S.-C. Tan, and J. Liu, "Thermal management of Li-ion battery with liquid metal," *Energy Convers. Manag.*, vol. 117, pp. 577–585, Jun. 2016, doi: 10.1016/j.enconman.2016.03.054.

[44] S. Panchal, R. Khasow, I. Dincer, M. Agelin-Chaab, R. Fraser, and M. Fowler, "Thermal design and simulation of mini-channel cold plate for water cooled large sized prismatic lithium-ion battery," *Appl. Therm. Eng.*, vol. 122, pp. 80–90, Jul. 2017, doi: 10.1016/j.applthermaleng.2017.05.010.

[45] F. Bai, M. Chen, W. Song, Z. Feng, Y. Li, and Y. Ding, "Thermal management performances of PCM/water cooling-plate using for lithium-ion battery module based on non-uniform internal heat source," *Appl. Therm. Eng.*, vol. 126, pp. 17–27, Nov. 2017, doi: 10.1016/j.applthermaleng.2017.07.141.

[46] D. Chen, J. Jiang, G.-H. Kim, C. Yang, and A. Pesaran, "Comparison of different cooling methods for lithium ion battery cells," *Appl. Therm. Eng.*, vol. 94, pp. 846–854, Feb. 2016, doi: 10.1016/j.applthermaleng.2015.10.015.

[47] N. Wu, X. Ye, J. Li, B. Lin, X. Zhou, and B. Yu, "Passive thermal management systems employing hydrogel for the large-format lithium-ion cell: A systematic study," *Energy*, vol. 231, p. 120946, Sep. 2021, doi: 10.1016/j.energy.2021.120946.

[48] R. Kizilel, A. Lateef, R. Sabbah, M. M. Farid, J. R. Selman, and S. Al-Hallaj, "Passive control of temperature excursion and uniformity in high-energy Li-ion battery packs at high current and ambient temperature," *J. Power Sources*, vol. 183, no. 1, pp. 370–375, Aug. 2008, doi: 10.1016/j.jpowsour.2008.04.050.

[49] S. K. Maknikar and A. M. Pawar, "Application of phase change material (PCM) in battery thermal management system (BTMS): A critical review," *Mater. Today Proc.*, Aug. 2023, doi: 10.1016/j.matpr.2023.08.329.

[50] Y. Zhang *et al.*, "Experimental and Numerical Investigations of a Thermal Management System Using Phase-Change Materials and Forced-Air Cooling for High-Power Li-Ion Battery Packs," *Batteries*, vol. 9, no. 3, Art. no. 3, Mar. 2023, doi: 10.3390/batteries9030153.

[51] R. Kizilel, R. Sabbah, J. R. Selman, and S. Al-Hallaj, “An alternative cooling system to enhance the safety of Li-ion battery packs,” *J. Power Sources*, vol. 194, no. 2, pp. 1105–1112, Dec. 2009, doi: 10.1016/j.jpowsour.2009.06.074.

[52] Z. Ling *et al.*, “Experimental and numerical investigation of the application of phase change materials in a simulative power batteries thermal management system,” *Appl. Energy*, vol. 121, pp. 104–113, May 2014, doi: 10.1016/j.apenergy.2014.01.075.

[53] X. Luo *et al.*, “Experimental investigation on a novel phase change material composites coupled with graphite film used for thermal management of lithium-ion batteries,” *Renew. Energy*, vol. 145, pp. 2046–2055, Jan. 2020, doi: 10.1016/j.renene.2019.07.112.

[54] H. Jouhara, N. Serey, N. Khordehgah, R. Bennett, S. Almahmoud, and S. P. Lester, “Investigation, development and experimental analyses of a heat pipe based battery thermal management system,” *Int. J. Thermofluids*, vol. 1–2, p. 100004, Feb. 2020, doi: 10.1016/j.ijft.2019.100004.

[55] J. Zhao, P. Lv, and Z. Rao, “Experimental study on the thermal management performance of phase change material coupled with heat pipe for cylindrical power battery pack,” *Exp. Therm. Fluid Sci.*, vol. 82, pp. 182–188, Apr. 2017, doi: 10.1016/j.expthermflusci.2016.11.017.

[56] S. Wang *et al.*, “A forced gas cooling circle packaging with liquid cooling plate for the thermal management of Li-ion batteries under space environment,” *Appl. Therm. Eng.*, vol. 123, pp. 929–939, Aug. 2017, doi: 10.1016/j.applthermaleng.2017.05.159.

[57] M. Shahjalal *et al.*, “A review of thermal management for Li-ion batteries: Prospects, challenges, and issues,” *J. Energy Storage*, vol. 39, p. 102518, Jul. 2021, doi: 10.1016/j.est.2021.102518.

[58] S. S. Madani, C. Ziebert, and M. Marzband, “Thermal Behavior Modeling of Lithium-Ion Batteries: A Comprehensive Review,” *Symmetry*, vol. 15, p. 1597, Aug. 2023, doi: 10.3390/sym15081597.

[59] L. Rao and J. Newman, “Heat-Generation Rate and General Energy Balance for Insertion Battery Systems,” *J. Electrochem. Soc.*, vol. 144, no. 8, p. 2697, Aug. 1997, doi: 10.1149/1.1837884.

[60] K. E. Thomas and J. Newman, “Thermal Modeling of Porous Insertion Electrodes,” *J. Electrochem. Soc.*, vol. 150, no. 2, p. A176, Jan. 2003, doi: 10.1149/1.1531194.

[61] Y. Chen and J. W. Evans, “Three-Dimensional Thermal Modeling of Lithium-Polymer Batteries under Galvanostatic Discharge and Dynamic Power Profile,” *J. Electrochem. Soc.*, vol. 141, no. 11, p. 2947, Nov. 1994, doi: 10.1149/1.2059263.

[62] L. Wu, K. Liu, J. Liu, and H. Pang, “Evaluating the heat generation characteristics of cylindrical lithium-ion battery considering the discharge rates and N/P ratio,” *J. Energy Storage*, vol. 64, p. 107182, Aug. 2023, doi: 10.1016/j.est.2023.107182.

[63] W. B. Gu and C. Y. Wang, “Thermal-Electrochemical Modeling of Battery Systems,” *J. Electrochem. Soc.*, vol. 147, no. 8, p. 2910, Aug. 2000, doi: 10.1149/1.1393625.

[64] S. Wang, S. Ji, and Y. Zhu, “A comparative study of cooling schemes for laminated lithium-ion batteries,” *Appl. Therm. Eng.*, vol. 182, p. 116040, Jan. 2021, doi: 10.1016/j.applthermaleng.2020.116040.

[65] M. Akbarzadeh *et al.*, “A novel liquid cooling plate concept for thermal management of lithium-ion batteries in electric vehicles,” *Energy Convers. Manag.*, vol. 231, p. 113862, Mar. 2021, doi: 10.1016/j.enconman.2021.113862.

[66] M. Akbarzadeh *et al.*, “A comparative study between air cooling and liquid cooling thermal management systems for a high-energy lithium-ion battery module,” *Appl. Therm. Eng.*, vol. 198, p. 117503, Nov. 2021, doi: 10.1016/j.applthermaleng.2021.117503.

[67] H. Behi *et al.*, “A new concept of thermal management system in Li-ion battery using air cooling and heat pipe for electric vehicles,” *Appl. Therm. Eng.*, vol. 174, p. 115280, Jun. 2020, doi: 10.1016/j.applthermaleng.2020.115280.

[68] K. S. Hariharan, “A coupled nonlinear equivalent circuit – Thermal model for lithium ion cells,” *J. Power Sources*, vol. 227, pp. 171–176, Apr. 2013, doi: 10.1016/j.jpowsour.2012.11.044.

[69] L. Calearo, A. Thingvad, C. Ziras, and M. Marinelli, “A methodology to model and validate electro-thermal-aging dynamics of electric vehicle battery packs,” *J. Energy Storage*, vol. 55, p. 105538, Nov. 2022, doi: 10.1016/j.est.2022.105538.

[70] M. A. Perez Estevez, S. Calligaro, O. Bottesi, C. Caligiuri, and M. Renzi, “An electro-thermal model and its electrical parameters estimation procedure in a lithium-ion battery cell,” *Energy*, vol. 234, p. 121296, Nov. 2021, doi: 10.1016/j.energy.2021.121296.

[71] K. Kirad and M. Chaudhari, “Design of cell spacing in lithium-ion battery module for improvement in cooling performance of the battery thermal management system,” *J. Power Sources*, vol. 481, p. 229016, Jan. 2021, doi: 10.1016/j.jpowsour.2020.229016.

[72] L. H. Saw, Y. Ye, and A. A. O. Tay, “Electro-thermal characterization of Lithium Iron Phosphate cell with equivalent circuit modeling,” *Energy Convers. Manag.*, vol. 87, pp. 367–377, Nov. 2014, doi: 10.1016/j.enconman.2014.07.011.

[73] “How Is Soil Formed And How Many Layers Does It Have?,” Science ABC. Accessed: Sep. 27, 2023. [Online]. Available: https://www.scienceabc.com/nature/how-is-soil-formed-and-how-many-layers-does-it-have.html

[74] “Farouki: Thermal properties of soils - Google Scholar.” Accessed: Sep. 27, 2023. [Online]. Available: https://scholar.google.com/scholar_lookup?title=Thermal%20properties%20of%20soils&publication_year=1986&author=O.T.%20Farouki

[75] “Geothermal gradient,” *Wikipedia*. Sep. 01, 2023. Accessed: Oct. 05, 2023. [Online]. Available: https://en.wikipedia.org/w/index.php?title=Geothermal_gradient&oldid=1173355650

[76] G. of C. N. R. C. Canada, “Ground temperatures - NRC Publications Archive.” Accessed: Nov. 07, 2023. [Online]. Available: https://nrc-publications.canada.ca/eng/view/object/?id=386ddf88-fe8d-45dd-aabb-0a55be826f3f

[77] N. Catolico, S. Ge, and J. S. McCartney, "Numerical Modeling of a Soil-Borehole Thermal Energy Storage System," *Vadose Zone J.*, vol. 15, no. 1, p. vzj2015.05.0078, Jan. 2016, doi: 10.2136/vzj2015.05.0078.

[78] R. de Lieto Vollaro, L. Fontana, and A. Vallati, "Experimental study of thermal field deriving from an underground electrical power cable buried in non-homogeneous soils," *Appl. Therm. Eng.*, vol. 62, no. 2, pp. 390–397, Jan. 2014, doi: 10.1016/j.applthermaleng.2013.09.002.

[79] P. Ocłoń, P. Cisek, M. Pilarczyk, and D. Taler, "Numerical simulation of heat dissipation processes in underground power cable system situated in thermal backfill and buried in a multilayered soil," *Energy Convers. Manag.*, vol. 95, pp. 352–370, May 2015, doi: 10.1016/j.enconman.2015.01.092.

[80] N. Chapman and A. Hooper, "The disposal of radioactive wastes underground," *Proc. Geol. Assoc.*, vol. 123, no. 1, pp. 46–63, Jan. 2012, doi: 10.1016/j.pgeola.2011.10.001.

[81] K. Sookhak Lari and D. Mallants, "Coupled Heat-Mass Transport Modelling of Radionuclide Migration from a Nuclear Waste Disposal Borehole," *Geofluids*, vol. 2022, p. e5264257, Apr. 2022, doi: 10.1155/2022/5264257.

[82] M. R. Cosley and M. J. Marongiu, "Analytical/computational studies of the ground thermal characteristics for underground battery vault applications," in *Proceedings of 1994 4th Intersociety Conference on Thermal Phenomena in Electronic Systems (I-THERM)*, May 1994, pp. 275–281. doi: 10.1109/ITHERM.1994.342887.

[83] "Earth's internal heat budget," *Wikipedia*. Sep. 27, 2023. Accessed: Oct. 30, 2023. [Online]. Available: https://en.wikipedia.org/w/index.php?title=Earth%27s_internal_heat_budget&oldid=1177465813#Sources_of_heat

[84] H. K. Gupta and S. Roy, *Geothermal Energy: An Alternative Resource for the 21st Century*. Elsevier, 2006.

[85] S. W. Rees, M. H. Adjali, Z. Zhou, M. Davies, and H. R. Thomas, "Ground heat transfer effects on the thermal performance of earth-contact structures," *Renew. Sustain. Energy Rev.*, vol. 4, no. 3, pp. 213–265, Sep. 2000, doi: 10.1016/S1364-0321(99)00018-0.

[86] "2.1 The Heat Diffusion Equation - Knovel." Accessed: Oct. 31, 2023. [Online]. Available: https://app.knovel.com/web/view/khtml/show.v/rcid:kpHTTE0007/cid:kt00BT7TJ2/viewerType:khtml/root_slug:heat-transfer-textbook/url_slug:heat-diffusion-equation?&b-toc-cid=kpHTTE0007&b-toc-root-slug=heat-transfer-textbook&b-toc-title=Heat%20Transfer%20Textbook%20%284th%20Edition%29&b-toc-url-slug=introduction&kpromoter=federation&view=collapsed&zoom=1&page=1

[87] N. H. Abu-Hamdeh, "Thermal Properties of Soils as affected by Density and Water Content," *Biosyst. Eng.*, vol. 86, no. 1, pp. 97–102, Sep. 2003, doi: 10.1016/S1537-5110(03)00112-0.

[88] P. J. Wierenga, D. R. Nielsen, and R. M. Hagan, "Thermal Properties of a Soil Based Upon Field and Laboratory Measurements," *Soil Sci. Soc. Am. J.*, vol. 33, no. 3, pp. 354–360, 1969, doi: 10.2136/sssaj1969.03615995003300030009x.

[89] S. Upadhyay and A. S. Raghubanshi, “Chapter 16 - Determinants of soil carbon dynamics in urban ecosystems,” in *Urban Ecology*, P. Verma, P. Singh, R. Singh, and A. S. Raghubanshi, Eds., Elsevier, 2020, pp. 299–314. doi: 10.1016/B978-0-12-820730-7.00016-1.

[90] B. J. Huntley, “Soil, Water and Nutrients,” in *Ecology of Angola*, Springer, Cham, 2023, pp. 127–147. doi: 10.1007/978-3-031-18923-4_6.

[91] “Soil Water Dynamics | Learn Science at Scitable.” Accessed: Dec. 07, 2023. [Online]. Available: https://www.nature.com/scitable/knowledge/library/soil-water-dynamics-103089121/

[92] T. E. Ochsner, R. Horton, and T. Ren, “A New Perspective on Soil Thermal Properties,” *Soil Sci. Soc. Am. J.*, vol. 65, no. 6, pp. 1641–1647, 2001, doi: 10.2136/sssaj2001.1641.

[93] N. Zhang and Z. Wang, “Review of soil thermal conductivity and predictive models,” *Int. J. Therm. Sci.*, vol. 117, pp. 172–183, Jul. 2017, doi: 10.1016/j.ijthermalsci.2017.03.013.

[94] K.-Q. Li, D.-Q. Li, D.-H. Chen, S.-X. Gu, and Y. Liu, “A generalized model for effective thermal conductivity of soils considering porosity and mineral composition,” *Acta Geotech.*, vol. 16, no. 11, pp. 3455–3466, Nov. 2021, doi: 10.1007/s11440-021-01282-x.

[95] A. Cousin *et al.*, “Compositions of coarse and fine particles in martian soils at gale: A window into the production of soils,” *Icarus*, vol. 249, pp. 22–42, Mar. 2015, doi: 10.1016/j.icarus.2014.04.052.

[96] F. Qi *et al.*, “Soil particle size distribution characteristics of different land-use types in the Funiu mountainous region,” *Soil Tillage Res.*, vol. 184, pp. 45–51, Dec. 2018, doi: 10.1016/j.still.2018.06.011.

[97] J. Ball, “Soil and Water Relationships,” Noble Research Institute. Accessed: Sep. 28, 2023. [Online]. Available: https://www.noble.org/regenerative-agriculture/soil/soil-and-water-relationships/

[98] Y. Wang, Y. Lu, R. Horton, and T. Ren, “Specific Heat Capacity of Soil Solids: Influences of Clay Content, Organic Matter, and Tightly Bound Water,” *Soil Sci. Soc. Am. J.*, vol. 83, no. 4, pp. 1062–1066, 2019, doi: 10.2136/sssaj2018.11.0434.

[99] “Understanding Soil Water Content and Thresholds for Irrigation Management - Oklahoma State University.” Accessed: Nov. 06, 2023. [Online]. Available: https://extension.okstate.edu/fact-sheets/understanding-soil-water-content-and-thresholds-for-irrigation-management.html

[100] I. Hamdhan and C. Barry, “Determination of thermal conductivity of coarse and fine sand soils,” *Bali Indones. Proc. World Geotherm. Congr.*, Jan. 2010.

[101] T. Ochsner, “13.2 Soil Thermal Properties,” Jun. 2019, Accessed: Oct. 04, 2023. [Online]. Available: https://open.library.okstate.edu/rainorshine/chapter/13-2-soil-thermal-properties/

[102] D. W. Waples and J. S. Waples, “A Review and Evaluation of Specific Heat Capacities of Rocks, Minerals, and Subsurface Fluids. Part 1: Minerals and Nonporous Rocks,” *Nat. Resour. Res.*, vol. 13, no. 2, pp. 97–122, Jun. 2004, doi: 10.1023/B:NARR.0000032647.41046.e7.

[103] “Types of Rocks | Kinds of Rocks | Famous Rocks | Compare Rocks.” Accessed: Oct. 31, 2023. [Online]. Available: https://rocks.comparenature.com/rocks.comparenature.com/

[104] "2. Classification of Underground Space - Knovel." Accessed: Nov. 07, 2023. [Online]. Available: https://app.knovel.com/web/view/khtml/show.v/rcid:kpUIPDC002/cid:kt00A5COS4/viewerType:khtml/root_slug:underground-infrastructures/url_slug:classification-underground?&b-toc-cid=kpUIPDC002&b-toc-root-slug=underground-infrastructures&b-toc-title=Underground%20Infrastructures%20-%20Planning%2C%20Design%2C%20and%20Construction&b-toc-url-slug=introduction-2&kpromoter=federation&view=collapsed&zoom=1&page=3

[105] P. Ocłoń *et al.*, "Thermal performance optimization of the underground power cable system by using a modified Jaya algorithm," *Int. J. Therm. Sci.*, vol. 123, pp. 162–180, Jan. 2018, doi: 10.1016/j.ijthermalsci.2017.09.015.

[106] P. Ocłoń *et al.*, "The performance analysis of a new thermal backfill material for underground power cable system," *Appl. Therm. Eng.*, vol. 108, pp. 233–250, Sep. 2016, doi: 10.1016/j.applthermaleng.2016.07.102.

[107] S. J. Zarrouk and K. McLean, "Chapter 2 - Geothermal systems," in *Geothermal Well Test Analysis*, S. J. Zarrouk and K. McLean, Eds., Academic Press, 2019, pp. 13–38. doi: 10.1016/B978-0-12-814946-1.00002-5.

[108] Y.-S. Duh *et al.*, "Characterization on thermal runaway of commercial 18650 lithium-ion batteries used in electric vehicles: A review," *J. Energy Storage*, vol. 41, p. 102888, Sep. 2021, doi: 10.1016/j.est.2021.102888.

[109] "BAK_N21700CG_data_sheet.pdf." Accessed: Aug. 10, 2023. [Online]. Available: https://rotorgeeks.com/download/BAK_N21700CG_data_sheet.pdf

[110] G. M. Todys and S. Mahmud, "Thermal Characterization of a Cylindrical Li-ion Battery Cell Master's thesis in Electric Power Engineering," 2020. Accessed: Sep. 08, 2023. [Online]. Available: https://www.semanticscholar.org/paper/Thermal-Characterization-of-a-Cylindrical-Li-ion-in-Todys-Mahmud/4c7d030fa53e88cb2037625bff08ce5eb77cde5d

[111] M. Al-Zareer, A. Michalak, C. Da Silva, and C. H. Amon, "Predicting specific heat capacity and directional thermal conductivities of cylindrical lithium-ion batteries: A combined experimental and simulation framework," *Appl. Therm. Eng.*, vol. 182, p. 116075, Jan. 2021, doi: 10.1016/j.applthermaleng.2020.116075.

[112] K. Murashko, J. Pyrhönen, and J. Jokiniemi, "Determination of the through-plane thermal conductivity and specific heat capacity of a Li-ion cylindrical cell," *Int. J. Heat Mass Transf.*, vol. 162, p. 120330, Dec. 2020, doi: 10.1016/j.ijheatmasstransfer.2020.120330.

[113] M. Auch, T. Kuthada, and A. Wagner, "Simple experimental method to determine the specific heat capacity of cylindrical Lithium-Ion-Battery cells," *Appl. Therm. Eng.*, vol. 234, p. 121212, Nov. 2023, doi: 10.1016/j.applthermaleng.2023.121212.

[114] Y. Bai *et al.*, "Reversible and irreversible heat generation of NCA/Si–C pouch cell during electrochemical energy-storage process," *J. Energy Chem.*, vol. 29, pp. 95–102, Feb. 2019, doi: 10.1016/j.jechem.2018.02.016.

[115] A. Eddahech, O. Briat, and J.-M. Vinassa, "Thermal characterization of a high-power lithium-ion battery: Potentiometric and calorimetric measurement of entropy changes," *Energy*, vol. 61, pp. 432–439, Nov. 2013, doi: 10.1016/j.energy.2013.09.028.

[116] J. Fang, J. Cai, and X. He, "Experimental study on the vertical thermal runaway propagation in cylindrical Lithium-ion batteries: Effects of spacing and state of charge," *Appl. Therm. Eng.*, vol. 197, p. 117399, Oct. 2021, doi: 10.1016/j.applthermaleng.2021.117399.

[117] S. Ohneseit *et al.*, "Thermal and Mechanical Safety Assessment of Type 21700 Lithium-Ion Batteries with NMC, NCA and LFP Cathodes–Investigation of Cell Abuse by Means of Accelerating Rate Calorimetry (ARC)," *Batteries*, vol. 9, no. 5, p. 237, 2023, doi: 10.3390/batteries9050237.

[118] K. Murashko, D. Li, D. L. Danilov, P. H. L. Notten, J. Pyrhönen, and J. Jokiniemi, "Applicability of Heat Generation Data in Determining the Degradation Mechanisms of Cylindrical Li-Ion Batteries," *J. Electrochem. Soc.*, vol. 168, no. 1, p. 010511, Jan. 2021, doi: 10.1149/1945-7111/abd832.

[119] "BACKTOGRID_20162.pdf." Accessed: Oct. 11, 2023. [Online]. Available: https://www.greenlightinnovation.com/files/product-documents/5c6755c6787fc/BACKTOGRID_20162.pdf

[120] "orionbms_specifications.pdf." Accessed: Oct. 11, 2023. [Online]. Available: https://www.orionbms.com/downloads/documents/orionbms_specifications.pdf

[121] "thermistor_expansion_spec.pdf." Accessed: Oct. 11, 2023. [Online]. Available: https://www.orionbms.com/downloads/documents/thermistor_expansion_spec.pdf

[122] "s_cr5000.pdf." Accessed: Oct. 11, 2023. [Online]. Available: https://s.campbellsci.com/documents/us/product-brochures/s_cr5000.pdf

[123] "TEMPOS," METER. Accessed: Oct. 11, 2023. [Online]. Available: https://www.metergroup.com/en/meter-environment/products/tempos/tempos-tech-specs

[124] "ECH20 EC-5," METER. Accessed: Oct. 11, 2023. [Online]. Available: https://www.metergroup.com/en/meter-environment/products/ech20-ec-5-soil-moisture-sensor

[125] "Battery Analyzer | Battery Impedance Tester | BT521 | BT520 | BT510." Accessed: Oct. 11, 2023. [Online]. Available: https://www.fluke.com/en-us/product/electrical-testing/battery-analyzers/fluke-500

[126] "Fluke 289 True-RMS Industrial Data Logging Multimeter." Accessed: Oct. 11, 2023. [Online]. Available: https://www.fluke.com/en-us/product/electrical-testing/digital-multimeters/fluke-289

[127] "Temperature Controller ITC-308," INKBIRD. Accessed: Oct. 11, 2023. [Online]. Available: https://inkbird.com/products/temperature-controller-itc-308

[128] A. A. G. Al-shammary, A. Z. Kouzani, A. Kaynak, S. Y. Khoo, M. Norton, and W. Gates, "Soil Bulk Density Estimation Methods: A Review," *Pedosphere*, vol. 28, no. 4, pp. 581–596, Aug. 2018, doi: 10.1016/S1002-0160(18)60034-7.

[129] S. Barcellona, S. Colnago, G. Dotelli, S. Latorrata, and L. Piegari, "Aging effect on the variation of Li-ion battery resistance as function of temperature and state of charge," *J. Energy Storage*, vol. 50, p. 104658, Jun. 2022, doi: 10.1016/j.est.2022.104658.

[130] S. Hossain Ahmed, X. Kang, and S. O. Bade Shrestha, “Effects of Temperature on Internal Resistances of Lithium-Ion Batteries,” *J. Energy Resour. Technol.*, vol. 137, no. 031901, May 2015, doi: 10.1115/1.4028698.

[131] H. Aung and K. Low, “Opportunistic State of Charge (SOC) Estimation for a Nanosatellite,” Jun. 2013.

[132] H. Wang *et al.*, “High-power charging strategy within key SOC ranges based on heat generation of lithium-ion traction battery,” *J. Energy Storage*, vol. 72, p. 108125, Nov. 2023, doi: 10.1016/j.est.2023.108125.

[133] K. Hirbodi and K. Jafarpur, “A simple and accurate model for conduction shape factor of hollow cylinders,” *Int. J. Therm. Sci.*, vol. 153, p. 106362, Jul. 2020, doi: 10.1016/j.ijthermalsci.2020.106362.

Appendix A: Copyright Permission

Figure 1: Different air-cooling channel designs [41]. Reproduced with permission from the publisher copyright

ELSEVIER LICENSE
TERMS AND CONDITIONS

Nov 30, 2023

This Agreement between Miss. Elizabeth Oyekola ("You") and Elsevier ("Elsevier") consists of your license details and the terms and conditions provided by Elsevier and Copyright Clearance Center.

License Number	5678831082531
License date	Nov 30, 2023
Licensed Content Publisher	Elsevier
Licensed Content Publication	Journal of Power Sources
Licensed Content Title	A review of air-cooling battery thermal management systems for electric and hybrid electric vehicles
Licensed Content Author	Gang Zhao,Xiaolin Wang,Michael Negnevitsky,Hengyun Zhang
Licensed Content Date	Jul 31, 2021
Licensed Content Volume	501
Licensed Content Issue	n/a
Licensed Content Pages	1
Start Page	230001
End Page	0

Figure 2: Annual temperature fluctuations with depth in the ground (Ottawa) [76]– Reproduced with the permission of the National Research Council of Canada, copyright holder

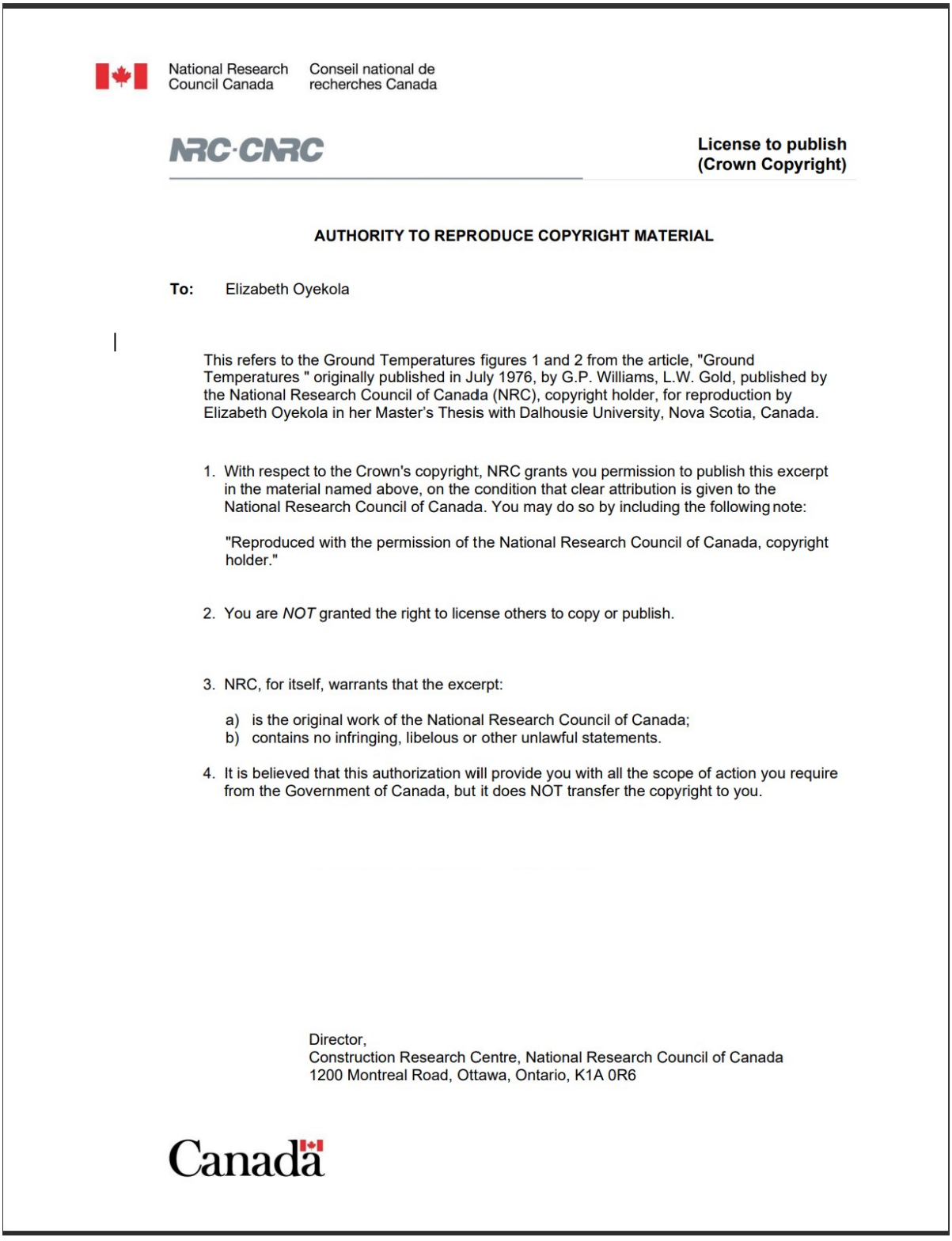

National Research Council Canada | Conseil national de recherches Canada

NRC·CNRC

License to publish (Crown Copyright)

AUTHORITY TO REPRODUCE COPYRIGHT MATERIAL

To: Elizabeth Oyekola

This refers to the Ground Temperatures figures 1 and 2 from the article, "Ground Temperatures " originally published in July 1976, by G.P. Williams, L.W. Gold, published by the National Research Council of Canada (NRC), copyright holder, for reproduction by Elizabeth Oyekola in her Master's Thesis with Dalhousie University, Nova Scotia, Canada.

1. With respect to the Crown's copyright, NRC grants you permission to publish this excerpt in the material named above, on the condition that clear attribution is given to the National Research Council of Canada. You may do so by including the following note:

   "Reproduced with the permission of the National Research Council of Canada, copyright holder."

2. You are *NOT* granted the right to license others to copy or publish.

3. NRC, for itself, warrants that the excerpt:

   a) is the original work of the National Research Council of Canada;
   b) contains no infringing, libelous or other unlawful statements.

4. It is believed that this authorization will provide you with all the scope of action you require from the Government of Canada, but it does NOT transfer the copyright to you.

Director,
Construction Research Centre, National Research Council of Canada
1200 Montreal Road, Ottawa, Ontario, K1A 0R6

Canada

Figure 3: soil types by texture [91]

Figure 4: Soil moisture content capacity according to texture [91]

Figures 3 and 4 are obtained from the article “Soil, Water and Nutrients” published in [90], which is licensed under the terms of the Creative Commons Attribution 4.0 International License (http://creativecommons.org/licenses/by/4.0/).

Soil, Water and Nutrients

Rights and permissions

Open Access This chapter is licensed under the terms of the Creative Commons Attribution 4.0 International License (http://creativecommons.org/licenses/by/4.0/), which permits use, sharing, adaptation, distribution and reproduction in any medium or format, as long as you give appropriate credit to the original author(s) and the source, provide a link to the Creative Commons license and indicate if changes were made.

The images or other third party material in this chapter are included in the chapter's Creative Commons license, unless indicated otherwise in a credit line to the material. If material is not included in the chapter's Creative Commons license and your intended use is not permitted by statutory regulation or exceeds the permitted use, you will need to obtain permission directly from the copyright holder.

Reprints and Permissions

Copyright information

© 2023 The Author(s)

Figure 5: Soil thermal properties: Thermal conductivity (λ), heat capacity (C), and thermal diffusivity (α) versus volume fractions of water (Θ), solids (vs), and air (na) for four medium-textured soils [92]. Reproduced with permission from the publisher copyright

JOHN WILEY AND SONS LICENSE
TERMS AND CONDITIONS

Nov 06, 2023

This Agreement between Miss. Elizabeth Oyekola ("You") and John Wiley and Sons ("John Wiley and Sons") consists of your license details and the terms and conditions provided by John Wiley and Sons and Copyright Clearance Center.

License Number	5663151098934
License date	Nov 06, 2023
Licensed Content Publisher	John Wiley and Sons
Licensed Content Publication	SOIL SCIENCE SOCIETY OF AMERICA JOURNAL
Licensed Content Title	A New Perspective on Soil Thermal Properties
Licensed Content Author	Tusheng Ren, Robert Horton, Tyson E. Ochsner
Licensed Content Date	Nov 1, 2001
Licensed Content Volume	65
Licensed Content Issue	6
Licensed Content Pages	7

Appendix B: Datalogger Script

The code below was used to record and store soil temperature data in the CR5000 Campbell Scientific datalogger during battery testing.

```
'CR5000

'Declare Variables and Units
Public DL_B_V
Public DL_T_C
Public Lab_T_C
Public T_1CT_C
Public T_1ST_C
Public T_1CB_C
Public T_1SB_C
Public T_2CT_C
Public T_2ST_C
Public T_2CB_C
Public T_2SB_C
Public T_3CT_C
Public T_3ST_C
Public T_3CB_C
Public T_3SB_C
Public VWC_2CT_mV
Public VWC_2CB_mV
Public VWC_2CT_pct
Public VWC_2CB_pct
Const VWC_Mult=0.8406
Const VWC_Offset=0.4196

'Define Data Tables
DataTable(Data,True,-1)
```

```
        DataInterval(0,60,Sec,10)
        Average(1,DL_B_V,FP2,False)
        Average(1,DL_T_C,FP2,False)
        Average(1,Lab_T_C,FP2,False)
        Average(1,T_1CT_C,FP2,False)
        Average(1,T_1ST_C,FP2,False)
        Average(1,T_1CB_C,FP2,False)
        Average(1,T_1SB_C,FP2,False)
        Average(1,T_2CT_C,FP2,False)
        Average(1,T_2ST_C,FP2,False)
        Average(1,T_2CB_C,FP2,False)
        Average(1,T_2SB_C,FP2,False)
        Average(1,T_3CT_C,FP2,False)
        Average(1,T_3ST_C,FP2,False)
        Average(1,T_3CB_C,FP2,False)
        Average(1,T_3SB_C,FP2,False)
        Average(1,VWC_2CT_mV,FP2,False)
        Average(1,VWC_2CB_mV,FP2,False)
        Average(1,VWC_2CT_pct,FP2,False)
        Average(1,VWC_2CB_pct,FP2,False)
EndTable

'Main Program
BeginProg
        'Main Scan
        Scan(1,Sec,1,0)
                Battery(DL_B_V)
                PanelTemp(DL_T_C,_60Hz)

                TCDiff(T_1CT_C,1,mV20C,1,TypeT,DL_T_C,True,0,_60Hz,1,0)
                TCDiff(T_1ST_C,1,mV20C,2,TypeT,DL_T_C,True,0,_60Hz,1,0)
```

```
        TCDiff(T_1CB_C,1,mV20C,3,TypeT,DL_T_C,True,0,_60Hz,1,0)
        TCDiff(T_1SB_C,1,mV20C,4,TypeT,DL_T_C,True,0,_60Hz,1,0)
        TCDiff(T_2CT_C,1,mV20C,5,TypeT,DL_T_C,True,0,_60Hz,1,0)
        TCDiff(T_2ST_C,1,mV20C,6,TypeT,DL_T_C,True,0,_60Hz,1,0)
        TCDiff(T_2CB_C,1,mV20C,7,TypeT,DL_T_C,True,0,_60Hz,1,0)
        TCDiff(T_2SB_C,1,mV20C,8,TypeT,DL_T_C,True,0,_60Hz,1,0)
        TCDiff(T_3CT_C,1,mV20C,11,TypeT,DL_T_C,True,0,_60Hz,1,0)
        TCDiff(T_3ST_C,1,mV20C,12,TypeT,DL_T_C,True,0,_60Hz,1,0)
        TCDiff(T_3CB_C,1,mV20C,13,TypeT,DL_T_C,True,0,_60Hz,1,0)
        TCDiff(T_3SB_C,1,mV20C,14,TypeT,DL_T_C,True,0,_60Hz,1,0)

        TCDiff(Lab_T_C,1,mV20C,20,TypeT,DL_T_C,True,0,_60Hz,1,0)

        VoltDiff(VWC_2CT_mV,1,mV5000,9,True,0,_60Hz,1,0)
        VoltDiff(VWC_2CB_mV,1,mV5000,10,True,0,_60Hz,1,0)
        VoltDiff(VWC_2CT_pct,1,mV5000,9,True,0,_60Hz,VWC_Mult,VWC_Offset)
        VoltDiff(VWC_2CB_pct,1,mV5000,10,True,0,_60Hz,VWC_Mult,VWC_Offset)

        'Call Data Tables and Store Data
        CallTable Data
    NextScan
EndProg
```

Appendix C: Data Processing Python Code

The code below was used to process soil temperature data and create chart results obtained from experiments or model results.

```
import pandas as pd
import numpy as np
import os
from matplotlib import pyplot as plt
import seaborn as sns
%matplotlib inline
model_data = pd.read_csv('filepath.csv')
model_data = model_data.set_index('Time (s)',drop=True)
model_data['elapsed time'] = (model_data.index )

Temps = [t for t in model_data.columns if 'T_xxx' in t]

fig, ax = plt.subplots(figsize=(12,8))
x = model_data['elapsed time']
y1 = model_data['Battery Power (kW)']
ax.plot(x,y1,color='black',label='Battery Power (kW)')
ax.set_xlabel('Elapsed time (h)')
ax.set_ylabel('Battery Power (kW)')

ax1 = ax.twinx()
for c in model_temps:
  y2 = model_data[c]
  ax1.plot(x,y2,label=c,linestyle='--')

ax1.set_axisbelow(True)
ax1.grid(axis='both')
ax1.set_ylabel('Temperature \N{DEGREE SIGN}C')

ax.set_zorder(1)
lns = [l for l in ax.lines] + [l for l in ax1.lines]
labs = [l.get_label() for l in lns]
ax.legend(lns,labs,bbox_to_anchor=(1.07,1),loc='best',ncol=2)
```

Appendix D: ANSYS Model Temperature Figure